Synthesis and Characterization of Thionated Reduced Graphene Oxides and Their Thin Films

by

Kiwan Jeon

A Dissertation Presented in Partial Fulfillment
of the Requirements for the Degree
Doctor of Philosophy

Approved November 2013 by the
Graduate Supervisory Committee:

Dong-Kyun Seo, Chair
Anne Jones
Jeffery Yarger

ARIZONA STATE UNIVERSITY

December 2013

ABSTRACT

Thiol functionalization is one potentially useful way to tailor physical and chemical properties of graphene oxides (GOs) and reduced graphene oxides (RGOs). Despite the ubiquitous presence of thiol functional groups in diverse chemical systems, efficient thiol functionalization has been challenging for GOs and RGOs, or for carbonaceous materials in general. In this work, thionation of GOs has been achieved in high yield through two new methods that also allow concomitant chemical reduction/thermal reduction of GOs; a solid-gas metathetical reaction method with boron sulfides (B_xS_y) gases and a solvothermal reaction method employing phosphorus decasulfide (P_4S_{10}). The thionation products, called "mercapto reduced graphene oxides (m-RGOs)", were characterized by employing X-ray photoelectron spectroscopy, powder X-ray diffraction, UV-Vis spectroscopy, FT-IR spectroscopy, Raman spectroscopy, electron probe analysis, scanning electron microscopy, (scanning) transmission electron microscopy, nano secondary ion mass spectrometry, Ellman assay and atomic force microscopy.

The excellent dispersibility of m-RGOs in various solvents including alcohols has allowed fabrication of thin films of m-RGOs. Deposition of m-RGOs on gold substrates was achieved through solution deposition and the m-RGOs were homogeneously distributed on gold surface shown by atomic force microscopy. Langmuir-Blodgett (LB) films of m-RGOs were obtained by transferring their Langmuir films, formed by simple drop casting of m-RGOs dispersion on water surface, onto various substrates including gold, glass and indium tin oxide. The m-RGO LB films showed low sheet resistances down to about 500 kΩ/sq at 92% optical transparency. The successful results make m-RGOs promising for applications in transparent conductive coatings, biosensing, etc.

DEDICATION

For Seong-Hee Kim and Kaylee Yoonseo Jeon

ACKNOWLEDGMENTS

First of all, I would like to acknowledge my committee members, Prof. Anne Jones and Prof. Jeffery Yarger. I particularly appreciate Prof. Dong-Kyun Seo, my advisor, for his encouragement, support, and patience. He always has tried to show me how to think and how to solve problems. He also has provided guidelines I am supposed to follow for research. Whenever I have encountered problems for research, he has helped me to better understand the problem and provided clues to solve the problem. From the beginning of my journey to this moment in graduate school, he has guided me to keep going: sometimes fast and sometimes slow but never to stop. Prof. Seo has given me intellectual and emotional support throughout this journey.

I also would like to thank to all my group-mates, Alex, Danielle, Dinesh, Daniel, Chang-Hee, Sudhanshu, Barun, and Milad and collaborators. There are many unforgettable things during my Ph.D study. Especially, brewing beer with Dinesh and Daniel was great experience to me and it refreshed me to work hard again.

I also would like to thank all my family members for their support. I have felt sorry for not being able to participate in certain family events, particularly my elder brother's wedding ceremony. I would like to thank my wife, Seong-Hee and my daughter, Kaylee Yoonseo. Kaylee is an energizer for me and that motivated me to achieve my goals. I especially appreciate Seong-Hee for all of her efforts. She sacrificed many things for me. She had maternity leave to stay in Arizona with Kaylee and me and she also took care of Kaylee all day. She also encouraged me to finish my Ph.D work.

TABLE OF CONTENTS

CHAPTER Page

CHAPTER Page

LIST OF TABLES

Table Page

LIST OF FIGURES

Figure Page

Figure Page

Figure Page

CHAPTER 1

INTRODUCTION

1.1 Graphene

Graphene is a one-atom-thick planar sheet of sp^2-hybridized carbon atoms arranged into a two-dimensional (2D) hexagonal honeycomb network, and is a basic building block for other important carbon allotropes, as depicted in **Figure 1**.[1] Theoretical properties of graphene and/or graphite have been investigated for more than a half century[2] and are used to describe various properties of carbon-based materials and their composites. Graphene has been described as an academic material[3] and was once believed not to exist in a free state because 2D crystals were thought to be thermodynamically unstable at finite temperatures.[4] However, in 2004, graphene was successfully isolated for the first time through the scotch tape method of highly ordered pyrolytic graphite (HOPG).[5] This fascinated the scientific community, who began to study the free-standing graphene. The isolated graphene was found to be stable under ambient conditions, exhibiting high quality and continuity on a microscopic scale, which led an explosion of interest.

The extended sp^2-hybridized carbon network exhibits exceptional electronic,[6] mechanical,[7] and thermal properties.[8] These have been the focus of theoretical studies and have fascinated experimentalists, because the graphene was isolated. Graphene is found to have many interesting properties. Many studies have provided observations of unique properties, including graphene's remarkably high electron mobility at room temperature with experimentally reported values in 15,000 ~ 20,000 $cm^2V^{-1}s^{-1}$,[5] the Quantum Hall Effect (QHE) for both electrons and holes even at room temperature,[9] single-molecule detection,[10] an excellent thermal conductivity (~ 5000 W/mK),[8] and high mechanical stiffest (Young's modulus of ~ 1 TPa),[11] large specific surface area (~ 2,600 m^2/g),[12] and optical transparency (~ 98%).[13]

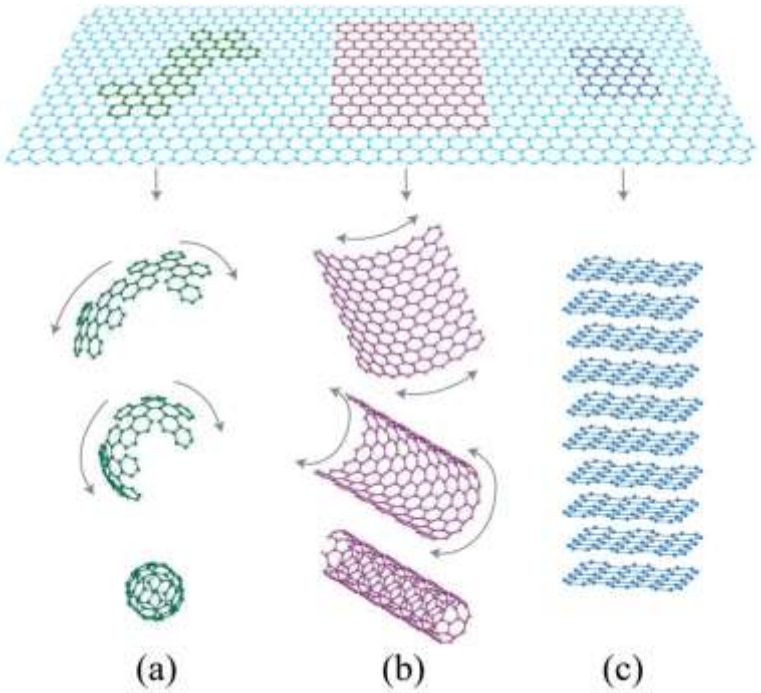

Figure 1. Graphene: building block for all other carbon allotropes. It can be wrapped up into (a) 0D buckyballs, rolled into (b) 1D carbon nano-tube, and stacked to form (c) 3D graphite, adopted from Geim.[1]

Thanks to the extraordinary properties aforementioned, it is no wonder that graphene has been considered a more promising material than other nanostructured carbon allotropes, i.e. 0D fullerenes and 1D carbon nanotubes, for a variety of applications such as field-effect transistors,[14] capacitors,[15] energy storage,[16] sensors,[17] transparent conductive films,[18] and heavy metals removal.[19] Moreover, graphene-based composite materials show high electrical conductivity and thus could be promising candidates for sensors[20] as well as Li-ion batteries.[21] Graphene-based sensors show promising responses because of the dependency of the electrical conductivity of graphene on the concentration of various gaseous species. Once graphene is biofunctionalized with biomolecules, the graphene-based nanostructures may open a gateway to new application fields in biotechnology.[22] Recently,

graphene has been used as a promising component in the development of Förster resonance energy transfer (FRET) biosensors due to its quenching capability toward various organic dyes and quantum dots, as well as its fast DNA sequencing.[23] Graphene can be used as a transparent and flexible electrode in photovoltaic cells,[24] touch-screens,[25] liquid crystal displays (LCDs), and organic light emitting diodes (OLEDs) because of its high electrical conductivity and high optical transparency.[1, 26] Graphene has also been envisioned as a potential candidate to replace indium tin oxide (ITO) because of its high strength, flexibility and stretchability.

1.2 Structure of Graphene

In order to better understand the properties of graphene, it is imperative to understand its structure. Graphene consists of a layer of sp^2 carbon hexagonal network. Up to 10 of layers graphene have been treated in 2 dimensional sheets based on electronic structure. The electronic structure of more than 10 layers of graphene approaches the 3 dimensional limit of graphite.[1] Graphene thicker than 10 layers should be considered a thin film of graphite. In a bi-layer or a few layers of graphene, each layer can be stacked in different ways, generating hexagonal (AA), Bernal (ABA), or rhombohedral (ABC) stacking as shown in **Figure 2(a)**. Each six-membered ring repeating unit of graphene sheet consists of three in-plane σ-bonds and π-orbitals perpendicular to the plane, contributing to a delocalized network of electrons as depicted in **Figure 2(b)**. The s, p_x, and p_y, atomic orbitals on each carbon hybridize to form strong covalent sp^2 bonds, giving rise to 120° C–C–C angles that generate the framework of the hexagonal structure (σ-bonds). The remaining p_z atomic orbital on each carbon overlaps with adjacent carbon to form π-orbitals that control interaction between inter-layers (π-bonds).

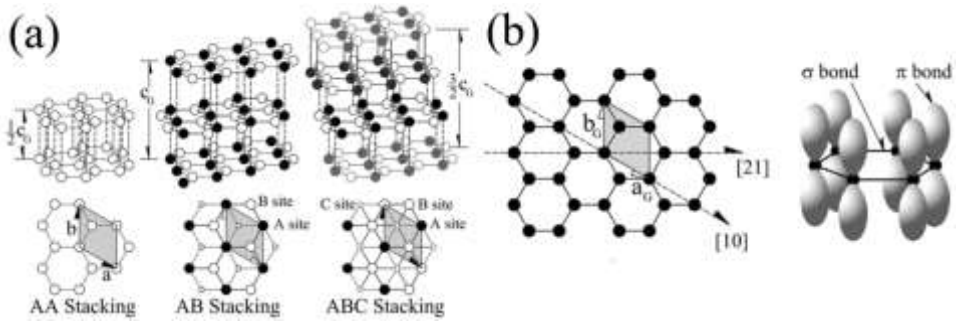

Figure 2. (a) Three most common structures and stacking sequence of graphene and (b) Schematic of the in-plane σ-bonds and π-orbitals perpendicular to plane of the graphene sheet, adopted from Hass.[27]

1.3 Various Synthetic Methods of Graphene

To date, various pathways have been developed to obtain graphene. Among many methods, they can be categorized in two ways: 1) top-bottom approaches and 2) bottom-top process. Each method has its drawbacks. For top-bottom approaches, the mechanical exfoliation method produces the highest quality graphene, but it is neither high throughput nor high product yield. An alternative to mechanical exfoliation is a chemical effort to exfoliate and stabilize the graphene sheet in solution.[28] To date, complete exfoliation of graphene in solution requires extensive modification of the 2D lattice, which may not be desirable for many application fields.[29] Bottom-top techniques include chemical vapor deposition, epitaxial graphene, and organic syntheses; these techniques have yet to produce a large-quantity of graphene and a uniform single layer.

1.3.1 Mechanical Exfoliation of Graphite

The mechanical exfoliation undertaken in 2004 revealed that carbon exfoliates in the form of graphitic layers on transition metal substrates. Several research groups tried to exfoliate HOPG to produce single sheets on SiO_2 substrate by using

an atomic force microscope (AFM)[30] but they couldn't achieve a single graphitic layer. While these elegant methods produced more than 10 layers of graphene sheet, a much simpler method, the scotch tape method, successfully isolated mono-layer graphene from HOPG in 2004.[5] Moreover, the electronic properties of graphene were reported for the first time in 2004.[5] The first mechanically isolated mono/few layers graphene from HOPG were transferred on SiO_2/Si substrate that allowed them to fabricate graphene transistor devices. Since then, the mechanical cleavage method has attracted attention as a reliable method for obtaining monolayer graphene flakes on foreign substrates. Mechanical exfoliation involves isolating graphene flakes from an HOPG block or graphite flakes by repeated peeling using different techniques such as scotch tape, ultrasonication and transfer printing. The approach was also used to produce 2D atomic crystals of many other materials such as BN, MoS_2, etc. This is the cheapest technique that has been used so far to produce the highest quality monolayer graphene sheets. This method, however, is low throughput; the product yield of single or few layer graphene obtained by this technique is also very poor, and the locations of graphene sheets are randomly distributed on the substrate. Thus mechanical exfoliation is so far well suited only for the fundamental study of graphene and is not scalable to industrial production.

1.3.2 Reduced Graphene Oxide (RGO)

To date, there is no method that can produce as much high quality graphene as can be generated by the mechanical exfoliation method. However, it is not suitable for large production, as mentioned above. Therefore there is a great interest in large-scale production of graphene suitable for many applications. Among the various synthetic methods for the mass production of graphene, reduction of graphene oxide, including both chemical and thermal reduction, is the current most

obvious and desirable route to produce large quantities of graphene-like materials. Moreover, the reduction process is the most important reaction of graphene oxide because of the similarity between reduced graphene oxide and pristine graphene. All of these methods produce products that are particularly similar to pristine graphene in terms of their electrical, thermal, mechanical properties as well as their surface morphology.

The various polar oxygen functional groups formed during oxidation of graphite flakes render graphite oxide (GO) hydrophilic and weaken the Van der Waals interactions. Thus GO can be easily exfoliated in several solvents, including water, by sonication.[31] In this method, completely exfoliated sheets are readily obtained from dispersions of graphene oxide prepared by sonication of GO dispersed in water.[31a] In general, GO has been synthesized by modified Brodie,[32] Staudenmaier,[33] or Hummers methods.[34] All these methods involve oxidation of graphite in the presence of strong oxidants. The methods of Brodie and Staudenmaier employ a combination of potassium chlorate ($KClO_3$) with nitric acid (HNO_3) to oxidize graphite flakes, while the Hummers method utilizes a combination of potassium permanganate ($KMnO_4$) and sulfuric acid (H_2SO_4) to oxidize graphite flakes. The Brodie method is not particularly efficient, and thus these days either the Staudenmaier or Hummers methods are used to oxidize graphite flakes. GO is highly hydrophilic due to the existence of various oxygen functional groups such as hydroxyl, epoxy, carbonyl, and carboxyl functional groups on the basal plane and at the edge of each graphitic layer during oxidation. Thus, GO is easily exfoliated in polar solvents, particularly well in water by sonication or mechanical stirring because the Van der Waals interaction between the inter-sheet gallery becomes weak due to intercalated water molecules[35] that generate a higher inter-layer distance (~ 9 A) than that of graphite (3.4 A).

After that, the colloidal dispersion of graphene oxide can be reduced to prepare reduced graphene oxide using several reducing agents such as hydrazine,[28c] hydroquinone,[36] sodium borohydride,[37] ascorbic acid,[38] and so forth. While many strong reducing agents have a slight to very strong reactivity with water, hydrazine or hydrazine hydrate do not. Therefore, among various reducing agents, hydrazine or hydrazine hydrate was one of the first reducing reagents to be used to reduce graphene oxide. However, because hydrazine or hydrazine hydrate is highly poisonous and explosive, precautions must be considered when a large amount of hydrazine is used. Many researchers have tried to look for safer and greener reducing agents with similar or more effective reduction of graphene oxide. The use of multiple reducing agents was also demonstrated to further reduce the graphene oxide, but this approach turns out to be limited given the effectiveness of hydrazine and $NaBH_4$ on their own.

The chemical reduction method is obviously the most common method to reduce graphene oxide but this does not mean that chemical reduction is the only way for the reduction of graphene oxide. Reduction of graphene oxide using thermal treatment in reducing atmosphere has also been considered as an efficient and low cost method. Thermal exfoliation and reduction of graphene oxide was demonstrated.[39] Rather than removing oxygen functional groups from the surface of GO through chemical reactions, it is possible to produce thermodynamically more stable carbon oxide species by introducing GO in a pre-heated furnace at 1050 °C.[39a] The generated carbon dioxide produces enormous pressure within the inter-layer gallery and the vast pressure can exfoliate GO. In order to exfoliate two stacked graphene oxide sheets, only 2.5 MPa is required. According to the previous report, a pressure of 40 MPa is generated at 300 °C, whereas a pressure of 130 MPa is produced at 1000 °C.[39a] During thermal exfoliation and reduction, structural damage

occurs *via* the release of carbon dioxide,[40] making approximately 30% of weight loss of GO.[39b]

Reduced graphene oxide has been shown to have promising potential in various applications such as transparent conductive electrodes,[18b] graphene-based polymer composites,[41] sensors,[42] capacitors,[43] and so on. However, these chemically and thermally reduced graphene sheets still contain oxygen function groups and other impurities due to the lack of complete reduction of graphene oxide, which may limit their application in many other areas of nano-electronics.

1.3.3. Epitaxial Graphene

The definition of epitaxy is a process of growing a crystal of a particular orientation on top of another crystal. If both crystals are of the same materials it will be called a homoepitaxy. And if the materials are different from each other, it will be called heteroepitaxy. In this particular process, graphene is directly grown on an epitaxially matched insulating or semiconducting substrate by chemical deposition technique. Graphene produced in this pathway is referred as an epitaxial graphene. Approximately 40 years ago, graphene formation was for the first time experimentally determined and investigations were carried out on the thermodynamics of growth of graphitic monolayer by near equilibrium segregation on a single crystalline Ni (111) surface.[44] However, the properties of those films on different metal surfaces produced through this process were not consistent with graphitic thin films on Ni surface. Moreover, the limitation of finally identifying the proper application of those films and thus this process was not studied extensively.

A more recently, implemented technique to produce graphene has employed SiC substrate to grow large area epitaxial graphene. The growth of epitaxial graphene is highly dependent on SiC orientation and hence it is important to understand the structure of SiC. Mostly, epitaxial graphene has been grown on hexagonal SiC substrates; therefore only hexagonal SiC structure will be considered. The two hexagonal SiC substrates which have commonly been used to grow epitaxial graphene are 4H- and 6H-SiC. The unit cell of each SiC is shown in **Figure 3**.[27] In both cases, unit cells consist of Si–C bilayers with different stacking arrangements. In case of the unit cell for 4H-SiC, the stacking is ABCB····· and for the unit cell of 6H-SiC, it is ABCACB·····. An *n*H-SiC unit cell is made of *n*Si–C bilayer. The unit cell of SiC has two polar faces perpendicular to c-axis. The Si terminated face (Si face) has one Si dangling bond per Si atom and C terminated face (C face) has one C dangling bond per C atom. The growth of epitaxial graphene and its structure on two different faces are very different from each other.

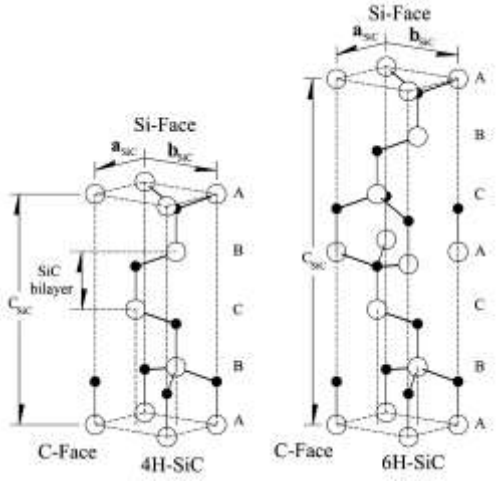

Figure 3. The unit cell structure of 4H- and 6H-SiC. Filled circles and open circles represent carbon and silicon, respectively. Lattice parameters of a_{SiC} and c_{SiC} for 4H-SiC are 3.0805 Å and 10.0848 Å and lattice parameters of a_{SiC} and c_{SiC} for 6H-SiC are 3.0813 Å and 15.1198 Å, adopted from Hass.[27, 45]

Due to the relationship between the grown epitaxial graphene and SiC lattice constants, there are various possible orientations of the epitaxial graphene lattice constants that lead to commensurate structures with SiC substrate. In this process, epitaxial graphene formation is initiated by the sublimation of sufficient Si atoms to leave behind the formation carbon-segregated surface containing mobile carbon atoms, during the heating either the C-face or Si-face surfaces in the range from 1000 °C to 1300 °C in ultra-high vacuum (UHV) or atmosphere pressure.[6a, 46] Rearrangement of those carbon atoms on the SiC surface at that high temperature forms layer of the large area epitaxial graphene film with a mobility of 2000 $cm^2V^{-1}s^{-1}$.[47] The low energy electron diffraction (LEED) pattern of the top-layer on the substrate is consistent with the surface of the graphite structure.[48] Additionally, the Auger peak of the over-layer on the substrate changed from the carbide character to a graphite character.[48b] The epitaxial graphene formation is specific to the different polar surfaces such as C-face and Si-face.[48a, 49] The graphene film grows much slower on Si-face than that on C-face[49c] and the graphene film grown on Si-face is epitaxial with an orientational phase with rotated 30° relative to the SiC surface, whereas graphene film grown on C-face can have multiple orientational phases.[48b, 50] Due to the multiple orientation of epitaxial graphene grown on C-face, the structural, growth, and electronic studies have mainly focused on epitaxial graphene grown on Si-face. Furthermore, this method allows the transferring a large area graphene film onto any arbitrary substrate by etching the underneath metals. This method is envisioned as a promising strategy for high quality and large area graphene growth. Graphene grown on dielectric surfaces directly *via* this particular process is another technological interest that would be beneficial for field-effect transistors (FET) or related devices in nanoelectronics.

1.3.4 Chemical Vapor Deposition (CVD) of Graphene

Based on the aforementioned explanation, graphene can be grown on metal surfaces by carbon segregation on the surface or rearrangement of carbon atoms on SiC substrate after sublimation of Si. In contrast to epitaxial graphene produced by thermal decomposition of SiC, where carbon precursor is already present in the substrate, for CVD, carbon precursor is fed in gas form and metal is used as a catalyst as well as a substrate to grow graphene. This technique has been considered as a promising and readily accessible approach for reasonably high quality and large area graphene production on transition metal substrates because of the availability of large metallic substrate in the form of thin films or foils. These metallic films/foils, however, are polycrystalline in nature and thus the individual grains are oriented in different directions forming grain boundaries. Thus, carbon segregation takes place relatively higher in grain boundaries as they are thermodynamically in higher energy state on polycrystalline material, and hence grain boundaries are the regions where graphene produced in higher thickness. Due to the nature of the substrate, graphene can grow on various crystallographic surfaces as opposed to epitaxial graphene grown on hexagonal metallic surface. CVD growth of graphene has been performed on various metallic substrates, but mostly practiced ones are Ni[51] and Cu.[52]

In a typical few layer graphene growth process, the substrate is first annealed with flowing Ar/H_2 gas around 1000 °C under low or atmospheric pressure in a furnace. The individual grains of the substrate grow bigger during annealing that eventually decreases the density of defects (wrinkle, folds, etc.) in the resulting graphene film. After annealing for a certain period of time, subsequently, both hydrocarbon molecules as a carbon precursor and H_2 gas as a carrier gas are supplied to deposit carbon on the transition metal substrates. Both hydrocarbon

molecules and H_2 gas flow are switched off once the growth of the graphene is done, and then the substrate cools down for carbon segregation on the surface to grow graphene film. Generally, the number of graphene layer grown through CVD technology can be determined several parameters such as active gas flowing rate, temperature, growth time, and substrate.[52-53] The thickness of graphene with the same growth time (20 minutes) on Ni substrate is affected by the cooling rate, with few layers graphene (3~4 graphene layers) being produced with a cooling rate of 10 °C/s. Faster cooling rate (20 °C/s) generates thicker graphene films due to a lack of time to diffuse carbon atoms to bulk, whereas slower cooling rate (0.1 °C/s) prevents carbon segregated from the Ni surface.[54] Finally, the substrate is etched away in aqueous $FeCl_3$ solution to allow graphene floating on the surface of etching solution. After subsequent cleaning, the graphene film is then transferred to the desired substrate.

CHAPTER 2

CHARACTERIZATION TECHNIQUES AND EXPERIMENTAL METHODS

2.1 X-ray Photoelectron Spectroscopy (XPS)

A solid or liquid surface could be defined in several different ways. The more precise definition is that a surface can be further specified the outer or topmost boundary of a matter. However, when getting down to the scope of the atomic level the term "boundary" loses its definition since the orbitals of bound electrons are highly diffused through three-dimensionally. The definition of the surface could be addressed that a surface is the region that dictates how the solid or liquid interacts with its neighbors. According to this particular definition, a surface can extent as little as one atomic layer (0.1-0.3 nm) to a couple of hundreds atomic layers (100 nm or more) depending on the material, its environment, and the physical or chemical property of interest. Applying the concept of this surface dimension for perspective, consider a strand of human hair. The diameter of the human hair can be in the range between 50 and 100 μm. If atoms composing the outer surface are as large as 0.2 nm in diameter, this cannot be viewed even under the most specialized optical microscope (typical magnification is up to ~300X) because the spatial resolution is diffraction limited to slightly less than 1 μm. In order to see it, very high magnification around 30,000,000X is required and very limited number of techniques can reach the magnification. One of the most common microscope tools is transmission electron microscopy (TEM). These concepts are represented in **Figure 4**.[55]

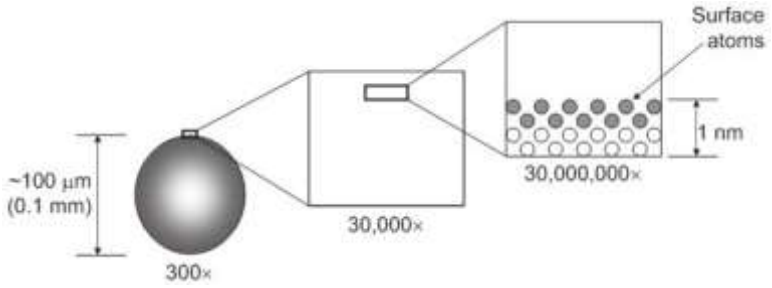

Figure 4. Illustration of the cross section of a strand of human hair at the various magnifications listed, adopted from Paul.[55]

XPS is one of the most powerful techniques and heavily used for chemical analysis of inorganic and organic surfaces and their interfaces (within the first 10 nm). The attraction of XPS stems from its ability to 1) identify and quantify the elemental composition of the surface around 10 nm in depth of any solid with all elements from Li to U detectable if elements exist higher than 0.05 atomic %, 2) know the chemical environment of elements exist, and 3) relative ease and minimal sample preparation. XPS is a study of the energy distribution of the photoelectrons from a surface of the X-ray irradiated compounds.

The kinetic energy of the photoelectrons from the surface of materials is measured by an electrostatic energy analyzer. XPS can study all electrons from core to valence levels. With knowledge of the X-ray excitation energy, the binding energy of the orbital from which an electron came can be evaluated using Einstein's equation for photoionization.[56] Siegbahn et al. discovered that the binding energies of the atomic levels could be shifted and distinguish the difference of the same elements in different chemical valence states. Therefore, the binding energies comprise information of the chemical state and the chemical environment of the elements.[57] As a result of the extensive study of the shift and the behaviors of the

binding energies, XPS has developed into a research tool of wide applications in chemistry and solid-state physics.[58]

A convenient source of characteristic X-rays is typically generated by electron bombardment of Mg or Al target that produces either MgKα; or AlKα. Aluminum and magnesium have narrow characteristic lines and MgKα or AlKα has the advantage that it can be readily monochromated.[59] When a material is irradiated by incident X-rays photoelectrons are emitted from the surface of the material. The emitted photoelectrons from the material are then focused (often with some retardation) into an energy analyzer that is generally of the electrostatic hemispherical type to obtain desired photoelectrons. After energy analysis, the electrons are detected by an electron multiplier array and recorded by a suitable electronics/data system. The X-ray source, specimen, lens, spectrometer and detector are all housed in an ultra-high vacuum environment in order to minimize contamination of the surface of the sample. The schematic illustration of basic components in XPS is shown in **Figure 5**.

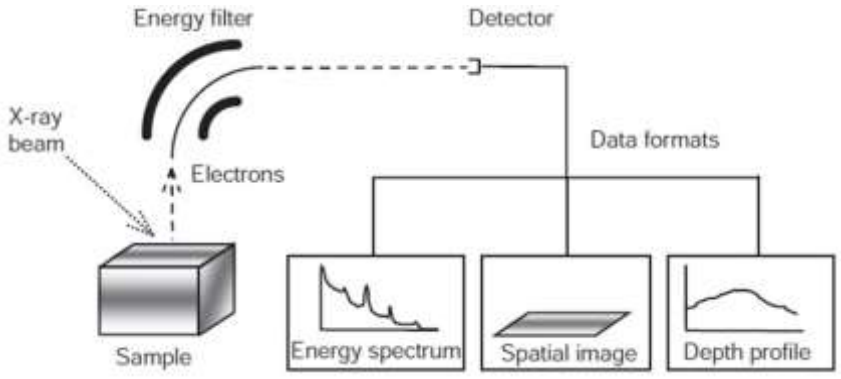

Figure 5. Schematic illustration of the basic apparatus in XPS, adopted from Paul.[55]

The basic processes of photoelectron spectroscopy are the followings: 1) the absorption of a quantum of energy, $\hbar v$, 2) ejection of an electron, and 3) measurement of the kinetic energy of the photoelectron ejected from the target

atom. In this process, incident photon energies transfer their entire energies to electrons in core level, and the element identification is provided by the measurement of the kinetic energy of the photoelectrons that escape from the material without energy loss. The schematic illustration of the photoelectron process from oxygen present within a silicon wafer is depicted in **Figure 6**.

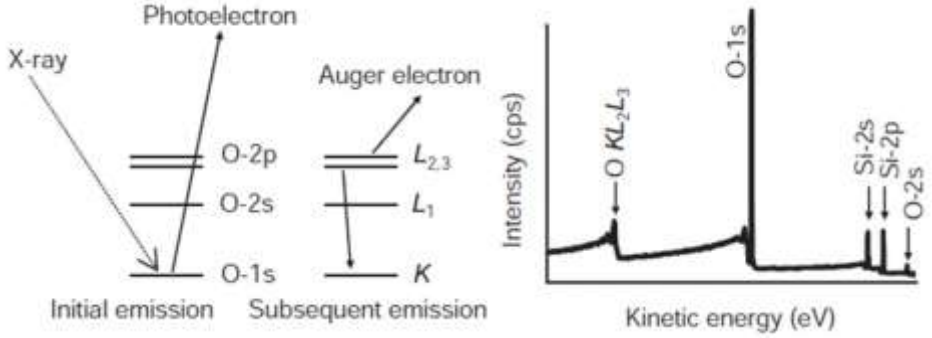

Figure 6. Schematic illustration of photoelectron process, adopted from Paul.[55]

During photoelectron process, X-ray-induced Auger emission also takes place because both photoelectrons and auger electrons are observed in XPS spectra. Even if X-rays can penetrate micrometers below the surface of materials, detectable photoelectrons produced by incident X-rays are typically around 10 nm in depth. If photoelectrons lose their energy, the signal will disappear within the spectral background. This happens for all photoelectrons produced by atoms or ions situated at some depth deeper than around 10 nm below the surface. Therefore, the discrete signals shown in the XPS spectrum are mainly from only the surface region. The presence of adsorbed layers on the surface could act to quench, to some extent, all signals from the underlying adsorbed layers. The general schematic photoelectron emission process is depicted in **Figure 7**.

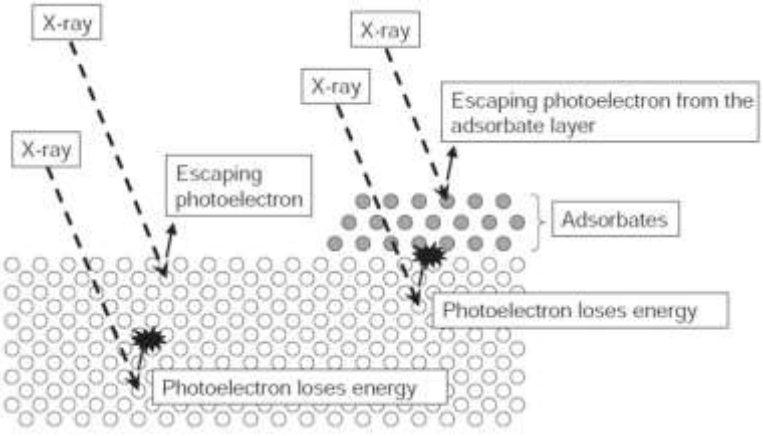

Figure 7. Pictorial illustration of the photoelectron emission process from a solid material and an adsorbates layer, adopted from Paul.[55]

XPS technique can be very useful in studying the functionalization of carbonaceous materials. XPS has been widely used to determine not only composition of materials but also functional groups covalently bonded to the materials. To date, XPS has been used for elemental analysis of graphite oxide (GO), reduced graphite oxide (RGO), and chemical functionalized activated carbon.[60] The High-resolution C1s XPS spectrum of GO and oxidized activated carbon shows larger full-width at half maximum (FWHM) peaks and new peaks in higher binding energies that were not seen with graphite and activated carbon.[61] These results indicate that the environment of the carbon atoms significantly changed and this is a strong evidence of oxygen functional groups incorporated into the carbon matrix. Nitrogen doped reduced graphene oxide is also studied by XPS and high-resolution C1s XPS spectrum showed a big difference between N-doped RGOs and undoped ones as well as XPS spectrum of N-doped RGOs shows new peaks around 400 eV that is assigned to C-N bonding.[62]

2.2 Raman Spectroscopy

Raman spectroscopy, named after C. V. Raman,[63] is one of the most important and powerful tools in studying the structure and properties of carbon products. The Raman spectroscopy measurement does not require any sample preparation, and the studied sample can be analyzed in a fast and non-destructive manner. This technique is based on the measurement of inelastic scattering of light that is the scattering of light in which the energy of the photon changes, and consequently corresponds to shifts from the frequency of the incident light. By exposing a sample to a monochromatic beam of light, electrons are excited from the ground state to the virtual state by absorbing photons. These electrons will scatter by either emitting or absorbing phonons, and finally relax to the ground state by emitting photons. Most of the light is elastic scattering (i.e. Rayleigh scattering) while only a minority is inelastic (i.e. Stokes or anti-Stokes) scattering, so called Raman scattering.

Raman spectroscopy is the most useful technique for all forms of carbon including graphite derivatives such as graphite oxide or reduced graphite oxide, fullerene, carbon nanotubes, amorphous carbon, polycrystalline carbon, diamond, etc.[64] Different forms of carbons have different position, width, and relative intensity of bands. With only considering the position of G band (~ 1580 cm^{-1}) and the I_D/I_G intensity ratios, the Raman spectra of all kind of carbon materials could be described within three-stage model of increasing disorder shown in **Figure 8**.[65] The G band position and I_D/I_G ratios could be affected by a degree of amorphization of carbon materials and the sp^2 domain size as well.

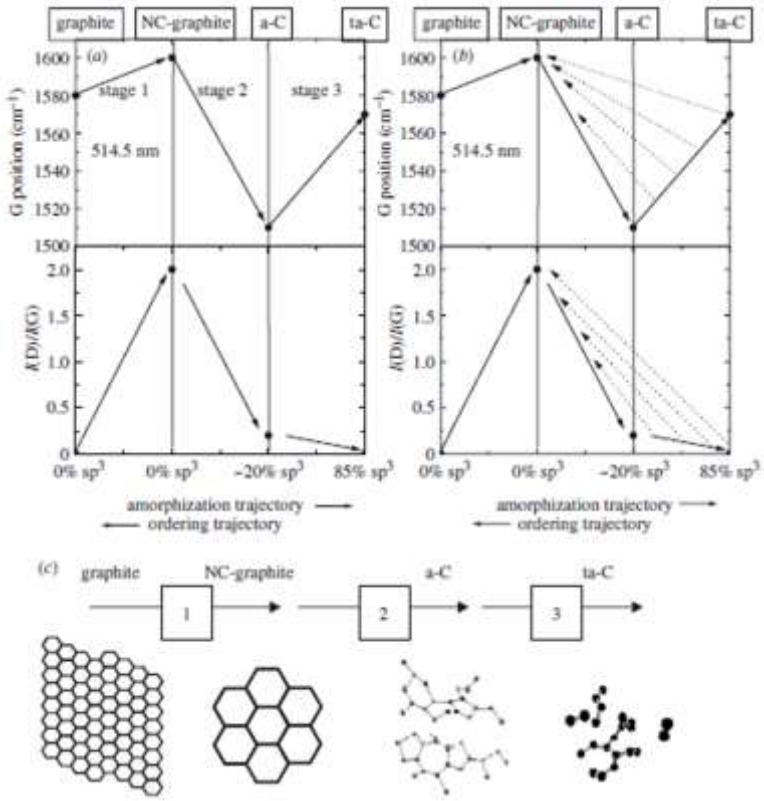

Figure 8. Three-stage model of the variation of the Raman G band and I_D/I_G ratios with increasing disorder, adopted from Ferrari.[65]

Several important bands from various carbonaceous materials that can be found in a Raman spectrum are described below: 1) a low-frequency peak < 200 cm^{-1} assigned to A_{1g} radial breathing mode (RBM) which is a characteristic of the single-wall carbon nanotube, 2) a higher frequency feature around 1340 cm^{-1} assigned to residual ill-organized graphite, the so-called D band, 3) a high frequency peak around 1580 cm^{-1} called G band which is a characteristic of all graphitic materials, corresponding to the doubly degenerated zone center E_{2g} stretching mode of graphite,[66] and 4) a second order scattering between 2450 and 2600 cm^{-1} assigned to the first overtone of the D band and historically called G' band.[67] The D band around 1340 cm^{-1} is a breathing mode of A_{1g} symmetry involving phonons near the K

zone boundary shown in **Figure 9**. This mode is forbidden in perfect graphite and only becomes active in the presence of disorder. Additionally, the G band of graphite around 1580 cm^{-1} has E_{2g} symmetry and its eigenvector shown in **Figure 9**. Using Raman spectroscopy, it is possible to study not only atomic structure and electronic properties but also a degree of lattice deficiency of carbonaceous materials.

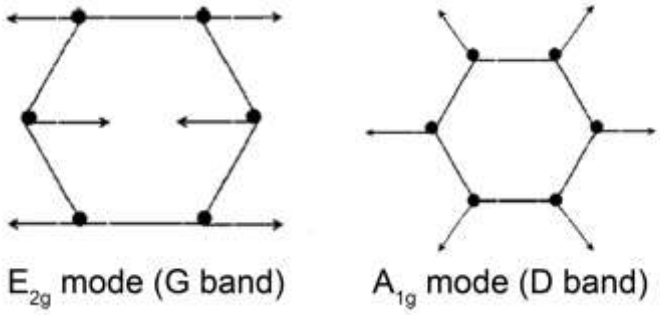

Figure 9. Carbon motions in the E_{2g} mode (left) and A_{1g} mode (right), adopted from Ferrari.[65]

2.3 Powder X-ray Diffraction (PXRD)

In fact, X-rays had been generated before Wilhelm Conard Röntgen who was awarded a Nobel Prize discovered. In the 1880s, experiments with cathode ray tubes had been popular and X-rays were generated by those experiments.[68] Röntgen used a gas filled cathode ray tube to study fluorescence produced when cathode rays struck the glass wall of the tube. He noticed a glow on a plate covered with barium platinocyanide some distance away in the darkened room. He speculated that the invisible radiation was passing through air from the tube to the screen. He called the radiation as X-ray.[69] Many scientists tried to understand the nature of X-rays and many attempts carried out but it was very difficult to do experiments due to handing with very short wavelength.[70] In 1912, the experiment performed by Max von Laue confirmed that X-rays show wave character by

diffraction experiments from single crystal.[71] After discovery of X-rays, X-ray radiography, X-ray crystallography, and X-ray spectrometry have developed from the use of this radiation.[72] First, X-ray has been used to photograph foreign bodies such as bullets, and coins inside the body. The biological effects of X-rays were not appreciated at first. After many scientists studied the risks of X-ray nowadays X-ray has been used accordingly. Second, following the discovery of X-rays, X-rays encouraged scientists to study crystalline structure in atomic level using X-ray diffraction. Third and last, X-ray spectrometry is one of the fundamental roots but this has developed into a routine technique in the last 20 or 30 years.[72]

These days, X-ray diffraction is one of the most powerful and important characterization techniques used in solid state chemistry and materials science. Especially, the powder X-ray diffraction (PXRD) method is of special importance because this method is the only technique that is readily applicable to all crystalline materials. Moreover, PXRD is the most convenient method for obtaining diffraction data from crystalline materials. Diffraction data depending on lattice parameters of substances are unique for each crystalline material. Therefore, crystalline materials can be identified by X-ray powder pattern that may be used as a "fingerprint". Once the material has been identified, X-ray crystallography may be used to determine its structure, i.e. how the atoms pack together in the crystalline state, and what the interatomic distance and angle are, and so on. PXRD technique can be the easiest and fastest way to identify materials. In this method, samples are polycrystalline form and thus crystallites are randomly orientated with respect to given directions and thus all possible lattice planes are shown in PXRD pattern.[73] After taking PXRD pattern the interplanar spacing d can be calculated using Bragg's law because the characteristic X-ray (normally CuKα) is used. Bragg's law is shown in **Equation 1**.

$$2d_{(hkl)} \sin\theta = n\lambda \qquad \textbf{Equation 1}$$

where $d_{(hkl)}$ is the interplanar spacing between atomic lattice, θ is an angle between the incident X-rays and scattering planes, n is integer order of reflection, and λ is wavelength of incident X-ray.

X-ray diffraction analysis is an important method for studying a degree of crystallinity in carbon materials.[74] Various carbon materials show a different degree of crystallinity from amorphous carbon such carbonaceous materials pyrolyzed organic materials at low temperature to well crystalline carbon such graphite. The fraction of amorphous carbon (χ_A), aromaticity (f_a), interlayer spacing of crystalline structure (d_{002}), and crystallite sizes (L_a and L_c) have been established as structural parameters for evaluating the carbon stacking structure.[75] Highly crystalline carbon material like graphite shows several sharp and intense Bragg's peaks but turbostratic carbon or amorphous carbon shows very different XRD patterns. By comparing full-width at half maximum (FWHM) and intensity of (002) Bragg's peak, it would be easily to distinguish between well crystalline carbon materials and poor crystalline carbon materials.

2.4 Electron Microscopy

Electron microscopy is a very useful technique for analysis of morphological features of samples using a beam of highly energetic electrons to examine objects on a very fine scale. This technique can provide different types of information such as the topography, morphology, composition, and crystallographic information. Electron microscopes were developed to overcome the resolution limitation of optical microscopes. The resolution of optical microscopes is proportional to light wavelength and thus the optical microscopes can only magnify as much as 500x or 1000x magnification and a spatial resolution of 0.2 um according to **Equation 2**.

The spatial resolution of electron microscope, however, is in the range from 2 to 5 Å.[76]

$$d = 0.61\lambda/\text{N.A} \qquad \textbf{Equation 2}$$

where, d is minimum distance between resolved points, λ is wavelength of light, N.A is the numerical aperture.

In the early 1930s, this theoretical limit had been reached and scientists wanted to see the fine details of the morphology of organic cells. This required higher than 10,000x magnification that was not possible with optical microscope. The transmission electron microscope (TEM) was the first type of electron microscope to be developed and basic principle is exactly the same as the light transmission microscope except that a focused beam of electrons is used instead of light to see through the samples. It was developed by Max Knoll and Ernst Ruska in Germany in 1931.[77]

The first scanning electron microscope (SEM) was developed in 1942 and it was the first commercial instruments around 1965. Its late development was mainly due to the electronics involved in "scanning" the beam of electrons across the sample.[78] Electron microscopes perform exactly the same as their optical counterparts except that they use a focused beam of electrons instead of light to "image" the specimen. The basic steps of both TEM and SEM are the following: 1) a stream of electrons is formed and accelerated in high vacuum, 2) these accelerated electrons impinge on the specimen, 3) the accelerated electrons pass through metal apertures and magnetic lenses into a thin, focused, monochromatic beam, and 4) the sample is irradiated by the accelerated electrons and interactions occur inside the irradiated sample. These interactions are detected and transformed into an image.[76, 78] It must be noted that TEM and SEM measure different type of signal and provide images in a different way. For TEM, an image is produced by transmitted electrons

and thus very thin sample preparation is required. For SEM, the accelerated electrons impinging on the sample can generate secondary electrons from the sample and the secondary electrons are collected to provide images.

2.5 Thionation

Thionation means that an oxygen atom in the compound is replaced by sulfur atom. Thionation of various organic molecules has been widely studied because organosulfur compounds are valued not only for their rich and varied chemistry, but also for many important biological properties.[79] Thionation has been mainly performed through thionating agent, and phosphorous decasulfide (P_4S_{10}, also called P_2S_5) is the oldest and the most important agent among various thionating ones.[80] Synthesis of P_4S_{10} was reported for the first time by J. Berzelius in 1843; since then P_4S_{10} is also called Berzelius reagent. Another widely used thionating reagent is Lawesson's reagent (LR) because of excellent product yields. However, aside from its high cost, LR has huge disadvantage that by-products produced from the reagent cannot be removed through general purification procedure. In order to remove the by-products, chromatography on silica gel must be used. The molecular structures of phosphorous decasulfide and Lawesson's reagent are represented in **Figure 10**.

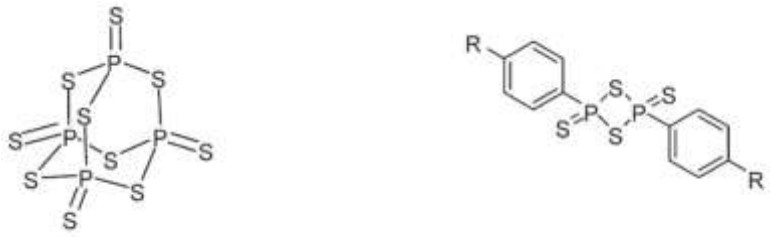

Figure 10. Molecular structures of P_4S_{10} (left) and Lawesson's reagent (right).

Due to the aforementioned issue, P_4S_{10} has been applied for syntheses of a wide range of purposes, mainly as a thionating agent of organic and inorganic compounds. Various experiments have been carried out by utilizing P_4S_{10} as a thionating agent, and the results indicate that P_4S_{10} can convert almost all kinds of oxygen functional groups into organic molecules.[81]

2.6 Solvothermal Reaction

To synthesize nano-sized inorganic materials with high crystallinity, solution-processed syntheses are preferred. These synthetic reactions are typically carried out at relatively low temperatures, thus requiring low energies. The sol-gel reaction is one of these methods. Sol-gel method, however, usually gives amorphous products, and calcination of the products is required to generate well-defined morphologic products.[82]

Recently, the use of organic media for nano-sized inorganic materials synthesis has attracted much attention. Since 1984, the synthesis of inorganic materials in organic media has been exploring at elevated temperatures (200 to 300 °C) under autogenous pressure of the organic solvent.[83] This technique is now generally called the "solvothermal" reaction. The term "solvothermal" means that reactions occurred in liquid or supercritical media at temperatures higher than the boiling point of the medium.[84] The pressure generated in the vessel (autoclaves) due to the organic medium vapors elevates the boiling point of the solvent. Therefore, the temperatures higher than the boiling point of the solvents could be created. Hydrothermal reaction is a kind of solvothermal reaction. In order to accomplish reactions at elevated temperatures under high pressure, pressure vessels are usually required. Alternatively, sealed ampoules of glass or silica as a pressure vessel can be used for solvothermal reaction, but these experiments should be

carried out with great precaution because the ampoules could be easily broken by the internal pressure generated by the organic solvents. To avoid explosion of the ampoules, they may be placed in an autoclave together with suitable organic medium to create a vapor pressure to balance the internal pressure of the ampoule.

The high pressure and temperature generated during synthesis facilitate the interaction of precursors. Due to the high-pressure employed, one often obtains high-pressure phases of the materials, and the solvothermal method can also be used to prepare thermodynamically stable and metastable states including novel materials that cannot be easily formed from other synthetic routes. In the last decade, solvothermal reaction route has emerged to become the chosen method to synthesize nanocrystals of inorganic materials.

It must be noted that the liquid structure of the organic medium is essentially unchanged at above or below the boiling point because the compressibility of the liquid is very small. Higher pressure generated during the solvothermal reaction may facilitate or retard the reaction rate depending on the relative volume of the activated complex at the transition state to the volume of the starting molecules. However, it has been known that to measure the effect of reaction pressure, GPa-scale pressure is required. This implies that the autogenous pressure created by the vapor pressure of the organic medium has only a minor effect on the reaction rate. Therefore, it should not affect the reactions whether the temperature is above or below the boiling point of the solvents. Consequently, "solvothermal" reaction should be defined more broadly as the reaction in a liquid medium at high temperatures. The results from reactions in a closed system using Teflon-lined autoclaves and in an open system using a flask equipped with a reflux condenser are sometimes completely different from each other, especially when a byproduct such as water is produced during the reaction.

Various compounds have been synthesized through solvothermal reactions route: metals,[85] metal oxides,[86] chalcogenides,[87] nitrides,[88] phosphides,[89] open-framework structures,[90] oxometalate clusters,[91] organic-inorganic hybrid materials,[92] and even carbon nanotubes.[93] Most products produced by solvothermal reaction are nano- or micro-particles with well-defined morphologies. The distribution of the particle size of the product is typically fairly narrow, and mono-dispersed particles are frequently formed. When the solvent molecules or additives are favorably adsorbed on a certain surface of the products, growth of the surface can be prohibited and thus products with unique morphologies may be generated by the solvothermal reaction route.[94] Therefore a wide range of morphologies of the products such as nanorods, wires,[94] tubes,[95] and sheets[96] has been obtained through solvothermal reaction route.

CHAPTER 3

CONCOMITANT THIONATION AND REDUCTION OF GRAPHENE OXIDE THROUGH SOLID/GAS METATHETICAL SULFIDATION REACTIONS AT HIGH TEMPERATURES

3.1 Introduction

Chemical reduction and/or functionalization of graphene oxide (GO) is important as a promising strategy in manipulating the physical and chemical properties of graphene and in further providing new graphene-based hybrid materials.[28b, 97] Among various methods,[97a, 97d, e] covalent functionalization can provide permanent functional groups covalently linked to the surface of GO sheets, mainly by utilizing carboxyl groups as a linking unit. For example, covalent-functionalized GOs were obtained by using porphyrin,[97e] adenine,[98] long-chain alkyl amine,[97b] and aryl diazonium salt.[97d] The hydroxyl groups on GO have been also utilized as a cross linker for organic isocyanates.[97a]

Most of the chemical treatments of GO are carried out with a regent usually in an aqueous medium.[99] Meanwhile, chemical modifications of GO at high temperatures are relatively rare in the literature. One reason for this can be because of the relatively scarce availability of reagents that are suitable for high-temperature reactions of GO. Indeed, the well-established high temperature reduction method for GO does not employ any chemicals but relies on the explosive evaporation of water and other gaseous molecules during the rapid heating of GO.[39, 100] Further exploration of high-temperature reactions may lead to new synthetic methodologies for new GO derivatives that can have unique properties.

Herein, I report a high-temperature solid/gas metathetical method for graphene oxide which produces thionated reduced graphene oxides (hereafter called "mercapto graphene oxide (m-RGO)") with a thiol content over about 24 wt% (from nonhydrogen elements only). The thionation reagent for GO in this high temperature

method is boron sulfides (BS_n, n = 1.5 ~ 2) which in previous work have shown to be unique in metal sulfide formation from their corresponding oxides.[101] Compared to other sulfurization reagents such as H_2S and CS_2, gaseous boron sulfides can be effective at temperatures as low as 350 °C, especially under vacuum. Metathetical reactions of the boron sulfides are favored particularly when oxides are used for metathetical sulfidation. The large formation energy of the vitreous B_2O_3 byproduct ($\Delta G_f°(v\text{-}B_2O_3) = -1182.5$ kJ/mol),[102] as compared to those of boron sulfides ($\Delta G_f°(v\text{-}B_2S_3) = -247.6$ kJ/mol; $\Delta G_f°(v\text{-}BS_2) = -120$ kJ/ mol),[103] makes the sulfidation thermodynamically favorable for a variety of metal oxides. In addition, the method allows nanoparticles to maintain their small particle sizes[101a] and it can even break up microparticles into nanoparticles.[101b] This has been attributed to the formation of $v\text{-}B_2O_3$ byproduct which is in a liquid state at the reaction temperature and thus acts as a passivation coating around sulfide nanoparticles, effectively preventing nanoparticles from fusing and growing.[101]

In application of the method for GO in the work, the boron sulfides are produced *in situ* in an evacuated reaction container in which GO is heated at high temperatures.[101] The high-temperature reaction condition allows a simultaneous reduction of GO, and yet the m-RGO products are remarkably well dispersible in water and various solvents, indicating less significant restacking of the graphene sheets even under the employed high temperature condition. In addition to chemical, microscopic, and spectroscopic characterizations, the quantity of the reactive thiol groups in the products was probed by employing disulfide formation reaction with Ellman's reagent.

3.2 Experimental Section

3.2.1 Synthesis of Graphene Oxide (GO)

GO was synthesized by a modified Hummers method through oxidation of graphite powder.[34] In a typical procedure, 1 g of graphite flake (Sigma-Aldrich) was ground with 5 g of NaCl (Alfa Aesar, 99+%) until the mixture becomes homogeneous by visual inspection. NaCl from the mixture was then washed away using deionized water with vacuum filtration. The ground graphite on the filter paper was dried at 110 °C in a lab oven for 2 h. 0.765 g of $NaNO_3$ (Sigma-Aldrich, ≥ 99.0%) was dissolved in 40 mL of concentrated H_2SO_4 (Sigma-Aldrich, ACS reagent, 95 ~ 98%) in a 400 mL beaker with stirring. 1 g of the ground graphite was then added to the beaker. Afterward, the beaker was placed in an ice bath and 5 g of $KMnO_4$ (Sigma-Aldrich, ≥ 99.0%) was slowly added to the beaker while the temperature was kept below 10 °C. The mixture was heated at 35 ~ 40 °C with vigorously stirring until it became pink thick paste. 100 mL of deionized water was added to the beaker and 20 mL of H_2O_2 (Alfa Aesar, ACS reagent, 29 ~ 32%) was slow added to the suspension subsequently. After the reaction, the color of the suspension became bright yellow. The suspension was then repeatedly centrifuged and washed with diluted HCl until $BaCl_2$ (Anhydrous purified, J.T. Baker chemical Co.) test shows a negative result.

3.2.2 Synthesis of Mercapto Reduced Graphene Oxide (m-RGO)

Sulfidation of GO was performed by modifying previously reported solid/gas sulfidation method for metal oxides, where gaseous boron sulfides (BS_n) are generated *in situ* from elemental boron and sulfur.[101] Multiple samples were prepared with various reaction temperatures and amounts of GO with respect to boron and sulfur precursors while the B:S atomic ratio was fixed at 1:2 (**Table 1**).

The oxygen amounts in the reaction mixtures were estimated solely from the relative amounts of oxygen in GO estimated from the X-ray photoelectron spectroscopy results without taking into account the presence of hydrogen atoms.

Hereafter, the description of synthesis is given by using Sample 3 in **Table 1** as a representative example. Typically, about 0.2 g of GO dispersed in deionized water (0.1 wt%, pH ~ 1) was mixed with 130 mL of 1 *M* NaOH aqueous solution. The solution was centrifuged and the supernatant was decanted. 0.0900 g of amorphous boron powder (Alfa Aesar, 99.99%, 325 mesh) and 100 mL of deionized water were added to the precipitate and the mixture was sonicated until it became homogeneous by visual inspection. The mixture dispersion was then dried in a lab oven at 110 °C overnight. 0.5347 g of sulfur powder (Alfa Aesar, 99.999%) was mixed with the dried precipitate and the mixture was subsequently placed in a fused silica tube (11 mm I.D.). After the silica tube was evacuated (~10^{-6} torr) and flamed-sealed, the mixture in the silica ampule was gradually heated at 100 °C/hr to 500 °C, kept for 10 hrs, and radiatively cooled to room temperature. After the reaction, the silica ampule was intact, and there was no visible indication of corrosion on the inner surface.

Once the product was taken out after breaking the silica ampule, it was ground and sonicated in carbon disulfide to wash off the unreacted sulfur. After centrifugation and decantation, the precipitate was dried in air. The product was then repeatedly washed with degassed hot water (~80 °C) until the supernatant became colorless, in order to remove unreacted boron sulfide and the by-product B_2O_3. 2 mL of 12 wt% sodium borohydride ($NaBH_4$) (Fluka) in aqueous 14 *M* NaOH solution was added to the product and then the mixture solution was sonicated for 10 min. The solution became green, indicating presence of polysulfide liberated from the product. This was repeated a couple of times until the color of the supernatant

solution became colorless. A sufficient volume of 1 *M* HCl solution was added to the solution to give a final pH of about 1. The solution was then centrifuged and decanted. The precipitate was rinsed multiple times with deionized water and subsequently washed with N,N-Dimethylformamide (DMF) (Alfa Aesar, anhydrous, amine free, 99.9%) and sonicated for 40 min in DMF. After centrifugation at 10,000 rpm for 10 minutes, the supernatant was collected to obtain dispersion.

As a control, GO was thermally treated in the same way but without adding boron and sulfur, and the product is called ttGO (thermally-treated GO) hereafter. The purification of ttGO was carried out by washing the reaction product with degassed hot water (~80 °C) and drying it in a lab oven.

3.2.3 Materials Characterization

Powder X-ray diffraction data were collected using a Siemens D5000 diffractometer with Cu-Kα radiation. Thermogravimetric analysis (TGA) studies were performed using a Mettler-Toledo TGA/DSC 1 STARe system. Samples were analyzed by heating from 25 to 800 °C at 5 °C·min^{-1}. All analyses were carried out under an Ar flow at 60 mL·min^{-1} with 70 µL-capacity alumina crucibles. Elemental analysis was performed with ground and air-dried samples using energy dispersive X-ray spectrometer (EDS) attached to an FEI XL-30 scanning electron microscope at 10 keV. For each sample, 13 different places were examined to obtain average chemical compositions. Transmission electron microscopic (TEM) studies were conducted using a JEOL 2000FX at an accelerating voltage of 200 kV. TEM samples were prepared by dipping a copper grid covered with a holey carbon film into an aqueous m-RGO dispersion, and subsequently taking out and drying it in air.

X-Ray photoelectron spectroscopic (XPS) studies were carried out using a ThermoFisher VG 220i-XL spectrometer with a monochromated Al Kα radiation

(1486.6 eV, line width = 0.8 eV). The pressure in the analyzing chamber was kept at the level of 10^{-9} torr while recording the spectra. The spectrometer had the energy resolution of 0.4 eV. All the binding energies were corrected with respect to C(1s) at 284.6 eV. Deconvolution of the high-resolution spectra was carried out using the CASA software with the accuracy of 0.2 eV and a 70% Gaussian-30% Lorentzian peak shape after performing a Shirley background correction. For the C1s spectra, deconvolution was carried out with C–C (sp^2- and sp^3-hybridization peaks at 284.7 and 285.4 eV, respectively),[37] C–O (hydroxyl, carbonyl, and carboxylate peaks at 286.3, 287.4, and 289.2 eV, respectively).[104] Carbon atoms with the C–S bond were not separately treated because the C1s binding energy of C–S (285.3 eV)[105] is too close to that of C–C (sp^3-hybridization) and thus could not be resolved, given the resolution of the XPS instrument (0.4 eV). The O1s spectra were deconvoluted with three functional groups, C═O (531.6 eV), C–OH (532.7 eV) and C–O–C (533.6 eV).[106] The S2p spectra were deconvoluted with three functional groups; C–SO_3 ($S2p_{3/2}$ at 167.8 eV with FWHM of 1.8 eV; $S2p_{1/2}$ at 168.9 eV with FWHM of 1.8 eV),[107] C–SH ($S2p_{3/2}$ at 164.0 eV with FWHM of 1.1 eV; $S2p_{1/2}$ at 165.2 eV with FWHM of 1.1 eV)[108] and C═S ($S2p_{3/2}$ at 162.0 eV with FWHM of 1.3 eV; $S2p_{1/2}$ at 163.2 eV with FWHM of 1.4 eV).[109] The area ratio for the $S2p_{3/2}$ and $S2p_{1/2}$ spin-orbit doublet peaks was fixed at 2:1 for all the sulfur species. Other sulfur functional groups such as thiophene ($S2p_{3/2}$ at 163.8 eV)[110] and thioester ($S2p_{3/2}$ at 163.5 eV)[111] were not included, as they do not appear in the spectra.

A Nicolet 6700 FTIR spectrometer (Thermo Scientific Nicolet) was used to collect attenuated total reflectance (ATR) FTIR spectra of ethanol and supernatant solutions of m-RGO dispersed in ethanol. Drops of each sample solutions were placed on a diamond plate for the measurements. All spectra were calibrated against an air spectrum. Drops of each sample were placed in contact with

attenuated total reflectance (ATR) on a multibounce plate of diamond. All spectra were rationed against a background of an air spectrum. UV-Vis measurements were performed using a Hewlett-Packard 8453 spectrophotometer using quartz cuvettes with a 1-cm path length. For the measurements, aqueous solutions of GO and m-RGO were prepared by dispersing air-dried GO and m-RGO powders by sonication for 1 hour, centrifuging at 6000 rpm for 10 min and collecting supernatant solutions. The Raman data were collected using a custom-built Raman spectrometer in 180° geometry. Air-dried sample powders were sprinkled on a glass slide and the measurements were performed at room temperature using a 0.5 mW Compass 532 nm laser. The laser power was controlled using neutral density filters. The laser was focused onto the sample using a 50X superlong working-distance Mitutoyo objective with a numerical aperture of 0.42. The signal was discriminated from the laser excitation using a Kaiser laser band pass filter followed by a Semrock edge filter. The data were collected using an Acton 300i spectrograph and a back thinned liquid nitrogen cooled CCD detector (Princeton Instruments).

3.2.4 Quantitative Analysis of Thiol Funtional Groups on m-RGO

Ellman's reagent [5,5'-dithiobis(2-nitrobenzoic acid), DTNB] (Sigma-Aldrich, ≥ 98 %) and L-cysteine (Spectrum Chemical Mfg. Corp., ≥ 98 %) were used as received without further purification. All the solutions and dispersions were prepared by using Millipore water (18.2 MΩ·cm). 7.92 mg of DTNB was dissolved in 10 mL of 4-ethylmorpholine (Sigma-Aldrich, ≥ 97 %) buffer solution (50 m*M*, pH 7.6) to prepare a 2.0 m*M* DTNB stock solution. 1.32 mg of m-RGO was added separately to 1 mL of water and sonicated for 30 min. 100 µL of the resulting m-RGO dispersion was added to a mixture of 750 µL of water, 50 µL of 2.0 m*M* of the DTNB solution and 100 µL of Tris-HCl buffer (0.1 *M*, pH 8.0) and vortexed thoroughly to prepare a

homogeneous 1 mL mixture solution. The mixture solution was allowed to stand for 30 seconds and was centrifuged to remove m-RGO particles before measuring its UV-Vis absorbance. Standard L-cysteine solutions were prepared freshly just before the experiment. Typically, 5.0 mg of L-cysteine was dissolved in 10 mL of Millipore water. This solution was then diluted with water appropriately to prepare 1.0, 1.8, 2.5, and 3.7 μ*M* solutions. 100 μL of each solution was used in place of the sample m-RGO dispersion to produce five standard thiol solutions and finally to obtain a calibration curve by using the absorbance values at 413 nm.

3.3 Results and Discussions

The mercapto reduced graphene oxide (m-RGO) has been synthesized through metathetical sulfidation reaction between GO and *in situ*-formed boron sulfides. Graphene oxide (GO), amorphous elemental boron, and sulfur were placed in a fused silica tube, evacuated, flamed-sealed, and heated at 350 or 500 °C for 10 hrs. Following our previous work,[101] the reaction of GO with boron sulfides can be given in the **Equation 3**,

$$C_xH_yO_z{\cdot}mH_2O(s) + pBS_n(g) \rightarrow C_{x'}H_{y'}O_{z'}S_{z''}(s) + (p/2)B_2O_3(v) + (x - x')CH_aO_b(g) + ((y - y')/2 + m)H_2S(g), \quad \textbf{Equation 3}$$

where GO's chemical formula is expressed as $C_xH_yO_z{\cdot}mH_2O$ in which H_2O represents the water molecules present in the galley of GO sheets. The typical amount of water in dried GO ranges from 10 to 20 wt%.[28c, 112] Graphene oxide (GO) undergoes thermal decomposition[39a] to a great extent, giving various small gaseous carbonaceous molecules whose chemical formulas are collectively represented as CH_aO_b in the **Equation 3**. The consequent decrease in the oxygen content in GO sheets is responsible to the reduction of GO (i.e., thermal reduction).[39a, 100] Boron

sulfides would react with GO sheets to lead to partial substitution of oxygen atoms in the GO sheets with sulfur, producing $C_{x'}H_{y'}O_{z'}S_{z''}$ and vitreous boron oxide byproduct. Based on our previous studies for metal sulfide synthesis from metal oxide nanoparticles,[101] it is speculated that the vitreous boron oxide byproduct may act as a passivation coating between m-RGO sheets, avoiding significant restacking of the sheets during the reaction. After the reaction, the boron oxide is conveniently removed from the product by washing in water or ethanol.

Table 1 shows the reaction conditions and the C:O:S atomic ratios of the resulting m-RGO products obtained from XPS results (see below for details). Two different loadings of boron sulfide precursors were tested while the B:S atomic ratio was fixed at 1:2 for all the experiments. B_2S_3 and BS_2 are the only stoichiometric boron sulfides that have been known in the literature and the employed B:S ratio is the one that corresponds to the sulfur-richer compound, BS_2. The composition was chosen to provide the largest amount of reactive sulfur atoms bound to boron under the *in situ* formation condition effective above 350 °C. All the reactions except one were carried out at 500 °C. In **Table 1**, the loadings are expressed by the atomic ratios of the oxygen in the dried GO and the boron and the sulfur in the precursor mixtures, for which the amount of oxygen in the dried GO precursor was estimated from XPS results. The loading at the O:B:S ratios of 1.67:1:2 would generate a slightly excess amount of boron sulfides compared to what is expected for the stoichiometric formation of B_2O_3 (O:B = 1.5:1). Another loading (O:B:S = 0.67:1:2) was chosen to examine the effect of the excess presence of boron sulfides in the reaction. In **Table 1**, it is found that the degree of reduction and sulfidation is not affected significantly by the different loadings, as the resulting products (Samples 1 – 6 in **Table 1**) have similar C:O:S ratios (~20:1:~2), although the Sample 3 showed the largest amount of sulfur. All the subsequent characterizations were

performed for Sample 3. Two different heating rates, 100 and 250 °C/hr were tried and they didn't show significant differences in the resulting compositions. Rapid heating conditions, which are typically achieved by inserting the reaction container in a hot furnace,[39b] were not attempted due to the potential danger of breaking the container and subsequent emission of toxic H_2S gas. Meanwhile, a reaction at 350 °C, the lowest temperature that still can produce gaseous boron sulfides,[113] resulted in a lower amount of sulfur (O:S = 1:1.3) and a less degree of thermal reduction (C:(S+O) = 3.3) in the product. All the products from the reactions at 500 °C showed the C:(S+O) ratios from 5.3 to 7.1, which is similar to a previous report where the RGOs produced by thermal treatment at 500 °C under an argon or H_2 flow were found to have the C:O ratios from 6.9 to 7.3.[100]

Table 1. Atomic compositions of the mercapto reduced graphene oxide from different reaction conditions.

Sample	Synthetic condition			Atomic composition	
	O:B:S	Temperature (°C)	Ramping rate (°C/hr)	C:O:S	C/(S+O)
1	1.67:3:6	500	100	22:1:2.1	7.1
2	1.67:3:6	500	250	20:1:2.0	6.7
3	0.67:3:6	500	100	17:1:2.2	5.3
4	0.67:3:6	500	250	19:1:2.0	6.3
5	0.67:3:6	350	100	7.6:1:1.3	3.3

Figure 11 shows the dispersions of GO, ttGO, and m-RGO in deionized water, ethanol, acetone, N,N-dimethylformamide (DMF), and propylene carbonate (from left to right). Propylene carbonate was chosen because of its large dipole moment (4.9

Debye) and thus its potential as a good solvent. The dispersions were prepared by ultrasonication for 1 hr and left unperturbed for 3 months before taking the photographs. After the long settling period, GO particles precipitated out from all the solvent except water. Meanwhile, complete precipitation is observed for ttGO particles in water, ethanol, acetone and propylene carbonate. Although not clear in the photograph, a significant amount of ttGO was found at the bottom of the ttGO/DMF dispersion.

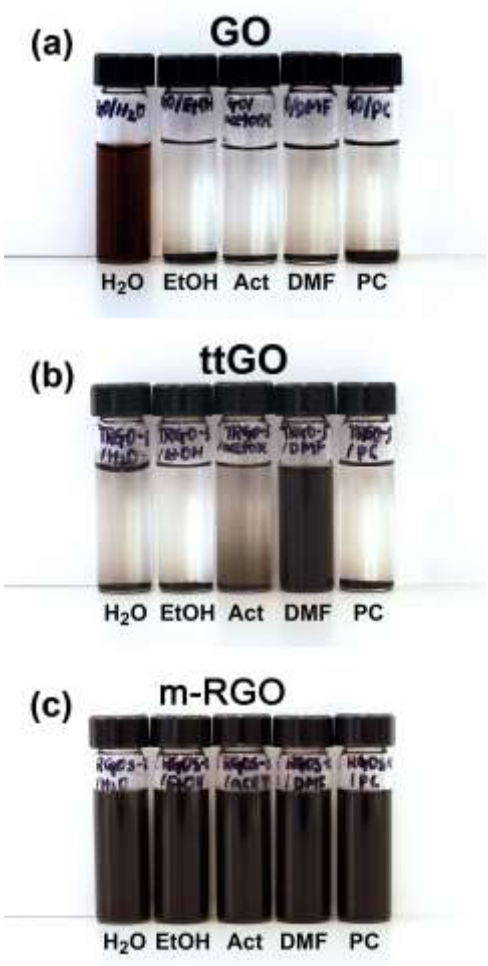

Figure 11. Photographs of (a) GO, (b) ttGO, and (c) m-RGO dispersions in water (H_2O), ethanol (EtOH), acetone (Act), N,N-dimethylformamide (DMF) and propylene carbonate (PC) from left to right.

In contrast to GO and ttGO, all the m-RGO dispersions showed no appreciable amount of precipitates even after the three-month period. This observation is rather remarkable in contrast to most of GO, reduced graphene oxide (RGO) and their derivatives which show rather exclusive dispersibilities in either water or organic solvents.[28b, c, 114] As described below, m-RGO is more reduced than GO and more importantly, it exhibits a significant amount of thiol groups in addition to hydroxyl groups on the graphene sheets. The reduced nature of the carbon atoms and the presence of the thiol groups must increase the hydrophobicity of the material and promotes a good dispersibility in organic solvents. In comparison to hydroxyl groups, however, we speculate that the relatively acidic nature of thiol groups results in deprotonation of thiols to some extent to give thiolate ions on the graphene sheets, so that it allows m-RGO to disperse well even in water.

Powder X-ray diffraction (PXRD) patterns of the prepared ttGO and m-RGO are compared with those of graphite flake precursor and GO in **Figure 12**. In **Figure 12(b)**, the (001) Bragg peak of the oven-dried GO is located at 11.9° (*d*-spacing = 7.44 Å),[104b] which confirms that we have obtained a well-oxidized graphite in which a significant amount of water molecules are present in the intersheet gallery. Although not show here, our GO samples dried by using rotary evaporation and freeze drying methods exhibit the (001) peak at 9.6 and 10.2°, respectively, which is also in good agreement with reported literature previously.[37, 115] The (001) Bragg peak position of GO appears typically near 10° but its precise location varies with the degree of oxidation[104, 115] and humidity.[15, 16b, 17]

In **Figure 12(d)**, the (002) peak of m-RGO has a much larger Full Width at Half Maximum (FWHM) and a lower intensity than that of ttGO (**Figure 12(c)**), suggesting that m-RGO has poorly stacked graphene sheets, as expected from the observed high dispersibility of m-RGO (**Figure 11**). Compared to GO, the (002)

peak of m-RGO shows a significant shift to 24.4° (*d*-spacing = 3.64 Å). Indeed, the (002) peak position and its FWHM of m-RGO are comparable to those of highly reduced GOs (RGOs) reported in the literature,[37, 107b] and hence the sulfurization reaction does not appear to noticeably affect the intersheet distances for m-RGO in comparison to RGO.

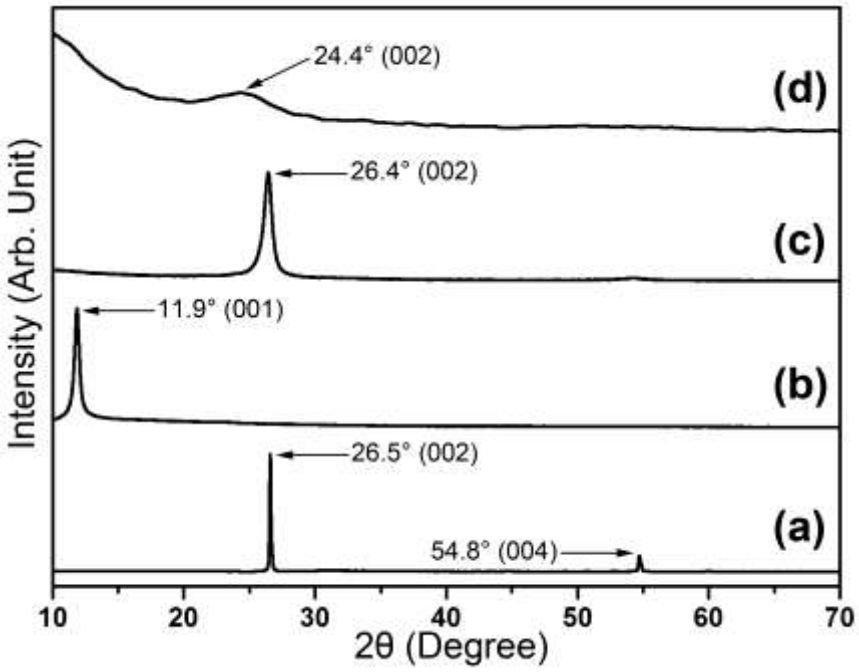

Figure 12. Powder XRD patterns of (a) graphite, (b) GO, (c) ttGO, and (d) m-RGO.

Meanwhile, the sharp (002) peak of ttGO at 26.4° (**Figure 12(c)**), which is comparable to the (002) peak of graphite flake at 26.5° (**Figure 12(a))**, indicates significant dehydration and restacking of graphene oxide sheets into a graphite-like structure. This feature is reflected in the Raman spectrum of ttGO where both D and G bands have smaller FWHMs than those for GO and m-RGO (**Figure 13**). The G bands appear around 1600 cm^{-1}, while the D bands are visible around 1340 cm^{-1} for all the samples except the graphite flake. Graphite flake exhibits a 2D band at 2712 cm^{-1}.[116] The positions of the G band for GO, ttGO, and m-RGO are higher in

frequency than that for graphite flake, which has been attributed to significant defects on graphene sheet.[66, 116a, 117] The Full Widths at Half Maximum (FWHMs) of the G band of GO, ttGO, and m-RGO are much larger than that of graphite flake, which is due to a higher degree of atomic disorder.[116b, 118] The I_D/I_G ratio of m-RGO (1.11) is almost the same as that of GO (1.08).The Raman spectrum of m-RGO is not changed significantly from the GO precursor in terms of the peak positions, FWHM and intensity ratios of the D and G bands, which is similar to what have been observed in comparative studies of RGOs and their original GO precursors.[100]

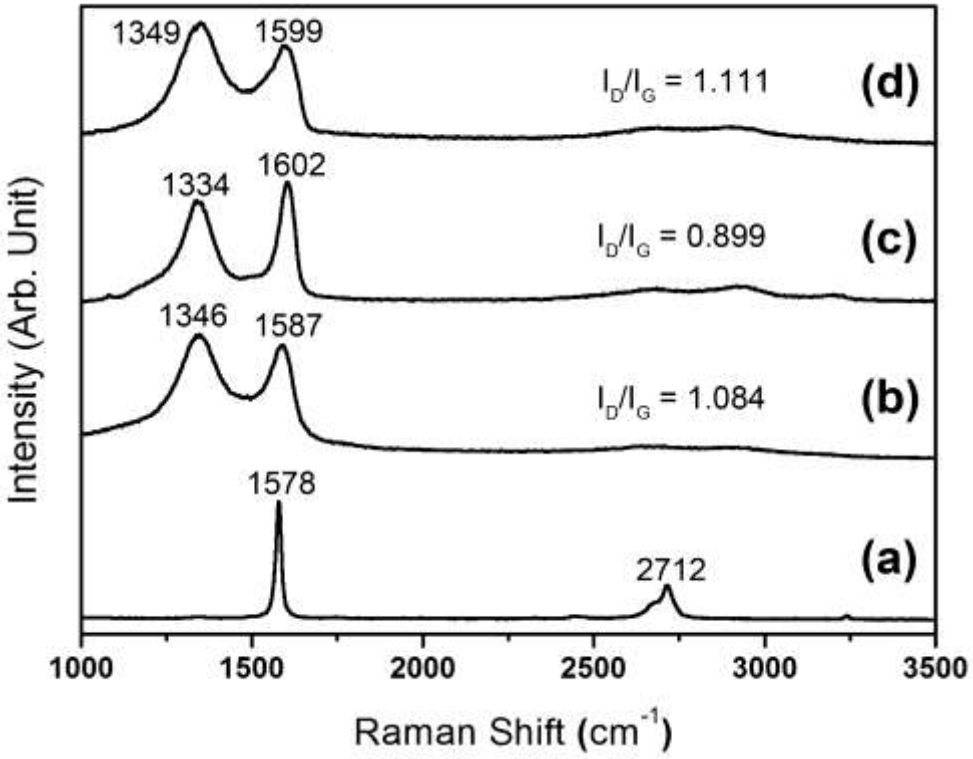

Figure 13. Raman spectra of (a) graphite flake, (b) GO, (c) ttGO, and (d) m-RGO.

Figure 14 shows TEM images of m-RGO (Sample 3 in **Table 1**) on a lacey carbon TEM grid. Generally, the material is in the form of sheets with a rag-like structure, which is consistent with the morphology expected for corrugated sheets with a high aspect ratio.[119] Indeed, the general morphology of the m-RGO is similar

to that of GO (not shown here) and it indicates that the sulfidation at 500 °C doesn't significantly affect to the structure of GO. Thick fringes are observed around the edges of the sheet in **Figure 14(b)**, which could indicate that there are only a few layers of the m-RGO sheet.[7c, 119c] Such fringes have been observed even for monolayer graphene sheets when they have scrolls and multiple folds.[120]

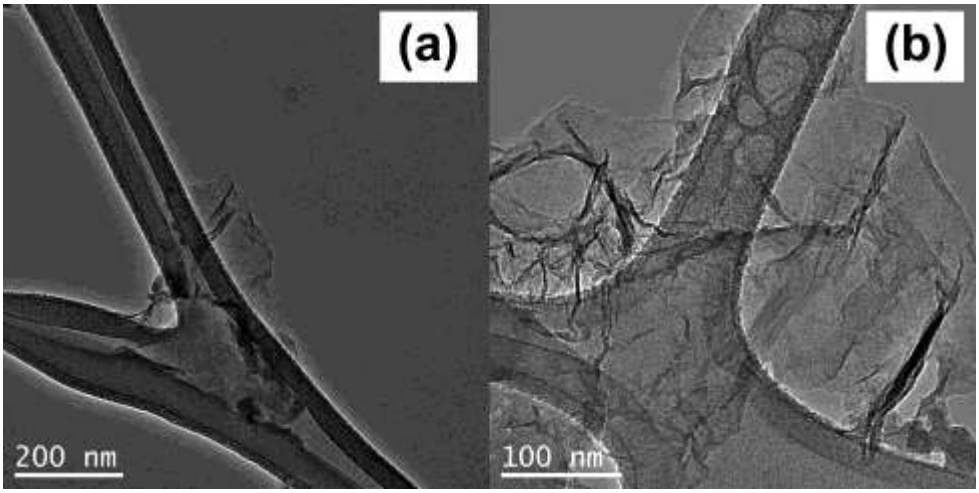

Figure 14. TEM images of m-RGO. The scale bars are 200 nm in (a) and 100 nm in (b).

The high-resolution XPS spectra of GO and m-RGO are shown in **Figures 15** and **16**, respectively, for selected energy regions. Their corresponding XPS survey scans are shown in **Figures 17(a)** and **17(b)**. The atomic ratios of C:O:S in GO calculated from its XPS survey scan shown in **Figure 17(a)** are 2.0:1:0.07 where the C:O is found to be in a typical range for well oxidized GOs.[39b, 118] The deconvolution of the high-resolution C1s and O1s spectra depicted in **Figures 15(a)** and **15(b)** indicates that only 7.1 % of the carbon atoms in GO exist as a sp^2-carbon, and the oxygen atoms are present in the form of hydroxyl (56%), carbonyl (23%), or ether (21%) functional groups. The small amount of the sulfur in GO is present as a sulfonate, as surmised from the S2p peak position in **Figure 15(c)**.

This is consistent with previous reports in which the GO from the Hummers method is shown to contain an insignificant amount of sulfonates.[121]

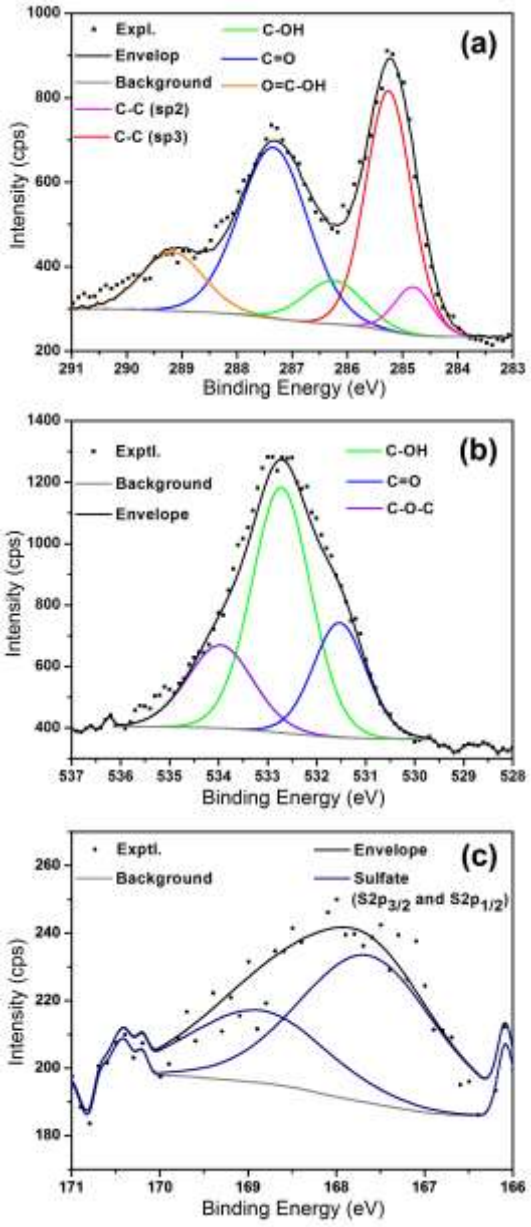

Figure 15. High-resolution XPS spectra of the core level region of (a) carbon 1s, (b) oxygen 1s, and (c) sulfur 2p for GO, respectively (colored).

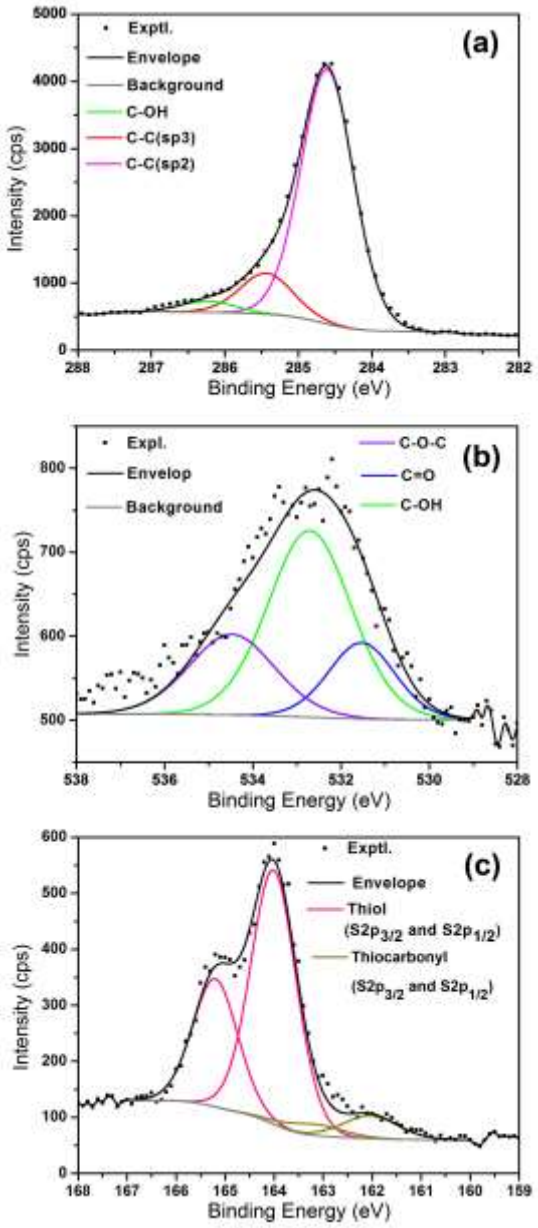

Figure 16. High-resolution XPS spectra of the core level region of (a) carbon 1s, (b) oxygen 1s, and (c) sulfur 2p for m-RGO, respectively (colored).

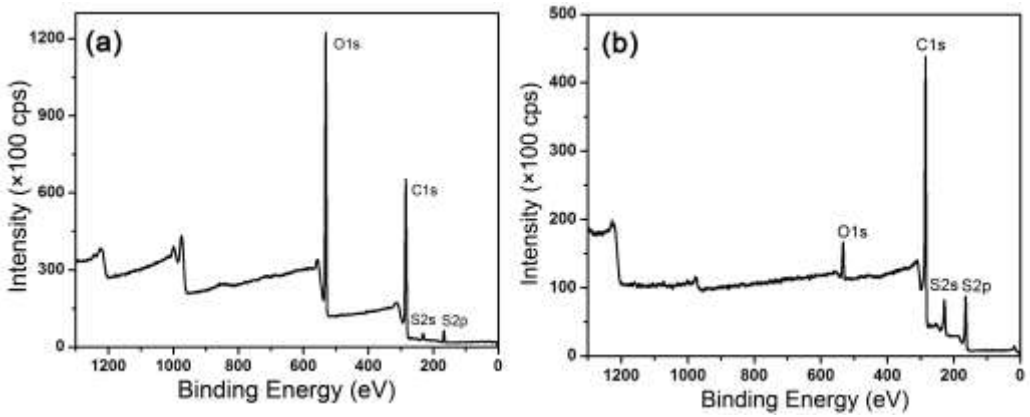

Figure 17. XPS survey scans of (a) air-dried GO and (b) m-RGO. See the main text for the details.

Meanwhile, the C:O:S ratios in m-RGO are estimated to be 17:1:2.2 from its XPS survey scan represented in **Figure 17(b)**, indicating that there exist more than twice as many sulfur atoms as oxygen atoms in the structure. These results are consistent with the average chemical composition of the m-RGO of C:O:S = 15:1:2 which was obtained using the energy dispersive X-ray spectroscopy (EDS) shown in **Figure 18**. The deconvolution results indicate that 83% of the carbon atoms exist as sp^2-carbon in m-RGO, in comparison to 7.1% in GO. Among the oxygen functional groups, the relative amount of the hydroxyl groups remained the same (56%) in m-RGO while the carbonyl content somewhat decreased to 18% and the ether content increased to 25%. More significantly, the sulfur atoms in m-RGO are present predominantly in the form of thiol (89%) in addition to thiocarbonyl (11%). The presence of the thiol groups is also evidenced from the ATR FT-IR spectrum of m-RGO dispersion in ethanol shown from 550 to 750 cm^{-1} shown in **Figure 19**. In comparison to ethanol and a GO ethanol dispersion, the m-RGO dispersion shows two additional absorption peaks centered at 617 and 719 cm^{-1} which can be attributed to C–S stretching modes observed in thiols.[122] The C–S stretching vibration is known to have a low intensity.[123] Further characterization of the m-RGO

products using NMR techniques were attempted but unsuccessful due to the high electrical conductivity of the m-RGO that hampered the use of magic angle spinning.

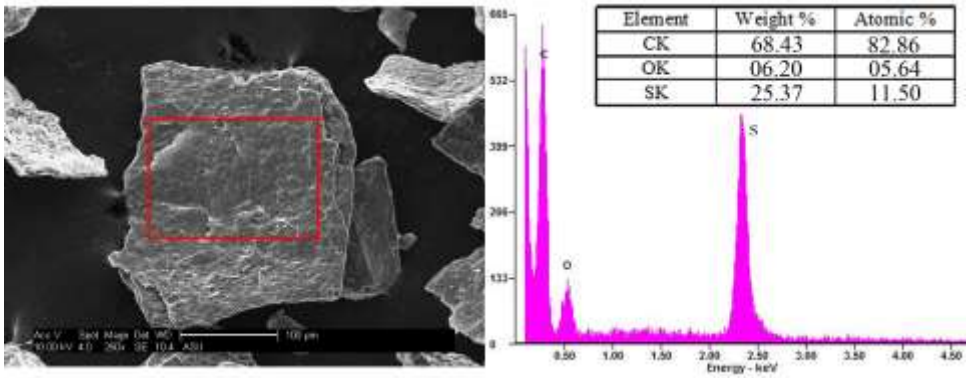

Figure 18. Representative SEM image and EDS spectrum of air-dried m-RGO. See the main text for the details.

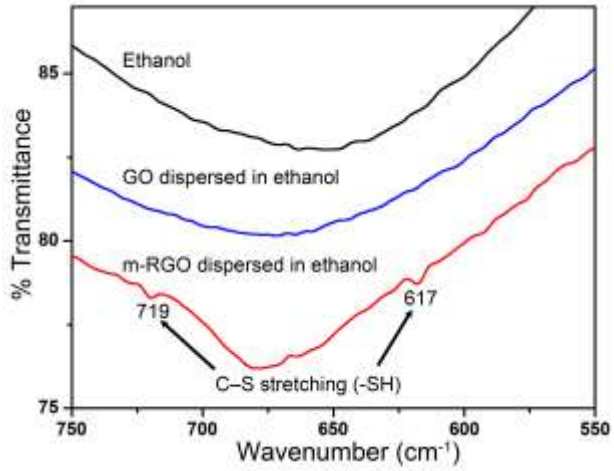

Figure 19. ATR FT-IR spectra for ethanol (black line) and GO solution dispersed in ethanol (blue line) and m-RGS dispersed in ethanol (red line).

Ellman assay method[124] was employed in order to quantify the amount of reactive thiols on m-RGO. The UV-Vis absorption spectra of five standard solutions and one sample solution are shown in **Figure 20** and the standard curve in **Figure 21**, respectively. The estimated thiol content in m-RGO was 28 wt%, taking into account only nonhydrogen elements, which is comparable to 24 wt% estimated from the XPS data. In other words, most of the sulfur atoms in m-RGO are in the form of thiols that are chemically reactive to form disulfides. Based on these spectroscopic and chemical studies, **Figure 22** shows a schematic diagram of a chemical structure of m-RGO. Analogous to the structures of GO,[39b] it is speculated that thiocarbonyl and carbonyl functional groups decorate the edge of the graphene matrix, while hydroxyl and thiol groups are placed on both the basal planes and the edges of the graphene sheets.

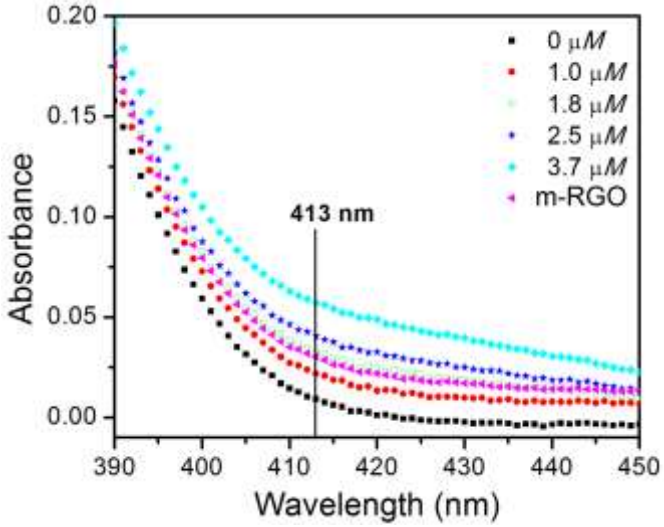

Figure 20. UV-Vis spectra of L-cysteine standard solutions with various concentrations and a mixture of m-RGO and DTNB in aqueous Tris-HCl buffer at pH 8 in the Ellman assay experiment.[124]

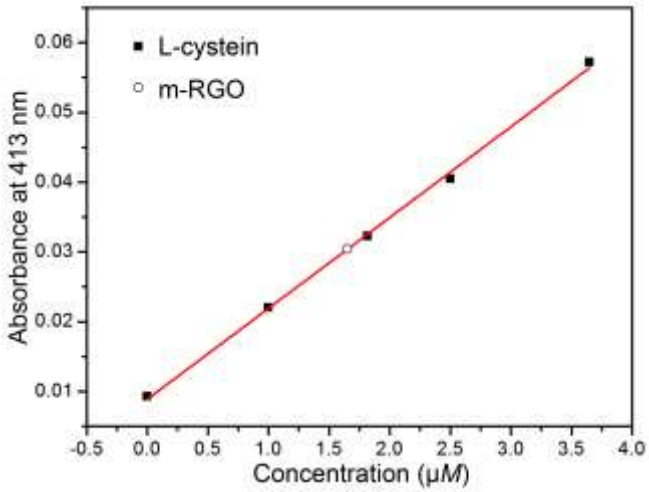

Figure 21. Plot of optical absorbance at 413 nm versus thiol concentration obtained from **Figure 20**. Black dots and white dot represent the standard solutions and a sample solution, respectively. The straight line (red) is a linear least square fit of the experimental data (*Rp* = 0.998).

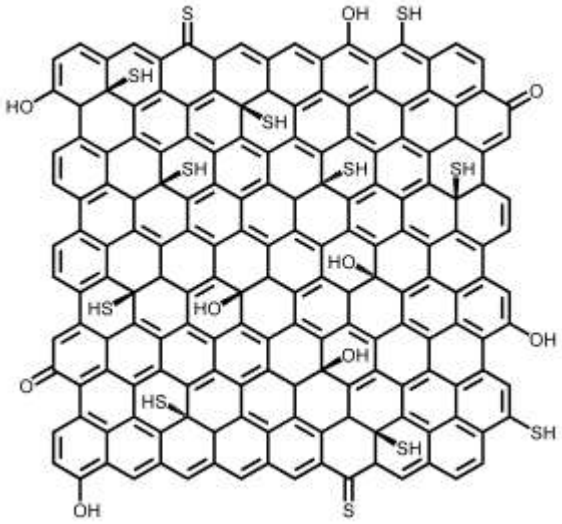

Figure 22. Schematic diagram of mercapto reduced graphene oxide (m-RGO).

The high sulfur content in the m-RGO produced at 500 °C potentially indicates a good thermal stability of the sulfur functional groups on the graphene sheets, and thus the thermal behavior of m-RGO was further studied by employing TGA. **Figure**

23 shows the TGA results of m-RGO, ttGO, and GO carried out under Ar flow up to 600 °C. Excluding the weight loss below 100 °C due to evaporation of free water, GO shows a total weight loss of 53 wt%, which is consistent with the literature.[112a] In contrast, the TGA curve of m-RGO shows a weight loss of only 15 wt%. Both GO and m-RGO show the largest weight loss in the relatively low temperature region from 100 to about 290 °C (45 and 5 wt% for GO and m-RGO, respectively). The rather rapid weight loss has been assigned to the removal of labile oxygen functional groups of GO and RGO in the previous report.[125] As temperature increases up to 600 °C, both GO and m-RGO lost their weight more or less at the same rate.

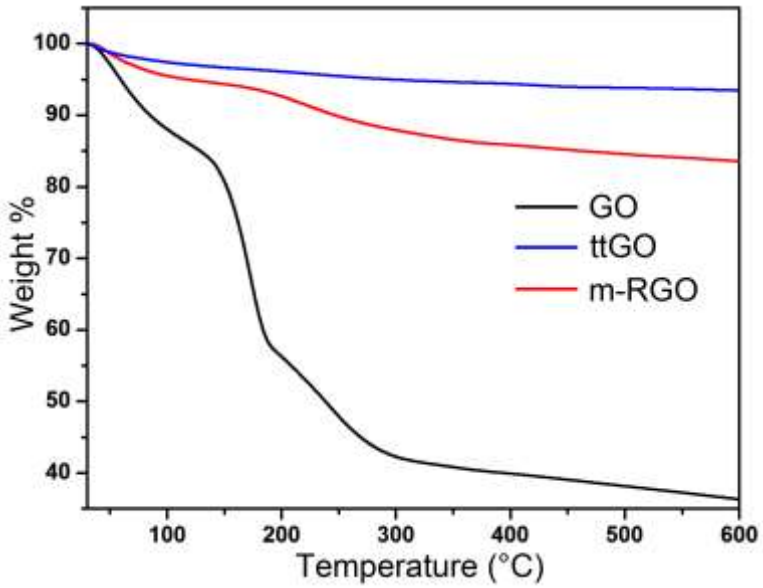

Figure 23. TGA curves of dried GO (black line), ttGO (blue line), and m-RGO (red line).

Meanwhile, ttGO gradually but only marginally lose its weight in the entire heating period. The XPS studies on the m-RGO after the heat treatment (see **Figure 24**) indicate that the heat treatment further reduced the m-RGO into a composition of C:O:S = 19:1:3.4 in comparison to the original composition (C:O:S = 17:1:2.2).

Notably, however, the relative amounts of sulfur to carbon and oxygen increased by 42% and 55%, respectively. These observations signify that the thiol functional groups are not as labile as the oxygen functional groups even up to 600 °C.

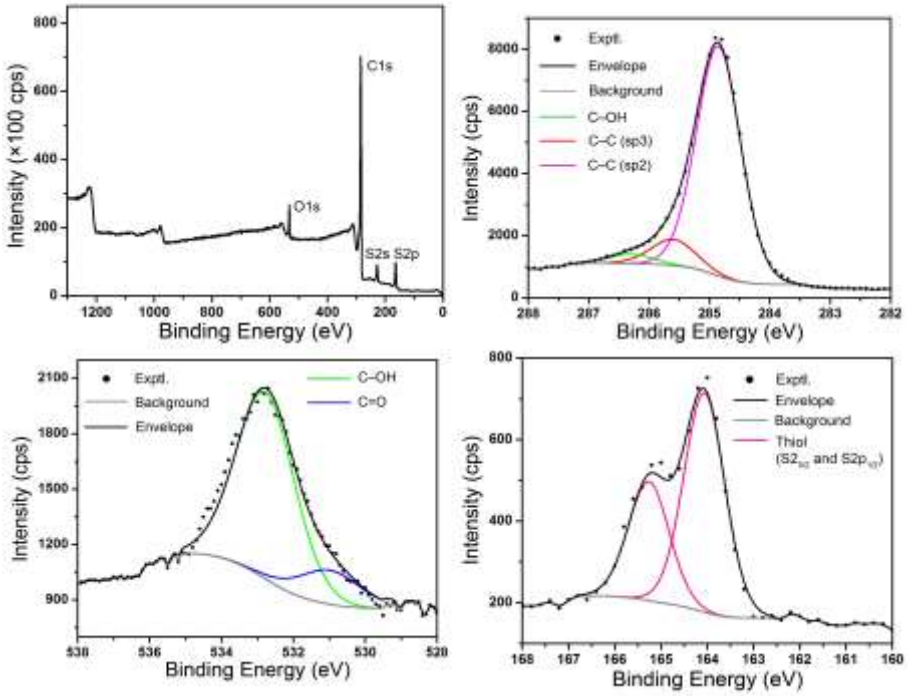

Figure 24. XPS survey scan (top-left) and high-resolution XPS spectra of core level region of C1s (top-right), O1s (bottom-left), and S2p (bottom-right) of m-RGO after heat treatment at 600 °C.

The band-to-band optical gaps for GO and m-RGO were estimated to be approximate electronic band gaps, by applying Tauc's Equation (**Equation 4**) on their UV-Vis absorption spectra within a parabolic band approximation for amorphous carbon:[126]

$$\alpha h\nu = B(h\nu - E_{Tauc})^2 \qquad \textbf{Equation 4}$$

where α is the absorption coefficient, B is the optical constant, h is Planck's constant, ν is the frequency, and E_{Tauc} is the Tauc gap. In this work, the Tauc's equation is

transformed into an equivalent form, $(A/\lambda)^{1/2} = \kappa(h\nu - E_{Tauc})$, which relates the measured absorbance, A, directly to the absorbed light frequency through the Beer-Lambert law, $A = \alpha bC$, where b is the light path length of the analyte, and C is the concentration of the analyte. κ is a proportional constant theoretically expressed as $\kappa = (BbC/hc)^{1/2}$, where *c* is the velocity of light, but serves only as an empirical parameter here due to the simplistic nature of the Tauc model. **Figure 25** shows Tauc plots of $(A/\lambda)^{1/2}$ versus $h\nu$ for GO and m-RGO dispersions obtained from their UV-Vis absorption spectra shown in **Figure 26**. By extrapolating the linear region of the curves to the energy axis, the Tauc gaps of GO and m-RGO are estimated to be 3.3 and 0.03 eV, respectively (**Figure 25**). The much smaller band gap estimated for m-RGO than for GO is consistent with the more reduced nature of the sp^2-carbon atoms in the former. However, the significant orbital overlap between sulfur 3s and 3p orbitals with the π-orbitals in the graphene sheet may be another possible cause for the band gap decrease.

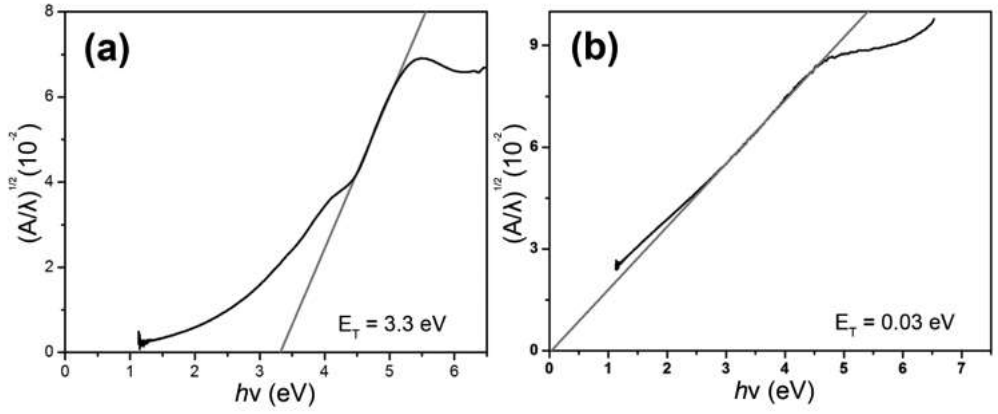

Figure 25. Tauc plots of $(A/\lambda)^{1/2}$ versus $h\nu$ for (a) GO and (b) m-RGO.

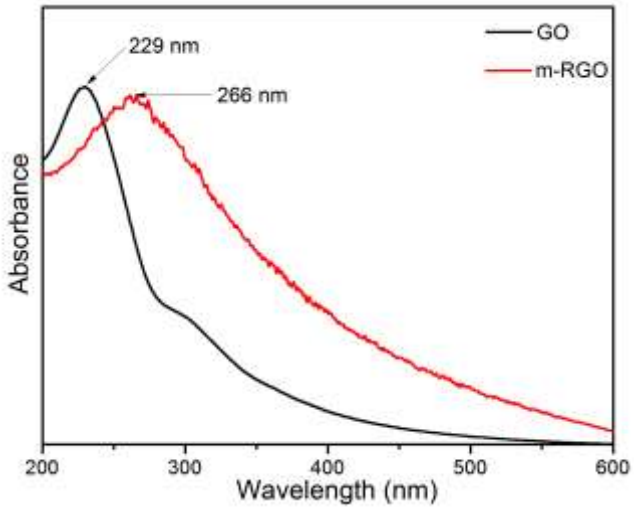

Figure 26. UV-Vis absorption spectra of GO (black) and m-RGO dispersions (red). The red-shit of the peak maximum is consistent with the reduced nature of the graphene sheets.[127, 37]

3.4 Concluding Remarks

It has been successfully demonstrated that simultaneous reduction and direct sulfidation of graphene oxide is possible through a relatively high-temperature solid/gas metathetical synthetic route by employing boron sulfides for the metathesis. The resulting material, mercapto reduced graphene oxide (m-RGO), has a sulfur content about twice as much as the oxygen amount and most of the sulfur is present in the form of thiol functional groups. Ellman assay on m-RGO has established that practically all the thiol groups in m-RGO act as free thiols which can participate in disulfide formation. The thiol groups on the graphene sheets were found to be more thermally stable than the hydroxyl groups from TGA results.

It is envisaged that the large amount of thiol groups directly bonded to graphene sheets in m-RGO may lead to advent of various new functionalization routes for graphene sheets through cross-linking the thiols to small molecules,

biological molecules or polymers based on disulfide formation or thiol-ene (yne) click chemistry.[128] Having both sulfur and oxygen functional groups, the multifunctional nature of the material may provide unique opportunities in their applications. In addition, the high affinity of m-RGO to noble metals may allow the material to be applied as a noble metal scavenger, as a conductive coating material on noble metal substrates,[129] or as a passivating/stabilizing agent for noble metal nanoparticles for their biological applications.[130] It is further noted that the newly developed thionation method may be applicable for other carbon nanomaterials that have surface oxygen functional groups, potentially extending the current scope of their functionalization schemes.

CHAPTER 4

THIONATED REDUCED GRAPHENE OXIDE THROUGH ONE-POT SOLVOTHERMAL REACTION WITH BERZELIUS REAGENT, P_4S_{10}

4.1 Introduction

Since graphene was successfully isolated in 2004,[5] it has been emerged as a fascinating material for many potential applications[131] due to its extraordinary electronic properties.[132] However, it was always been a challenging task for the past few years to have a bulk production of chemically synthesized graphene for its utilization in many potential areas. Chemical modification or functionalization of the surface has been used as an easy pathway to tune various physical as well as chemical properties of carbon nano-materials over the years.[28b, 97e, 133] In this regard, chemical modification of graphene has found out as a promising strategy to produce large quantities of graphene for different potential application purposes. The oxygen functionalized graphene is an electrically insulating material that is not desirable for many applications. To dates, much research has been paid attention to manipulate both the physical and chemical properties of graphene through chemical modification or reduction of oxygen functionalized graphene namely graphene oxide (GO).[97c, 134]

Till dates, only oxygen functional groups on chemically modified graphene generated during GO synthesis have been utilized for different limited purposes. Mainly, carboxyl and hydroxyl groups on graphene have been played a role of linking unit.[97a, 135] The utilization of chemically modified graphene with multifunctional groups, however, could open up new directions of potential researches. Among diverse functional groups, thiol functional group is favorable for various purposes such as cross-linking group through disulfide formation,[136] click chemistry in various reaction media,[128] self-assembly monolayers (SAMs) on gold surface,[137] heavy metal

scavenger,[138] biosensors,[139] biomedical applications,[140] and passivation and stabilization of noble metal nanoparticles for biological applications.[130]

Various thionating agents such as potassium thioacetate,[141] ethyl xanthogenate,[142] sodium dimethyldithiocarbamate,[143] and alkali hydrosulfide,[144] have been used for the thionation of halogen groups by an SH group. More recently, thiourea was employed to produce thiol functionalized nanodiamond.[145] This procedure, however, requires substitution of hydroxyl functional group by bromide and multiple steps. These all thionating agents cannot directly convert oxygen functional groups into corresponding sulfur functional groups.

In contrast to all thionating agents aforementioned, almost all kinds of oxygen functionalities can be easily converted to corresponding sulfur functional groups by reacting those groups with P_4S_{10}.[80] Therefore, phosphorus decasulfide (P_4S_{10}) is one of the familiar thionating reagents, widely used for sulfidation in organic chemistry. P_4S_{10} was used for thionation of diethyl ether, ethanol,[81] and amiades.[146] Moreover, P_4S_{10} has been employed for the synthesis of heterocyclic compounds containing sulfur by simply replacing oxygen.[80] The use of P_4S_{10} in organic chemistry, however, was restricted due to poor yield and selectivity in the final product, which is an important issue in that area. Although P_4S_{10} is not the most desirable and useful thionating agent in terms of yield and selectivity in organic chemistry, it is still good enough using P_4S_{10} to synthesize thiol-functionalized reduced graphene oxides (namely "mercapto reduced graphene oxides" (m-RGOs)) starting from graphite oxide prepared by modified Hummers method.[34]

In 2005, P_4S_{10} was used for thionation of oxidized multi-walled carbon nanotubes (O-MWCNTs) through reflux condition in toluene. However, it requires long reaction time (7 days) and the sulfur content after the reaction was less than 2 wt%.[147] More recently, m-RGO was also synthesized in my previous study (in

Chapter 3) through high temperature route (solid-gas metathetical reaction) by utilizing gaseous form of boron sulfide (B_xS_y) molecules. But those graphene sheets were re-stacked together in some extent during the course of reaction and it was difficult to completely utilize the product for different purposes. In order to solve aforementioned problems, the development of efficient and facile synthetic route is required. Therefore, in this study, a relatively low temperature solvothermal reaction route is developed to produce the m-RGOs from exfoliated graphite oxide by varying reaction conditions such as reaction temperatures and the amount of P_4S_{10}.

Although there has not been a clear report of thionation mechanism of P_4S_{10}, the following two plausible reaction mechanisms have been generally accepted: 1) P_4S_{10} could dissociate into P_2S_5 that eventually reacts with various oxygen functional groups and 2) P_4S_{10} could dissociate into P_2S_5 which then reacts with pyridine (solvent) to form zwitterionic compounds and the zwitterionic compound subsequently reacts with various oxygen functional groups.[148] To best my knowledge, thionation of graphite oxide with utilizing Berzelius reagent (P_4S_{10}) is for the first time successfully achieved. Herein, a facile and efficient solvothermal reaction route is reported to produce m-RGO with 14.5~19.4 wt% sulfur content depending upon the reaction temperature. For comparison, reduced graphite oxide (RGO) was synthesized through the same reaction condition as that of as-synthesized m-RGO without P_4S_{10}.

4.2 Experimental Section

4.2.1 Synthesis of Graphene Oxides (GOs)

GOs were prepared by using a modified Hummers method through oxidation of natural graphite flake with strong oxidants.[34] In a typical procedure, 1 g of natural graphite flake (Sigma-Aldrich) was ground with 5 g of NaCl (Alfa Aesar,

99+%) until the mixture becomes homogeneous by visual inspection. NaCl from the mixture was then washed away using deionized water with vacuum filtration. The ground graphite on the filter paper was dried at 110 °C in a lab oven for 2 hours. 0.765 g of $NaNO_3$ (Sigma-Aldrich, ≥ 99.0%) was first dissolved in 40 mL of concentrated H_2SO_4 (Sigma-Aldrich, ACS reagent, 95 ~ 98%) in a 400 mL of beaker with stirring for 20 minutes. About 1 g of the ground graphite was then added to the beaker. Subsequently, the beaker was placed in an ice bath and then 5 g of $KMnO_4$ (Sigma-Aldrich, ≥ 99.0%) was slowly added to the beaker while the temperature was kept below 10 °C. Afterward, the beaker was removed from ice bath. The mixture in the beaker was then heated at 35 ~ 40 °C with vigorously stirring until it became pink thick paste. 100 mL of deionized water was added to the beaker and 20 mL of H_2O_2 (Alfa Aesar, ACS reagent, 29 ~ 32%) was slow added to the suspension to finish the reaction. After the reaction, the color of the suspension became bright yellow. The suspension was then repeatedly centrifuged and washed with diluted HCl until $BaCl_2$ (Anhydrous purified, J.T. Baker chemical Co.) test shows a negative result.

4.2.2 Synthesis of Mercapto Reduced Graphene Oxides (m-RGOs)

The purified GOs in water were mixed with 1 *M* NaOH solution to obtain precipitated GOs and subsequently the pH was adjusted around 9 by rinsing with deionized water. The solvent exchange of the GOs sludge was performed with 100 mL of pyridine by vacuum filtration. The washed GOs sludge with pyridine was homogenized for 10 minutes to obtain exfoliated GOs in pyridine for further sulfidation reaction. For the synthesis of m-RGOs *via* solvothermal reaction route, phosphorus decasulfide (P_4S_{10}, Sigma-Aldrich, 99%) has been used as a thionating reagent. To get control over the amount of sulfur incorporation in graphitic network,

the amount of the phosphorus decasulfide (P_4S_{10}, sulfur precursor) as well as the reaction temperature were varied. Hereafter, all m-RGOs samples, unless otherwise stated, were synthesized by using 10% excess with respect to stoichiometric amount of P_4S_{10}. In a typical solvothermal reaction, 220 mg of P_4S_{10} (10% excess with respect to stoichiometric amount of P_4S_{10}) was added to 200 mg of GO in 13 mL of pyridine in a Teflon-lined autoclave of capacity of 23 mL. It was then placed in an oven preset at 120, 150 and 180 °C for 15 hours. The solid product was collected *via* vacuum filtration and it was washed several times with deionized water and ethanol to remove all the unreacted starting materials and by-products. The mercapto reduced graphene oxides (m-RGOs) in water were freeze-dried for further characterization. This final product can be easily dispersed in various solvents like H_2O, DMF, DMSO, NMP, etc. by sonication for 30 minutes to achieve the stable dispersion of mostly single or bi-layer m-RGO in wide range of solvent media.

4.2.3 Materials Characterization

Powder X-ray diffraction patterns (PXRD) were recorded using a Bruker D8 diffractometer with Cu-Kα radiation. Thermogravimetric analysis (TGA) studies were performed using a Mettler-Toledo TGA/DSC 1 STARe system. Samples were analyzed by heating from 25 to 600 °C at 5 °C·min^{-1}. All analyses were carried out under an Ar flow at 60 mL·min^{-1} with 70 µL-capacity alumina crucibles.

X-ray photoelectron spectroscopic (XPS) measurements were carried out using a VG-220IXL spectrometer with a monochromated Al Kα radiation (1486.6 eV, line width 0.8 eV). The pressure in the analyzing chamber was kept at the level of 10^{-9} torr while recording the spectra. The spectrometer has the energy resolution of 0.4 eV. All the binding energies were corrected with reference to C(1s) at 284.6 eV. Deconvolution of the spectrum was done using the CASA software with the accuracy

of 0.2 eV. Shirley background was used for the deconvolution. For the high-resolution C1s XPS spectrum was deconvoluted into the following three components: C–C (sp^2- and sp^3-hybridized peaks at 284.7 and 285.4 eV, respectively),[37] C–S (285.3 eV),[105] and C–O (hydroxyl or ether peaks at 286.5 eV).[104] Carbon atoms with the C–S bond were not separately treated because the C1s binding energy of C–S (285.3 eV)[105] is too close to that of C–C (sp^3-hybridization) and thus could not be resolved, given the resolution of the XPS instrument (0.4 eV). The high-resolution O1s XPS spectrum was presented with the following oxygen functional groups: P–O, C═O (531.7 eV),[106, 149] and/or oxygen binding energy in sulfonic functional group (531.2~532 eV),[150] as well as C-OH (532.7 eV).[106] The high-resolution S2p XPS spectrum was deconvoluted with three functional groups: C═S ($S2p_{3/2}$ at 162.0 eV with FWHM of 1.4 eV; $S2p_{1/2}$ at 163.2 eV with FWHM of 1.4 eV),[109] C–SH ($S2p_{3/2}$ at 164.0 eV with FWHM of 1.2 eV; $S2p_{1/2}$ at 165.2 eV with FWHM of 1.2 eV),[108] and C-SO_3H ($S2p_{3/2}$ at 167.5 eV with FWHM of 1.4 eV; $S2p_{1/2}$ at 168.7 eV with FWHM of 1.4 eV).[150b, 151] The area ratio and splitting energy difference between $S2p_{3/2}$ and $S2p_{1/2}$ spin-orbit doublet peaks were 2:1 and 1.2 eV, respectively.

A Nicolet 6700 FTIR spectrometer (Thermo Scientific Nicolet) was used to collect attenuated total reflectance (ATR) FTIR spectra of ethanol and supernatant solutions of m-RGO dispersed in ethanol. Drops of each sample solutions were placed on a diamond plate for the measurements. All spectra were calibrated against an air spectrum. Drops of each sample were placed in contact with attenuated total reflectance (ATR) on a multibounce plate of diamond. All spectra were rationed against a background of an air spectrum. Scanning transmission electron microscopy (STEM) images and elemental mapping images were acquired using JEOL 2010F (200 kV) TEM/STEM equipped with Schottky type field emission gun and EDAX thin window X-ray energy dispersive spectrometer (EDS) detector.

For the STEM-EDS composition analysis, 8 different areas were examined and averaged out. STEM samples were prepared by dipping a copper grid covered with a holey carbon film into the dispersion, taken out and dried in air.

UV-Vis measurements were carried out using a Hewlett-Packard 8453 spectrophotometer using quartz cuvettes with a 1 cm path length. Surface topography images were obtained using atomic force microscope (Pico-Plus AFM, Molecular imaging, Agilent technologies). All AFM studies were performed in air using a tapping mode with SCANASYST-AIR tips (Bruker). The mercapto reduced graphene oxide (m-RGO) suspension in 200-proof ethanol obtained after ultrasonication for 30 minutes and subsequently centrifuged at 6000 rpm for 10 minutes was used for deposition of m-RGO sheets on freshly cleaved mica by using drop-casting method. The images were collected at a scan rate of 1.0 Hz in air.

The Raman spectra were collected using a custom-built Raman spectrometer in 180° geometry. The sample was excited using a 0.75 mW Compass 532 nm laser. The laser power was controlled using neutral density filters. The laser was focused onto the sample using a 50X superlong working-distance Mitutoyo objective with a numerical aperture of 0.42. The signal was discriminated from the laser excitation using a Kaiser laser band pass filter followed by a Semrock edge filter. The data were collected using an Acton 300i spectrograph and a back thinned Princeton Instruments liquid nitrogen cooled CCD detector.

4.3 Results and Discussions

Figure 27 shows the dispersions of RGOs and m-RGOs in deionized water (left), ethanol (middle), and N,N-dimethylformamide (DMF) (right). The dispersions were prepared by ultrasonication for 40 minutes (**Figure 27(a)** and **(c)**) and centrifugation at 4000 rpm for 10 minutes after sonication (**Figure 27(b)** and **(d)**),

respectively. Both RGOs and m-RGOs show a good dispersion in all solvents right after sonication but after centrifugation, almost all RGOs precipitated out in all solvents. In contrast to RGOs, m-RGOs still shows a good dispersion in both ethanol and DMF after centrifugation. Although all RGOs in water were precipitated out, the m-RGOs still demonstrates relatively good dispersion in water after centrifugation. The dispersibility of m-RGOs in both water and organic solvents is rather remarkable in contrast to most of GOs, RGOs and their derivatives that show rather exclusive dispersibilities in either water or organic solvents.[28b, c, 114] The dispersibility between RGOs and m-RGOs is very different from each other, which indicates that thiol functional group on the surface can change the dispersibility of m-RGO significantly. Herein, It might be speculated that relatively more acidic thiol group than hydroxyl group can be deprotonated in some extent to form thiolate that can generate negative charge on the surface and it generates a good dispersion in water.

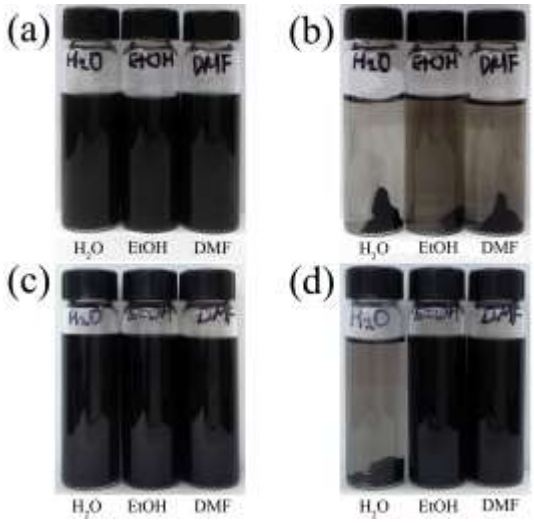

Figure 27. Photographs of (a) and (b) RGOs and (c) and (d) m-RGOs dispersion in water, ethanol (EtOH), and dimethylformamide (DMF) right after sonication (a) and (c) and after centrifugation at 4000 rpm for 10 minutes (b) and (d).

The absorption coefficients of graphite dispersed in various organic solvents and in water/surfactant were reported previously.[28e, 152] The absorption coefficient was varied in different solvents as well as materials.[28e, 153] Therefore, the absorption coefficient of m-RGOs can be different from that of graphite. In order to find the absorption coefficient of m-RGOs dispersed in DMF and ethanol, these dispersions were characterized by UV-Vis absorption spectroscopy and the absorption at 660 nm was collected with different concentration of m-RGOs in DMF and ethanol, which is showing Beer-Lambert behavior shown in **Figure 28**. The absorption coefficient at 660 nm of m-RGO in DMF and in ethanol is 4080 and 3070 L g^{-1} m^{-1}, respectively.

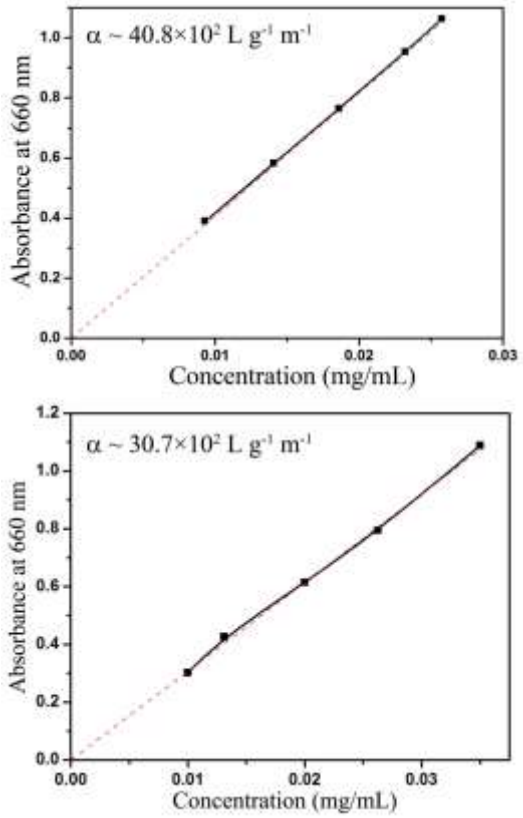

Figure 28. Absorbance at 660 nm with different concentration of m-RGOs dispersed in DMF (up) and in ethanol (bottom), respectively.

Additionally, UV-Vis spectra of GOs, RGOs, and m-RGOs are shown in **Figure 29**. The absorption peaks of GOs are shown around 229 nm as well as a shoulder around 305 nm which attributes to π→π* transition of aromatic C–C bond and n→π* transition of C═O.[31a] The absorption peak position of π→π* transition was red-shifted from 229 nm for GOs to 260 nm for RGOs and to 273 nm for m-RGOs due to extended aromatic C–C bond, suggesting that electronic conjugation within graphene sheet is restored.[31a, 114] It is important to note that the absorption peak of m-RGOs (273 nm) is further red-shifted than that of RGOs (260 nm), which indicates that the optical transition gap of m-RGOs was further decreased. The further decreased optical gap may be a significant orbital overlap of 3s and 3p orbitals with π-orbitals of aromatic C–C bond.

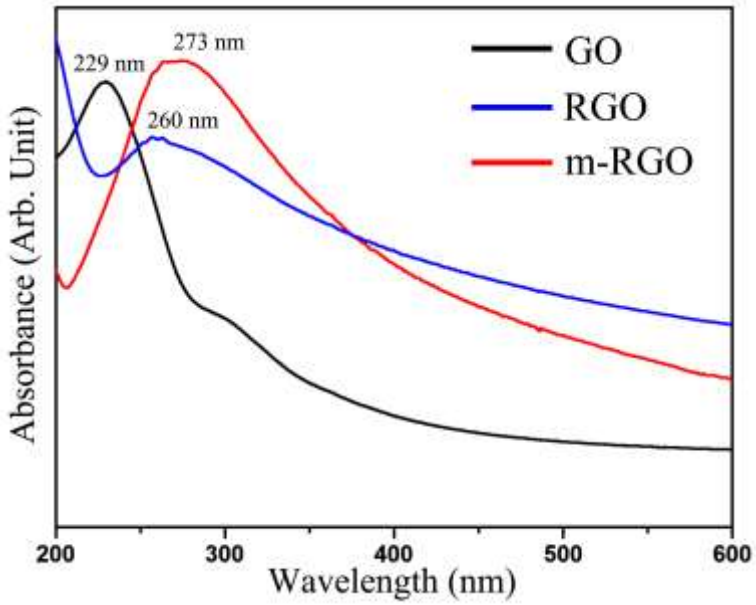

Figure 29. UV-Vis absorption spectra of GO (black), RGO (blue), and m-RGO (red) dispersions.

Powder X-ray diffraction (PXRD) patterns of bulk graphite powder, GO, RGO, and m-RGO are presented in **Figure 30**. (002) Bragg peak position in GO was

shifted to 2θ= 9.54° (d-spacing = 9.3 Å) with respect to bulk graphite powder which indicates increase in interlayer spacing due to heavy oxidation of graphite flakes as well as intercalation of water molecules between the layers.[37, 104b, 115] The (002) peak position (2θ= 24.7°, d-spacing = 0.36 Å) of RGO and m-RGO, however, shows a significant shit compared with that of GO, which is the indirect evidence of dehydration of the intercalated water between the layers. The (002) peak position in RGO and m-RGO is slightly lower than that (2θ= 26.5°, d-spacing = 0.34 Å) of bulk graphite, which may be due to the presence of oxygen and sulfur functional groups on the basal planes of the graphene layers. The large Full-Width at Half Maxim (FWHM) and less intense (002) peak in both RGO and m-RGO than that of graphite powder and GO reveal its less ordered structure along c-direction. The (002) peak position and large FWHM of RGO is comparable with those of highly reduced GO reported previously[37, 107b].

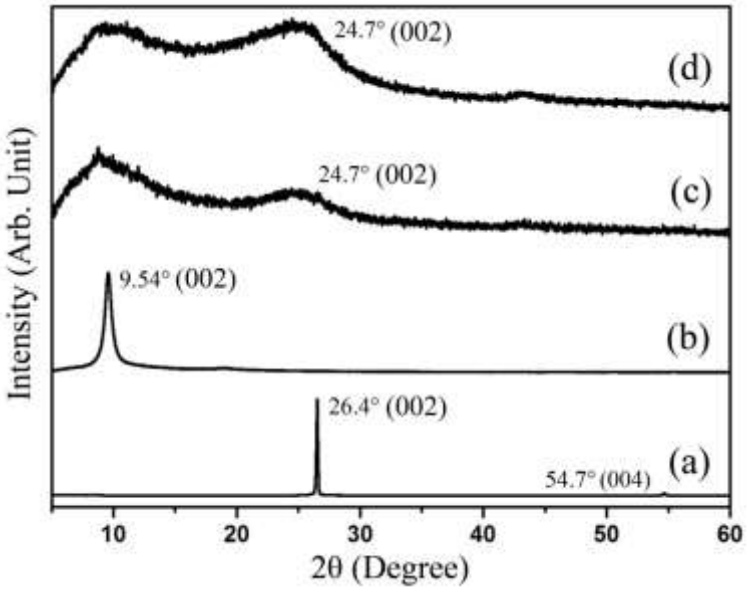

Figure 30. Typical powder XRD (PXRD) patterns of (a) bulk graphite powder, (b) GO, (c) RGO, and (d) m-RGO.

Raman spectra of graphite flake, GO, RGO, and m-RGO are shown in **Figure 31**. It is well known fact that graphite does not exhibit D band; it only shows the in-phase vibration of the graphite lattice (G band, 1583 cm^{-1}) corresponding to first-order scattering as well as less intense and broader second-order scattering (2D band, 2722 cm^{-1}). The G band peak position in GO, RGO, and m-RGO (~1590 cm^{-1}) is higher in frequency than that of graphite. There are various factors such as varying grain size, presence of isolated double bonds,[154] etc. that can influence the Raman spectra of graphitic materials, which have been debated so far.

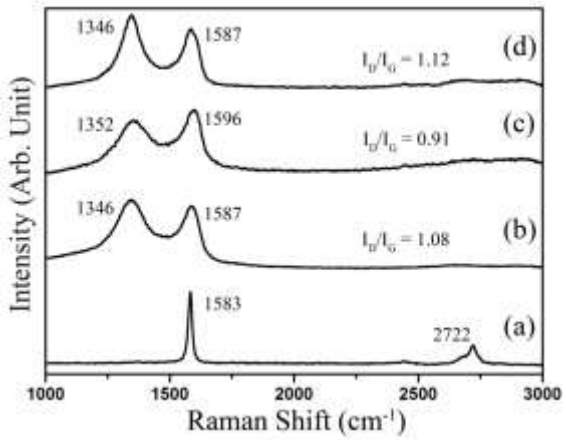

Figure 31. Raman spectra of (a) bulk graphite flake, (b) GO, (c) RGO, and (d) m-RGO.

The intensity ratio of D-band to G-band (I_D/I_G) in graphitic materials has been usually used as an indication of the degree of the structural defects present in the materials. According to Tuinstra-Koenig (TK) equation at a fixed λ,[66] the I_D/I_G ratio increases with increasing disorder. The I_D/I_G ratio of RGO was decreased after solvothermal reaction, which indicates that a degree of the structural defects was decreased during the reaction (restoration of sp^2-hybridized C atoms). The value of I_D/I_G ratio in GO and m-RGO, however, is 1.08 and 1.12 respectively, indicating presence of similar extent of structural disorder in these two materials. This may

indirectly suggest that oxygen functional groups in GO were replaced by sulfur functional groups during the solvothermal reaction.

The X-ray photoelectron spectra of RGO and m-RGO are depicted in **Figure 32** and **Figure 33**, respectively. For the RGO, the survey scan depicted in **Figure 32(a)** only shows carbon and oxygen peak and there is no any kind of undesired product present. The atomic ratios of C:O estimated from the survey scan are 6.56:1 that is higher than that of reduced GO via reflux condition in various organic solvents[155] and it is comparable with the atomic ratios of C:O from reduced GO prepared by solvothermal route in NMP.[156] The high-resolution C1s and O1s XPS spectra of RGO are shown in **Figure 32(b)** and **(c)** indicate that a majority of carbon species is sp^2-carbon (72%) and oxygen atoms are present in the form of hydroxyl (46%), carbonyl (34%), and ether (20%) functional groups. According to the high-resolution S2p XPS spectrum shown in **Figure 32(d)**, there is no sulfur functional group present in reduced graphite oxide.

Meanwhile, **Figure 33(a)** shows existence of carbon, oxygen, sulfur, and phosphorous peaks in the survey scan of m-RGO. The C:O:S atomic ratios of m-RGO calculated are 12.7:1:1.2. The high-resolution XPS spectrum of phosphorous (not shown here) indicates the presence of higher valent phosphorous and the binding energy of higher valent phosphorous resembles with P–O binding energy.[149] The high-resolution XPS spectrum of C1s (**Figure 33(b)**) shows large FWHM envelope which indicates different types of carbon species at the carbon surface and a major component is sp^2-carbon (75%). The deconvoluted high-resolution XPS spectrum of O1s shown in **Figure 33(c)** represents that there are several types of oxygen atoms that can form C–O, C═O, P–O, and/or S═O. The binding energy difference of C═O, P–O, and S═O is less than 0.4 eV and thus these three components were not properly separated each other because the used XPS

instrument can't resolve those three components due to resolution limitation (0.4 eV). The high-resolution S2p XPS shown in **Figure 33(d)** clearly shows presence of thiol (–SH), thiocarbonyl (C═S) as well as sulfonic acid (–SO_3H) groups in graphite oxysulfide but thiol functional group (83%) has come out as a major sulfur functional group.

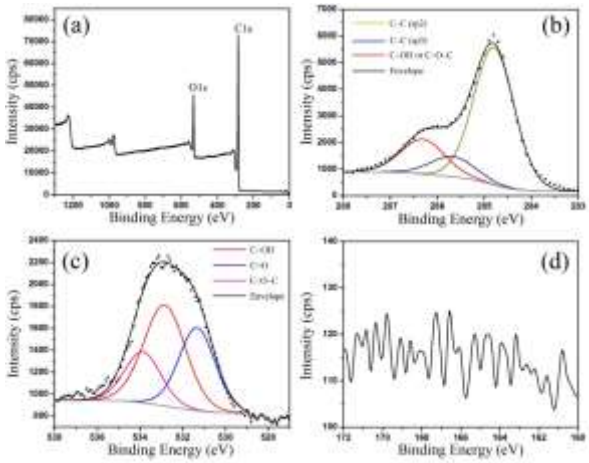

Figure 32. (a) Survey X-ray photoelectron spectral scan, (b) high-resolution XPS scan of C1s; (c) O1s; and (d) S2p of RGO.

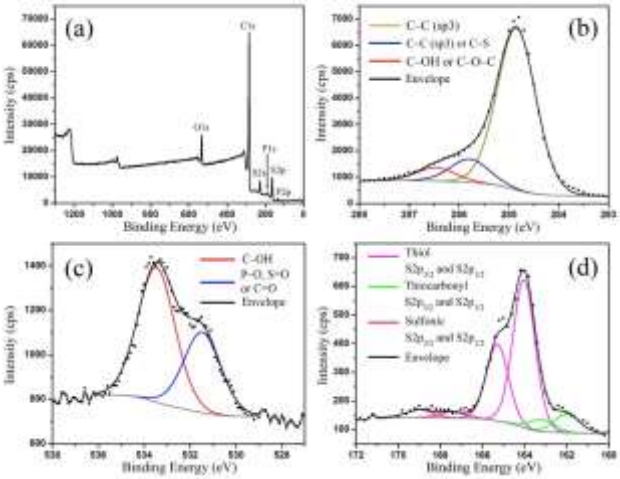

Figure 33. (a) Survey X-ray photoelectron spectral scan, (b) high-resolution XPS scan of C1s; (c) O1s; and (d) S2p of m-RGO.

Scanning transmission electron microscope equipped with energy dispersive X-ray spectroscopy (STEM-EDS) was carried out to estimate chemical compositions of m-RGO. For STEM-EDS analysis, it is more important to compare O:S atomic ratios rather than comparison of C:O:S atomic ratios because of the existence of carbon grid. Each area of O:S atomic ratios was shown differently, which indicates that oxygen and sulfur atoms are not homogeneously distributed on graphene matrix. One area of them is shown in **Figure 34**. In STEM-EDS spectrum, Cu peak is also shown because of TEM Cu grid. And the average O:S atomic ratios of m-RGO are 1:0.9±2, which is consistent with the result of XPS. The elemental mapping image of m-RGO shown in **Figure 35** indicates that oxygen and sulfur functional groups are well distributed on m-RGO sheet.

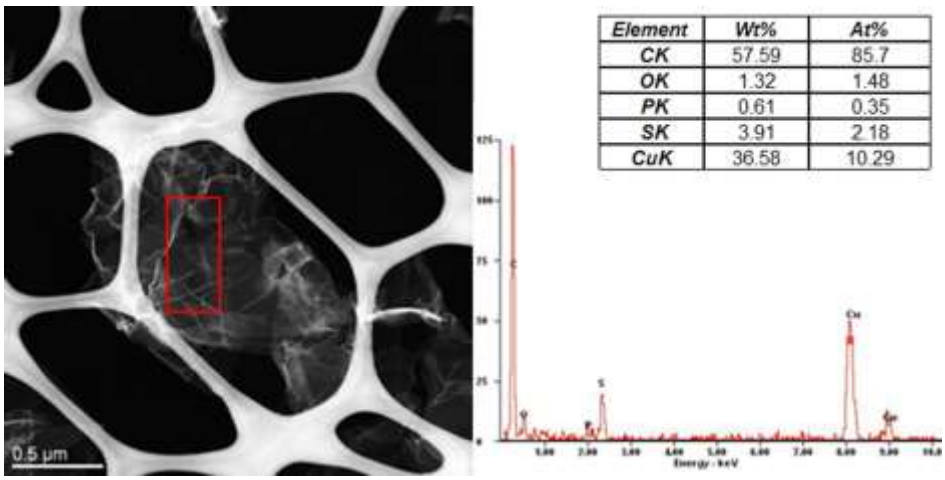

Element	Wt%	At%
CK	57.59	85.7
OK	1.32	1.48
PK	0.61	0.35
SK	3.91	2.18
CuK	36.58	10.29

Figure 34. Scanning Transmission Electron Microscope equipped with Energy Dispersive X-ray Spectroscope (STEM-EDS) image and the corresponding EDS spectrum of m-RGO.

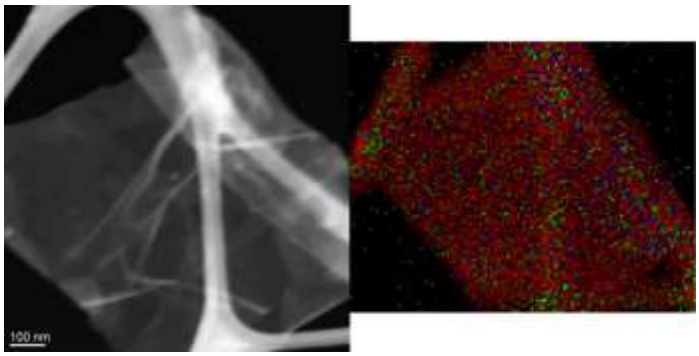

Figure 35. Dark field STEM image of m-RGO (left) and the corresponding elemental mapping image of m-RGO (right). Red represents carbon, green represents oxygen, and blue represents sulfur.

In order to confirm the presence of thiols on m-RGO, attenuated total reflectance-Fourier transform infrared (ATR FT-IR) was carried out with dispersion of RGO and m-RGO in ethanol. The ATR FT-IR spectra from 800 to 550 cm^{-1} of RGO and m-RGO dispersion were shown in **Figure 36**, respectively. The RGO dispersed in ethanol does not show any distinct peak within the spectrum range. In contrast to RGO dispersion, m-RGO dispersed in ethanol shows an absorption peak centered at 665 cm^{-1} which is attributed to C–S stretching mode in thiols.[157]

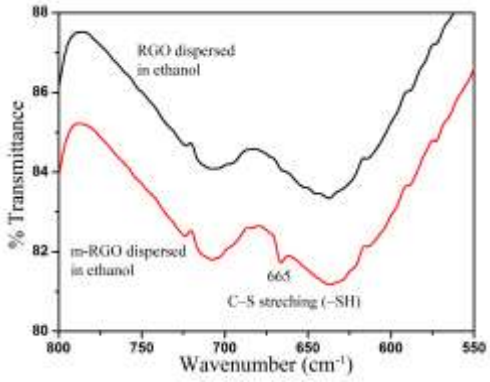

Figure 36. ATR FT-IR spectra for supernatant solution of RGO (black) and m-RGO (red) dispersed in ethanol.

The m-RGO has been synthesized through solvothermal reaction condition performed at different reaction temperatures and the sample names were designated according to the reaction temperatures such as 120 °C, 150 °C, and 180 °C (See **Table 2)**. The second portion of the sample names e.g. 120, 150, and 180 indicates the corresponding reaction temperatures such as 120 °C, 150 °C, and 180 °C, respectively. The atomic % of sulfonic functional group is the rest of the summation of the other sulfur functional groups because it is not presented in **Table 2**. In order to understand the thermal stability of m-RGO as well as different sulfur functional groups, heat-treatment of m-RGO was performed at 600 °C under Ar atmosphere for 10 minutes.

Table 2. Detailed XPS data analysis of m-RGO samples as well as before and after heat treatment depicts the atomic % ratios of C, O, S, and C/S. Atomic % of –SH as well as C═S groups from deconvoluted high-resolution X-ray photoelectron spectra of sulfur.

Sample name	C	O	S	C/(S+O)	(–SH) (atomic %)	(C═S) (atomic %)
m-RGO-120	9.7	1	0.7	5.71	86.1	9.14
m-RGO-150	10.5	1	0.9	5.53	80.9	11.8
m-RGO-180	12.7	1	1.2	5.77	82.6	11.8
m-RGO-120 (heated at 600 °C)	14	1	0.41	9.93	100	0
m-RGO-150 (heated at 600 °C)	16	1	0.54	10.4	100	0
m-RGO-180 (heated at 600 °C)	18	1	0.84	9.78	100	0

The TGA results and the high-resolution S2p XPS spectra were shown in **Figure 37** and **Figure 38**, respectively. Additionally, the corresponding XPS results are tabulated in **Table 2**. Interestingly, after heat-treatment, all sulfur functional groups such as thiocarbonyl (C═S), and sulfonic ($-SO_3H$) functional group were removed except thiols (–SH), which indicates thiols are more thermally stable than the other sulfur functional groups.

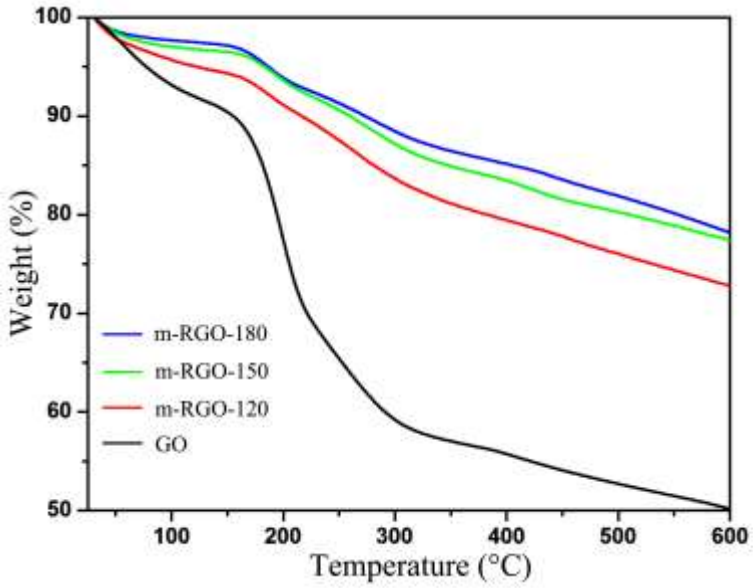

Figure 37. TGA curves of GO, m-RGO-120, 150, and 180 °C.

The increase in sulfur content with increasing reaction temperature was reflected in the increased atomic % ratio of sulfur (S) as well as in decreased C/S atomic ratio (See **Table 2**). The atomic ratios of C/(O+S) with different reaction temperature are almost all the same each other but the sulfur content was increased with increasing reaction temperature, which represents that more oxygen functional groups were replaced by sulfur functional groups with higher reaction temperature. It was also observed even if the amount of P_4S_{10} was used during the course of the reaction as much as 50% excess than that of stoichiometric amount of P_4S_{10}, the

sulfur content in mercapto reduced graphite oxide was not changed significantly with varying reaction temperatures, indicating that 10% excess amount of P_4S_{10} is enough to obtain the maximum sulfur content in the samples. It was found from the deconvoluted high-resolution S2p XPS spectrum that thiols (–SH) exist as a major (80-85 atomic %) sulfur functional group in m-RGO. The existence of other sulfur functional groups such as thiocarbonyl (C═S) and sulfonic acid ($-SO_3H$) groups were also shown as minor sulfur functional groups evidenced from the deconvoluted high-resolution XPS of sulfur.

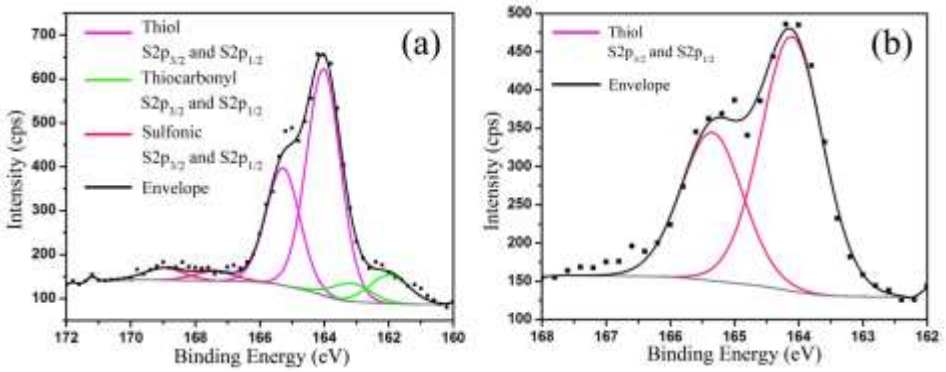

Figure 38. High-resolution S2p XPS spectrum of m-RGO: (a) before heat-treatment and (b) after heat-treatment at 600 °C.

Figure 39 shows atomic force microscopy (AFM) images and corresponding height profile of m-RGO. AFM images of m-RGO were obtained by dispersing m-RGO in ethanol and then drop casted on freshly cleaved mica after sonication for 30 minutes follwed by centrifugation at 6000 rpm for 10 minutes. It is evidient from the height profile that the average thickness of the layer is about 1 nm which indicates that completely exfoliated m-RGO sheets deposited on mica.[28c] From height profile in **Figure 39(c)**, there are some spikes on the m-RGO surface due to wrinkled m-RGO sheets on the substrate. Additionally, some few-layered m-RGO re-stacked

together during evaporation were also found in low magnification. The general morphology of m-RGO is irregular and lateral dimension is in the range from a couple of tenth nano-meters to about 1 μm.

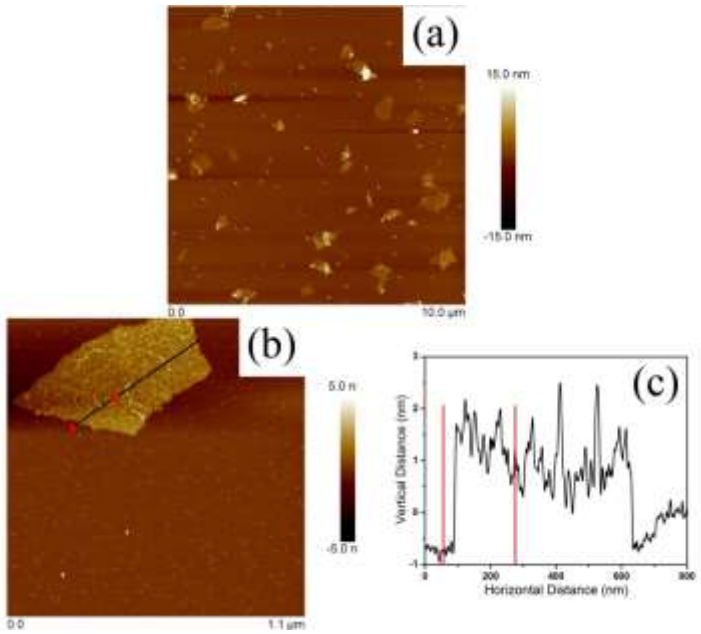

Figure 39. (a) Low magnification; (b) high magnification AFM images; and (c) corresponding height profile of m-RGO. The scanned areas are 10.0×10.0 μm^2 and 1.1×1.1 μm^2 respectively.

4.4 Concluding Remarks

It has been sucessfully demonstrated that through a facile one-pot low-temperaure solvothermal synthesis, bulk quantity of m-RGO has been produced with both oxygen and sulfur functinal groups on its surface utilizing Berzelius reagent. The amount of the sulfur functional groups can be easily tuned simply by varying the reaction temperatures as well as the sulfur functional groups can be controlled by short heat-treatment at 600 °C. This as-synthesized material, m-RGO, contains 19.4 wt% of sulfur and thiol (–SH) as the major functional group. Among the sulfur

functional groups, thiols are more thermally stable. To best of my knowledge, m-RGO has been synthesized for the first time using P_4S_{10} as a thionating agent. These thiol functional groups on graphitic matrix can be exploited in different potential purposes like self-assembly monolayer (SAM) on gold substrate,[137] heavymetal scavenger,[138a] and as a biosensor.[139a] This unique and new thionating strategey could be applied to convert oxygen to sulfur functinal groups for other carbonaceous materials and biopolymers containing oxygen functional groups.

CHAPTER 5

FABRICATION OF TRANSPARENT CONDUCTING THIONATED REDUCED GRAPHENE OXIDE THIN FILM

5.1 Introduction

Transparent and electrically conducting glass electrodes have been widely used in various photoelectronic devices.[158] To dates, metal oxides such as indium tin oxide (ITO) and fluorine tin oxide (FTO) have been widely used as materials for glass electrodes. These metal oxides, however, are becoming increasingly problematic due to limited availability of indium, instability in the presence of acid and base, reduced transparency in the near infrared (IR) region, and their susceptibility to ion diffusion in polymer layers.[18b, 159] Graphene has been considered as a possible alternative electrode material because of the high optical transmittance of 97.7% for a single layer at 550 nm and electrical conductivity.[13, 18b, 160] Graphene films can be directly fabricated by chemical vapor deposition (CVD)[51b] and epitaxial growth on SiC.[6b] Aforementioned techniques require specific substrates, and not scalable and cheap.

Another approach for fabrication of graphene film is to use graphene dispersion[161] or reduced graphene oxide (RGO) dispersion.[162] Because the product yield of RGO dispersion by ultra-sonication is extremely low, this approach is not suitable for fabrication of large-area films by directly using RGO dispersion. A stable colloidal dispersion of graphene oxide (GO) in water can be easily obtained by ultra-sonication due to the presence of hydrophilic oxygen functional groups. The GO thin film preparation methods such as drop-casting,[163] spin-coating,[160] dip-coating,[18b] spraying,[164] vacuum filtration,[162] and Langmuir-Blodgett (LB) assembly[165] have been developed. These GO films, however, require extensive chemical reduction or thermal reduction to produce electrically conducting thin film. The reduced graphene

oxide (RGO) film also can be directly fabricated from RGO suspension by vacuum filtration.[162]

Self-assembly process at liquid-air interface and liquid-liquid interface can also form GO, RGO, and graphene thin films. Graphene oxide film forms at pentane-water interface by the evaporation of pentane through rapid injection of ethanol into a GO dispersion.[166] Graphite oxide membranes were obtained by evaporation of GO dispersed in water.[167] As-fabricated GO film or membrane requires chemical or thermal reduction to produce electrically conductive film or membranes and these methods are tedious due to evaporation of solvent step. Graphene thin film can directly form at chloroform-water interface after sonication of the mixture.[168] The amount of graphene dispersed in chloroform, however, is very small and this is not suitable for formation of large-area film. Moreover, it is also difficult to obtain continuous large-area thin film because thin films can be easily cracked during transfer to the desired substrates. These drawbacks make this process unsuitable for fabrication of continuous large-area thin films. Reduced graphene oxide thin film can be fabricated at water-air interface after chemical reduction of GO dispersion.[169] During chemical reduction, almost all of RGO sheets precipitate out at the bottom and very small amount of RGO sheets that float on the water form RGO thin film. This method is also unsuitable for production of large-area RGO film on water.

It is important to develop a new fabrication method to produce continuous, large-area, and conducting thin film in order to apply the graphene thin films for many applications such as field emission device (FED)[170], organic solar cell[171], organic light-emitting diodes,[172] and so on. The new fabrication method developed could at least satisfy the following two issues: 1) minimize loss of active material and 2) avoid post-treatment e.g., chemical or thermal reduction. Herein, a facile fabrication of continuous large-area transparent conducting reduced graphene oxides thin film on

various substrates is reported for the first time by using homogeneous RGOs that are thiol-functionalized (m-RGOs) dispersion. The synthesis of m-RGO was reported in my previous work (see **Chapter 4**). Advantages of the described fabrication process are no limitation on size, shape, and substrate material, no additional reduction is required, no loss of active materials, and specific instrumentation for fabrication is not needed.

5.2 Experimental Section

5.2.1 Synthesis of Graphene Oxides (GOs)

GOs were synthesized by using a modified Hummers method through oxidation of natural graphite flake with strong oxidants.[34] In a typical procedure, 1 g of natural graphite flake (Sigma-Aldrich) was ground with 5 g of NaCl (Alfa Aesar, 99+%) until the mixture becomes homogeneous by visual inspection. NaCl from the mixture was then washed away using deionized water with vacuum filtration. The ground graphite on the filter paper was dried at 110 °C in a lab oven for 2 hours to remove all physisorbed water. 0.765 g of $NaNO_3$ (Sigma-Aldrich, ≥ 99.0%) was first dissolved in 40 mL of concentrated H_2SO_4 (Sigma-Aldrich, ACS reagent, 95 ~ 98%) in a 400 mL of beaker with stirring for 20 minutes. About 1 g of the dried ground graphite was then added to the beaker with keep stirring. Subsequently, the beaker was placed in an ice bath and then 5 g of $KMnO_4$ (Sigma-Aldrich, ≥ 99.0%) was slowly added to the beaker while the temperature was kept below 10 °C. Afterward, the beaker was removed from the ice bath. The mixture in the beaker was then heated around 40 °C with vigorously stirring until it became pink thick paste. 100 mL of deionized water was added to the beaker and 20 mL of H_2O_2 (Alfa Aesar, ACS reagent, 29 ~ 32%) was slow added to the suspension subsequently to finish the reaction. After the reaction, the color of the suspension became bright yellow. The

suspension was then repeatedly centrifuged and the precipitate was washed with diluted HCl until $BaCl_2$ (Anhydrous purified, J.T. Baker chemical Co.) test shows a negative result.

5.2.2 Synthesis of Mercapto Reduced Graphene Oxides (m-RGOs)

The purified GOs in water (pH ~4) were mixed with 1 *M* NaOH solution to obtain GOs precipitate and subsequently the pH was adjusted around 9 by rinsing with deionized water. The solvent exchange of the GOs sludge was performed with 100 mL of pyridine vacuum filtration to ensure complete removal physisorbed water. The washed GOs sludge with pyridine was homogenized for 10 minutes to obtain exfoliated GO in pyridine for further sulfidation reaction. For the synthesis of m-RGO *via* solvothermal reaction route, phosphorus decasulfide (P_4S_{10}, Sigma-Aldrich, 99%) has been used as a source of sulfur. To get control over the amount of sulfur incorporation in graphitic network, the amount of the phosphorus decasulfide (P_4S_{10}, sulfur precursor) as well as the reaction temperature were varied. Hereafter, all m-RGO samples, unless otherwise stated, were synthesized by using 10% excess with respect to stoichiometric amount of P_4S_{10}. In a typical solvothermal reaction, 220 mg of P_4S_{10} (10% excess with respect to stoichiometric amount of P_4S_{10}) was added to 200 mg of GOs in 13 mL of pyridine in a Teflon-lined autoclave of capacity of 23 mL. It was then placed in an oven pre-heated at 120, 150 and 180 °C for 15 hours. After the reaction, the solid product was collected *via* vacuum filtration and it was washed several times with deionized water and ethanol to remove all the unreacted P_4S_{10} and by-products. The mercapto reduced graphene oxides (m-RGOs) in water were freeze-dried for further characterization. This final product can be easily dispersed in various solvents like H_2O, DMF, DMSO, NMP, etc. by sonication for 30

minutes to achieve the stable dispersion of mostly single or bi-layer m-RGO in wide range of solvent media.

5.2.3 Fabrication of Mercapto Reduced Graphene Oxide (m-RGO) Langmuir-Blodgett (LB) Film

The mercapto reduced graphene oxides (m-RGOs) LB films have been fabricated using m-RGOs dispersion in absolute ethanol. The m-RGOs supernatant solution was obtained after centrifugation at 6000 rpm for 10 minutes to remove un-exfoliated m-RGOs. This dispersion was dropped on top of the deionized water surface in a glass petri dish. The m-RGO sheets are invisible with a couple of drops of m-RGOs suspension but very thin m-RGOs Langmuir film could be visible on top of the water surface in the petri dish after adding about 0.3 mL of m-RGOs dispersion. The mercapto reduced graphene oxides (m-RGOs) Langmuir film on the surface of water in the petri dish gradually spreads out with addition of the m-RGOs suspension and eventually, entire water surface is covered by m-RGOs thin film. In order to fabricate transparent conducting m-RGOs thin films on various substrates, the m-RGOs thin film on the surface of water could be transferred to various substrates by scooping the m-RGOs Langmuir film on water with the substrates. Hereafter, this method is called "scooping method". Another method to fabricate m-RGOs LB film is to place the substrate in the glass petri dish with several holes on the bottom and to put the petri into larger petri dish. The larger petri dish was filled with deionized water 80% full and then m-RGOs dispersion was added to the surface of the water. Once the m-RGOs Langmuir film forms the water in the larger petri dish was slowly removed by pipette until the m-RGOs thin film on the water stands on the substrate and the m-RGOs LB film was dried at atmosphere condition. This method is called "water draining method".

5.2.4 Materials Characterization

X-ray photoelectron spectroscopic (XPS) measurements were carried out using a VG-220IXL spectrometer with a monochromated Al Kα radiation (1486.6 eV, line width 0.8 eV). The pressure in the analysis chamber was about 10^{-9} torr while recording the spectra. The spectrometer has an energy resolution of 0.4 eV. All the binding energies were corrected with reference to C(1s) at 284.6 eV. Deconvolution of the spectrum was done using the CASA software with the accuracy of 0.2 eV. Shirley background was used for the deconvolution. For the high-resolution C1s XPS spectrum was deconvoluted into the following three components: C–C (sp^2- and sp^3-hybridized peaks at 284.7 and 285.4 eV, respectively),[37] C═O (carbonyl peak at 287.6 eV),[173] and C–O (hydroxyl peak at 286.5 eV).[104] Carbon atoms with the C–S bond were not separately treated because the C1s binding energy of C–S (285.3 eV)[105] is too close to that of C–C (sp^3-hybridization) and thus could not be resolved, given the resolution of the XPS instrument (0.4 eV). The high-resolution O1s XPS spectrum was presented with the following oxygen functional groups: C═O (531.7 eV)[106, 149] and C-OH (533 eV).[60a] The high-resolution S2p XPS spectrum was deconvoluted with thiol ($S2p_{3/2}$ at 164.0 eV with FWHM of 1.2 eV; $S2p_{1/2}$ at 165.2 eV with FWHM of 1.2 eV).[108] The area ratio and splitting energy difference between $S2p_{3/2}$ and $S2p_{1/2}$ spin-orbit doublet peaks were 2:1 and 1.2 eV, respectively.

The transmittance curves of m-RGO LB films were acquired on a UV-Vis spectrometer Lambda 650 S (Perkin-Elmer). Surface topography images were obtained using atomic force microscope (AFM) (Pico-Plus AFM, Molecular imaging, Agilent technologies) and profilometry. The profilometry is a Zescope non-contact white light optical profilometer from Zygo. The data were acquired and processed using the software ZeMaps. All AFM studies were performed in air using a tapping mode with SCANASYST-AIR tips (Bruker). The m-RGO suspension in 200-proof

ethanol obtained after ultrasonication for 40 minutes and subsequently centrifuged at 6000 rpm for 10 minutes was used for fabrication of m-RGOs LB films on freshly cleaved mica. The images were collected at a scan rate of 1.0 Hz in air.

The Confocal Raman Microscope by WITec (Germany) is based on an Alpha300 WITec microscope, equipped with EC-EPIPlan 20x (NA 0.4), 40x (NA 0.8), and 100x (NA 1.25) microscope objectives (Zeiss GmbH, Germany). The sample is mounted on a piezoelectrically driven XY scan stage (PI-P527, Physik Instruments, Germany). Adjustments of the sample on the vertical axis (Z-direction) are performed by using the Alpha300 microscope built-in scan stage. Sample excitation is provided by a 532 nm CW solid-state laser (Excelsior 532-60, Spectra Physics-Newport Corporation). The laser is coupled to an optical fiber, and then directed into the back entrance of the microscope body and focused on the sample by selecting the appropriate microscope objective (generally 40x, NA 0.8, or 100x NA 1.25, for Raman applications). The signal from the sample is collected through the same objective and directed toward a mirror-based spectrograph (Acton SP2300, Princeton Instruments, USA). The spectrometer is equipped with two gratings: one with 600 grooves/mm, centered at 595 nm on the CCD chip, and covering a spectral range of >3600 cm^{-1}, and a second one with 1800 grooves/mm, centered at 548 nm on the CCD chip, and covering a spectral range of >1100 cm^{-1}. The spectrograph is connected to a DV401A-BV CCD camera (Andor Technology), with an imaging area of 26.6×3.3 mm^2, covered by 1024×127 pixels with a size of 26×26 μm^2 each. To minimize electronic noise, the camera is cooled at -60 °C during operation. The spectrally resolved signal from the spectrograph is imaged onto the CCD sensor to record a full Raman spectrum. Control of the instrument and data recording are achieved through the WITec Control software (v. 1.58, WITec GmH, Germany) provided with the instrument.

After m-RGOs film was deposited on to 1 cmx1 cm glass substrate, drops of sliver paint (2SPI Supplies / Structure Probe, Inc.) was applied at four corners of the sample forming dots of diameter ~1.5 mm. After drying of the silver paint in ambient, the sample was then loaded into a four-point probe, with four springs loaded pogo-pins pressed firmly onto the silver paint contact dots. The sheet resistance was then measured with the standard Van der Pauw scheme; a current (I) was sourced between the two contact dot long one side of the sample, and the voltage (V) measured across the contacts on the opposite side. The sample sheet resistance ($R_{\square}$) can be obtained as $R_{\square}=4.53V/I$.[174] Note that the current source used (Keithley 6221) has output impedance of $\sim 10^{14}$ that is well suited for my measurement. The temperature was changed by slowly lowering the dipping probe into a dewar of liquid He, and temperature was measured using a calibrated silicon diode sensor; both sample and diode sensor are in good thermal contact with the two faces of a thin block of copper.

The Nano-Secondary Ion Mass Spectrometry (NanoSIMS) measurements were done using a Cs^+ primary ion beam with the Cameca Ametek NanoSIMS50L at Arizona State University. The beam current at the sample was lowered to ~0.48 pA by choosing a small diaphragm to get a much desired fine beam and high enough count rates for imaging of the sample. Negative secondary ions of ^{12}C, ^{16}O, ^{32}S and $^{32}S^{16}O$ were measured simultaneously using electron multipliers in the multicollection mode. Sufficient mass resolving power (MRP) to separate out mass interferences, e.g., ^{32}S from $^{31}P^{1}H$ (MRP > 4000), was maintained by choosing an appropriate entrance slit. Typical measurement condition varied from 10×10 μm^2 to 25×25 μm^2 analysis areas and 10-15 layers. Each area was divided into 256^2 pixels with dwell times of 40 msec/pixel. The ion images from multiple layers were corrected for

beam drifts using the WinImage software and the last 8-12 layers were added to form summed ion images.

5.3 Results and Discussions

The schematic illustration of m-RGOs LB film fabrication procedure (scooping method) is depicted in **Figure 40**. The m-RGOs LB film can be fabricated by either scooping method or water draining method but **Figure 40** only illustrates the scooping method. Initially, when m-RGOs dispersion is added to the surface of water one drop at a time, m-RGO sheets freely move around on the water surface and it is very difficult to recognize them due to its very thin and small sheets. After about 0.5 mL of m-RGOs dispersion is dropped on the water surface, m-RGO sheets are visible clearly and a part of the water surface is covered by m-RGOs thin film.

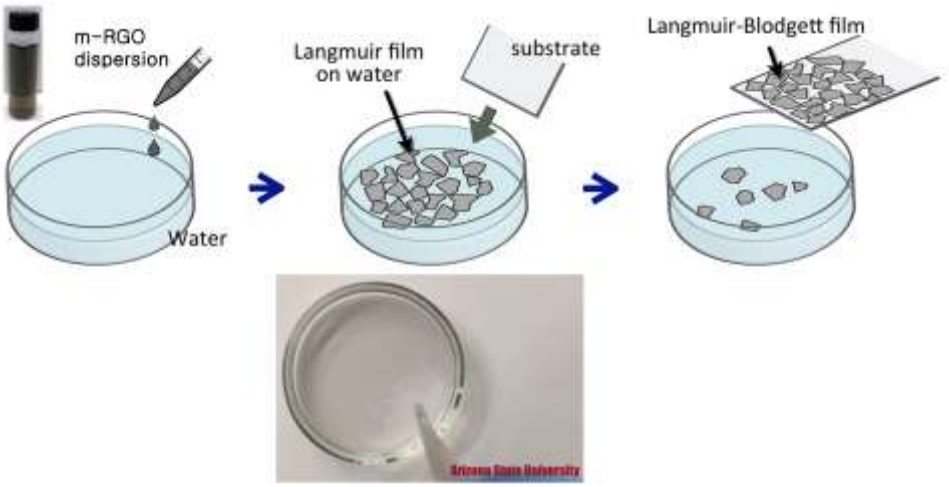

Figure 40. Schematic illustration of m-RGOs LB film fabrication procedure and photographs of m-RGOs dispersion in ethanol and m-RGOs Langmuir film on the surface of water.

The size of m-RGOs Langmuir film gradually increases by adding more m-RGOs dispersion in ethanol. Once m-RGOs thin film is clearly seen with bare eyes, the

average thickness of m-RGOs Langmuir film becomes around 5 or 6 nm thick. When m-RGOs Langmuir film covers the entire water surface, the m-RGOs thin film can be easily transferred to any kinds of substrate such as glass, mica, or Au. Although not shown here, m-RGOs LB film could be fabricated with m-RGOs dispersed in other organic solvents such as DMF, DMSO, or NMP.

XPS survey scan, high-resolution C1s, O1s, and S2p spectra of as-synthesized m-RGOs were represented in **Figure 41**. After synthesis of m-RGOs, the elemental analysis was carried out by using X-ray photoelectron spectroscopy (XPS). The estimated C:O:S atomic ratio of m-RGOs from XPS wide scan shown in **Figure 41(a)** was 13:1:0.9, and the XPS survey scan indicates that all byproducts and unreacted P_4S_{10} were completely removed. The high-resolution C1s XPS spectrum implies that the sp^2-carbon species in m-RGO are significantly restored. C–S binding energy (285.3 eV)[155] is very close to the binding energy of sp^3-hybridized carbon species and the binding energy difference between them is less than the resolution limit (0.4 eV) of the XPS and thus C–S bond was not resolved. There is no doubt that m-RGO was reduced during the synthesis according to not only atomic ratios of m-RGO but also the high-resolution C1s XPS. Both high-resolution C1s and O1s XPS spectra show that the obtained m-RGO still contains some oxygen functional groups such as hydroxyl and carbonyl groups. The as-synthesized m-RGO contains only thiol functional group confirmed by high-resolution S2p XPS spectrum shown in **Figure 41(d)**. The high-resolution S2p XPS spectrum shows two distinct peaks due to spin-orbit coupling effect.

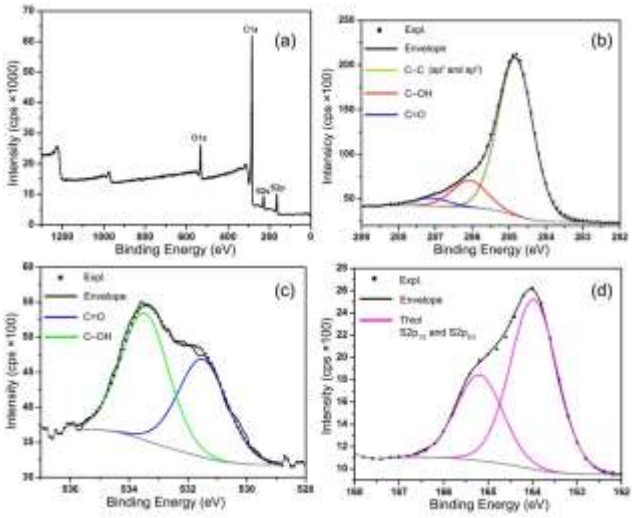

Figure 41. XPS spectra of m-RGO: (a) wide scan, (b) high-resolution C1s, (c) high-resolution O1s, and (d) high-resolution S2p.

Transmittance and sheet resistance of m-RGOs LB film were studied to examine the optical and electrical properties of the films as well as how significantly sulfur functional groups affect to the sheet resistance of the film. **Figure 42** shows transmittance curve of m-RGO LB film and sheet resistance and the corresponding digital camera photograph is represented in **Figure 43**. In the m-RGOs LB film photograph, silver paste was applied at each corner of the film for electrical conductivity measurement. The m-RGOs LB film on slide glass (1×1 cm^2) is highly transparent and m-RGO sheets are homogeneously distributed on the glass substrate macroscopically. The m-RGOs LB films show a flat optical transmittance profile in visible light and near infrared region. The transparency of m-RGOs LB films was determined at 550 nm wavelength incident light, and the transmittance of m-RGOs LB films was 92% and 91%, respectively. The average number of 92% and 91% transmittance m-RGO sheets on each film is around 4 layers because each layer of graphene can reduce the transmittance of about 2.3%.[13] The optical property of m-RGOs is almost all the same as graphene, which is reported in **Chapter 4**. Although

not shown here, the thickness of m-RGOs film could be easily controlled by changing the concentration of m-RGOs dispersion. The sheet resistance of the corresponding m-RGOs LB film on the slide glass was measured by Van der Pauw four-probe method. Although the transparency of m-RGOs LB film is almost all the same with each other, the sheet resistance of m-RGOs LB films with different content of sulfur is very different. The mercapto reduced graphene oxides (m-RGOs) LB film with higher sulfur content and lower sulfur content show the sheet resistance of 500 kΩ/sq and 1.3 MΩ/sq at room temperature, respectively. This result indicates that sulfur functional group can significantly improve the electrical conductivity. This might happen probably because the orbital overlap between sulfur 3s and 3p with π-orbitals in the graphene sheets improve the electrical conductivity. The sheet resistance of reduced graphene oxides (RGOs) thin film is highly depending on the physical contact of each graphene sheet to the substrate[175] because the sheet resistance of slightly thicker m-RGOs film might be significantly reduced as well. Additional heat treatment can improve the electrical conductivity of reduced graphene oxide film dramatically.[169a] Therefore, the sheet resistance of m-RGOs LB film may be further decreased.

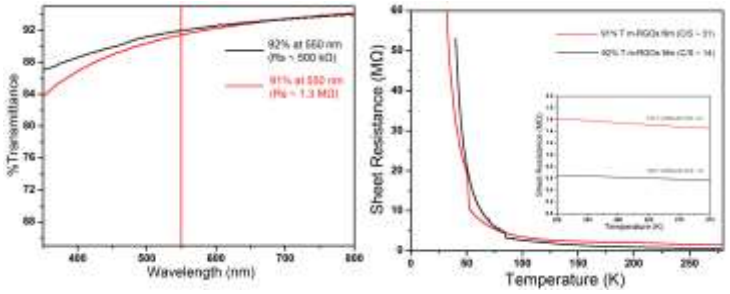

Figure 42. Transmittance of m-RGOs LB films on slide glass (left) and the corresponding sheet resistance of m-RGOs LB film (right).

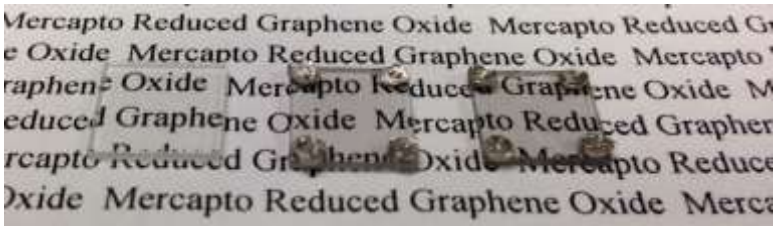

Figure 43. Digital camera photograph of plain glass (left), 92% optical transparent m-RGOs LB film (middle), and 91% optical transparent m-RGOs LB film (right).

In order to study the general morphology, thickness, and root mean square (RMS) roughness of m-RGOs thin film on water and on glass substrate, profilometry was employed. The 1.7×1.7 mm^2 scanned profilometry images of m-RGOs Langmuir film and m-RGOs LB film are shown in **Figure 44**, respectively. Both m-RGOs Langmuir film and LB film show around 1 nm RMS roughness, which indicates the surface of both films on water and glass substrate is very smooth. It is noted that there are some thicker areas on both m-RGO thin films due to the presence of re-stacked, folded, or wrinkled m-RGO sheets. The thickness of both m-RGOs thin films on water and glass substrate is around 6 nm. According to the profilometry images of m-RGOs Langmuir and m-RGOs LB films, both m-RGOs sheets are well physically contacted together on the surface of water and glass substrate.

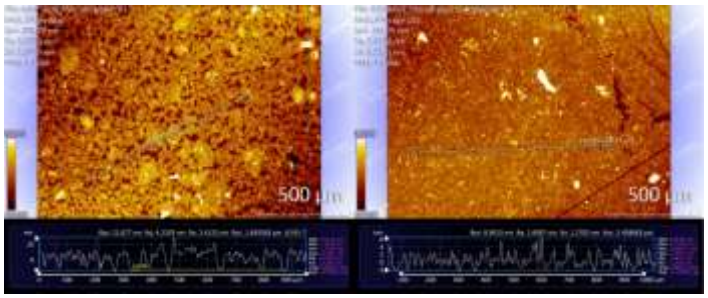

Figure 44. Profilometry images of m-RGOs Langmuir film on water (left) and m-RGOs LB film on glass substrate by scooping method (right).

In order to study the morphology of m-RGOs LB film microscopically, atomic force microscope (AFM) was carried out. The AFM images of m-RGOs LB film are represented in **Figure 45**. The mercapto reduced graphene oxides (m-RGOs) thin film on mica was fabricated by water draining method. Almost all m-RGO sheets are well exfoliated and distributed on the mica substrate. According to the AFM image of the m-RGOs thin film, each m-RGO sheet is wrinkled and folded, which is a general behavior of reduced graphene oxides LB film.[176] Some m-RGO sheets stacked together are observed as well. The thickness of m-RGOs is about 1 nm, which indicates m-RGO sheets are completely exfoliated.[165] The height profile shows some spikes and higher than 1 nm thickness; those are ascribed to wrinkle, fold, and/or stacking m-RGO sheets.

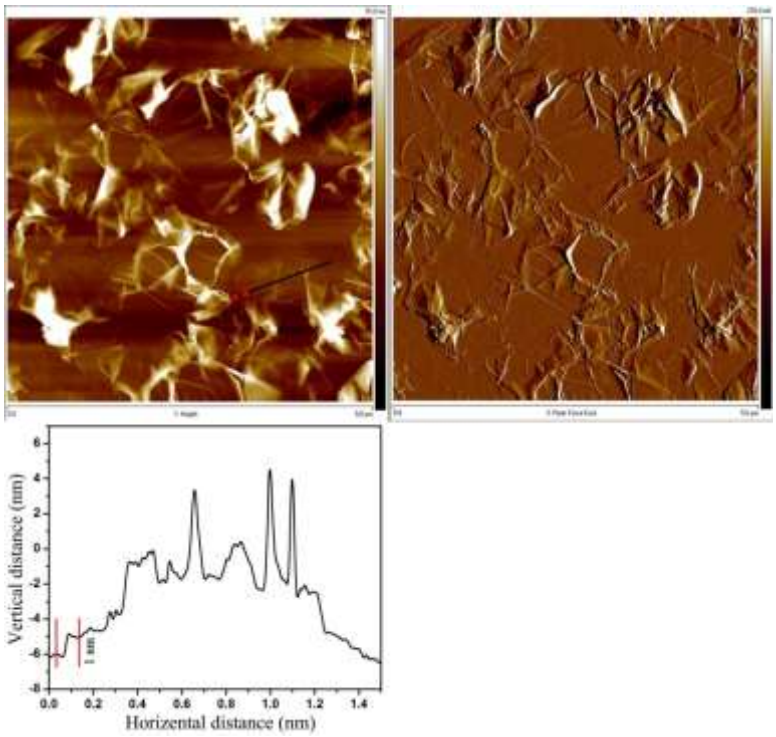

Figure 45. AFM height (left) and amplitude (right) image of m-RGOs LB film on mica and corresponding height profile (bottom left).

Raman spectroscopy is a useful technique for carbonaceous materials. For this particular work, D (around 1350 cm^{-1}) and G (around 1580 cm^{-1}) bands region become the focus of the study. Raman spectrum directly indicates a degree of deficiency of lattice on graphene sheets by comparison between D and G band intensity. Generally, graphene oxides show high I_D/I_G ratio (typically higher than 1) due to the presence of various oxygen functional groups both on the basal plane and at edge, as well as many defects generated during oxidation process.[177] **Figure 46** shows an optical image of m-RGOs thin films on slide glass substrate, Raman mapping image in the range from 1300 to 1600 cm^{-1} from the red box area, and averaged Raman spectrum of Raman mapping image. The m-RGOs thin film was fabricated on slide glass substrate by water draining method. The bright field image of m-RGOs film clearly shows m-RGOs film and glass area and m-RGO sheets are densely packed together. The Raman mapping image was obtained from the area in the red box of bright field image, and the intensity of the Raman mapping depends on the intensity of D (~ 1350 cm^{-1}) and G (~1580 cm^{-1}) band. The Raman mapping shows that m-RGO sheets are well distributed on the slide glass substrate. There are some brighter areas because of the presence of the different thickness of m-RGOs thin films. The I_D/I_G ratio of reduced graphene oxides, however, decrease (typically lower than 1) because of restoration of sp^2-hybridized carbon species during reduction process.[177] The Raman spectrum was obtained by averaging D and G band intensity out in the Raman mapping and the I_D/I_G ratio is around 1 which implies that m-RGO sheets contain many sp^3-hybridized carbon species and deficiency of lattice on the m-RGOs thin film due to the replacement of oxygen atoms in graphene oxide by sulfur atoms and defects produced during synthesis of m-RGOs.

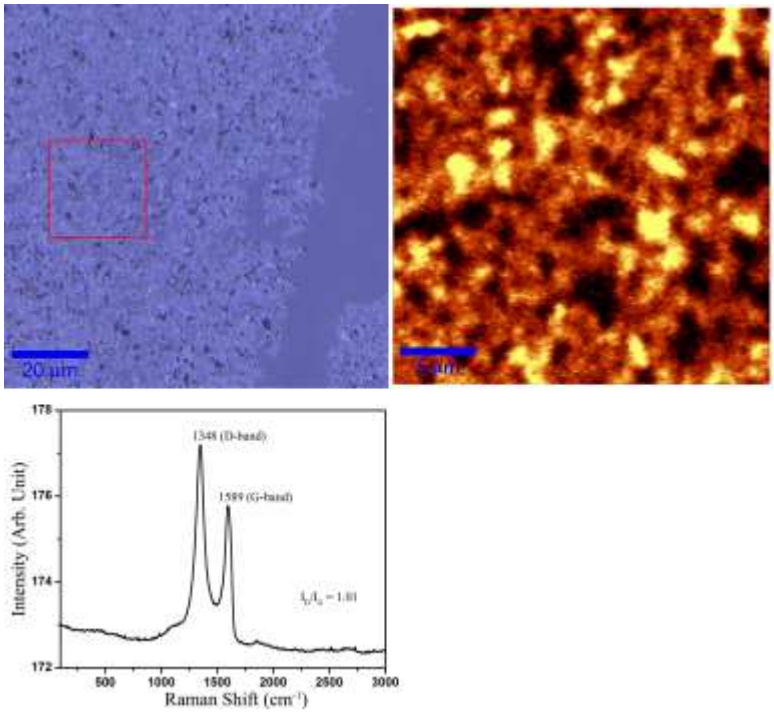

Figure 46. Confocal Raman spectroscopy of m-RGOs LB film. Bright field image of m-RGOs film (top left), Raman mapping in the range from 1300 to 1600 cm^{-1}(top right) from red box area of bright field image, and averaged Raman spectrum of Raman mapping (bottom left).

The NanoSIMS was used to investigate the distribution of carbon, oxygen, and sulfur on the m-RGOs LB film. NanoSIMS is a new generation double-focusing mass spectrometer,[178] which is characterized by high spatial resolution (up to 50 nm using the Cs^+ primary beam and ~200 nm with the O^- beam) necessary to investigate the films fabricated in this study. The last 5-12 layers were added to form summed ion images shown in **Figure 47**. The summed up images depicted in **Figure 47** shows clearly the distribution of oxygen and sulfur functional groups on the surface of the m-RGOs LB film. With the lateral resolution of about 50 nm, individual element could not be resolved. However, one can see the spatially

correlated O and S-rich hotspots (indicated by the red arrows in **Figure 47**) probably pertaining to several films adhering to each other.

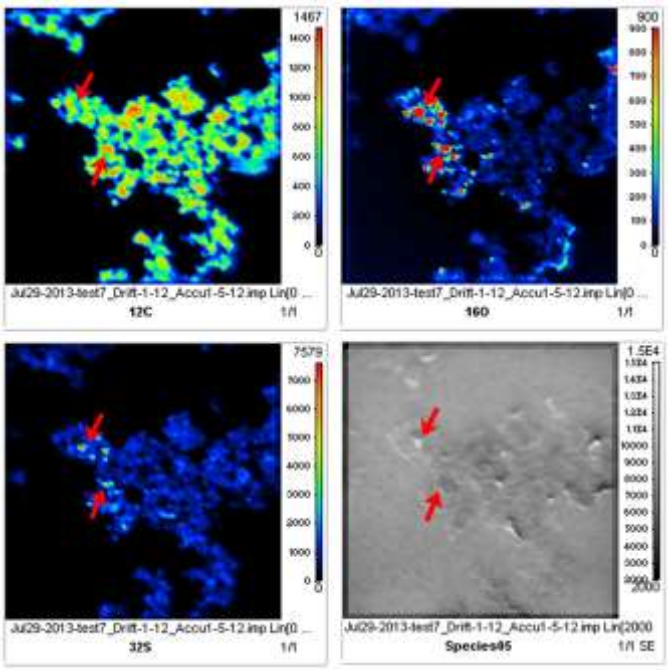

Figure 47. Ion images of $^{12}C^-$, $^{16}O^-$, and $^{32}S^-$ as well as secondary electron image of a 25x 25 um^2 area on a m-RGO LB film on an Au substrate using Nano-Secondary Ion Mass Spectrometry (NanoSIMS).

5.4 Concluding Remarks

It has been successfully demonstrated that a facile fabrication of transparent conducting m-RGOs Langmuir-Blodgett film on various substrates such as glass, mica, and Au without any specific instrumentation. The as-synthesized m-RGOs contain high density of thiol functional group and the thiol functional group could alter the surface property of the reduced graphene oxides. The sheet resistance of m-RGOs LB film can be dramatically reduced with higher sulfur content of the m-RGOs LB film, which may be ascribed to overlapping sulfur 3s and 3p orbitals with π-

orbitals in graphene sheets. Nano-SIMS elemental analysis reveals that thiol functional groups are well distributed on m-RGOs LB film. The thiol functional groups are present on the surface of the fabricated m-RGOs film, thus the thiol functional group present on the surface of the m-RGOs thin film might be utilized for further applications such as fabrication of a robust Au film on plastic substrate and biomolecule sensor utilizing thiol as a cross-linker. Additionally, this simple and powerful a new fabrication of thin film method may facilitate the uses of graphene film to various applications.

CHAPTER 6

DEPOSITION OF MERCAPTO REDUCED GRAPHENE OXIDE ON GOLD ELECTRODE

6.1 Introduction

Various substrates have been used for fabrication of graphene oxides (GOs), reduced graphene oxides (RGOs) films through several different methods such as drop-casting,[163] spin-coating,[160] vacuum filtration,[28d] or Langmuir-Blodgett (LB) technique.[175] Among various substrates, Au substrate has been used for various purposes. However, there is no report of fabrication of graphene oxides (GOs) or reduced graphene oxides (RGOs) film on gold substrate. This is because although GOs or RGOs film might be fabricated on the Au substrate, the GOs or RGOs films could easily be peeled off from the surface of Au substrate due to inertness of the gold surface. The Au surface shows a very good affinity with soft-bases and thiol is one of the soft-bases. Therefore, deposition of organosulfur molecules to the Au substrate has been intensively carried out. In my previous work, thiol-functionalized reduced graphene oxides (m-RGOs) have been successfully synthesized via two different methods described in **Chapter 3** and **Chapter 4**, respectively. Inspired by self-assembled monolayers (SAMs) of organosulfur molecules on the Au substrate, m-RGO sheets may be easily deposited on Au substrate because of the presence of high density of thiols on the graphene matrix.

Self-assembled monolayers (SAMs) typically refer to the spontaneous formation of nanometer-sized mono-molecular thin film by chemisorption and self-organization on the surface of appropriate substrates.[179] Each molecule that composes the building blocks of the SAMs on a substrate can be divided into three different parts, namely: 1) the head group (linking group), 2) the backbone (main chain), and 3) the specific terminal group (active group). The head group provides self-assembly process on the surface of the substrate. The interactions among

backbone hydrocarbon chains make an efficient packing of the monolayer and stabilize the structures with increasing chain length due to increasing intermolecular forces. The terminal group determines specific properties of the surface and could also be used to anchor additional molecules by van der Waals interactions or covalent bonds.[180]

Ever since Nuzzo and Allara discovered the preparation and characterization of SAMs on gold at the beginning of the 1980s,[181] thiols and dithiols on gold have been extensively studied with various existing surface science techniques. Among various organic molecules for SAMs on gold substrate, long-chain n-alkanethiols[182] and their substituted analogues[183] have been the most widely investigated. In all cases, removing organic residue adsorbed on the surfaces is required to self-assemble the thiol monolayer. Changing the functional group of the other end in n-alkanethiols could be enough to alter the physical and chemical properties of the layers. Dithiols can be regarded as thiol-terminated n-alkanethiols, and are very important to bind metallic ions and nanoparticles to the SAMs.[184] As a result of the intensive research of SAMs, it in turn is found to have plenty of applications such as in nanofabrication,[185] nanoelectronics,[186] biological screening,[187] and analytical chemistry.[188] Other important application of SAMs is in the field of material protection, where they are used as thin film for corrosion prevention.[189] Especially, thiol SAMs also have been used to synthesize gold nanoparticles; it stabilizes the nanostructures against aggregation[190] and controls the cluster size by changing the hydrocarbon chain length.[191]

With regard to the stability of thiol SAMs on gold against oxidation and thermal desorption of sulfur head group organic molecules adsorbed on gold surfaces, this is an important issue with practical applications. Therefore, improvement of the oxidation resistance of thiol SAMs becomes crucial for their use

in ambient conditions. The poor thermal stability of SAMs, which are stable only up to 70 °C, provides some restrictions to their applications.[182] The poor thermal stability of thiol SAMs could be ascribed that Au–S chemical bond (a thiolate bond, 50 kcal/mol)[137] is not strong enough to stand higher than 70 °C. Recently, penta-corannulene (*tert*-butylthio or 4-dimethylaminophenylthio) chemisorbed on gold substrate was reported.[192] These organic molecules on gold substrate remain bound to the surface through Au–S bonds even higher than 167 °C. This work implies that a molecule that has more thiol functional group can improve the thermal stability of SAMs on Au. Although the thermal stability of SAMs on Au was improved, it still provides limited application due to poor electrical conductivity. Therefore, it is urgent to fabricate good electrically conductive SAMs on Au.

Since graphene was successfully isolated from graphite in 2004, the graphene has been intensively investigated because of extraordinary electrical properties.[5] Much research has been carried out to understand the nature of graphene at the beginning. These days, however, more research has been focused on modifying the surface of graphene in order to alter the physical and chemical properties.[193] Among various methods,[194] graphene oxide (GO) produced by solution process is the most popular for modifying the surface of graphene due to the presence of various oxygen functional groups. In **Chapter 4**, modification of the surface of graphene oxides utilizing a Berzelious reagent (P_4S_{10}) *via* solvothermal reaction route was shown to produce thiol-functionalized reduced graphene oxides (mercapto reduced graphene oxides (m-RGOs)). Herein, the deposition of m-RGOs on Au electrode in the same fashion of self-assembled monolayers (SAMs) of n-alkanethiol on Au electrode is reported in this study for the first time. The mercapto reduced graphene oxides (m-RGOs) chemisorbed on Au electrode may show a good thermal stability due to the presence of multiple thiols on the basal plane of graphene matrix.

6.2 Experimental Section

6.2.1 Synthesis of Graphene Oxides (GOs)

GOs were synthesized through a modified Hummers method by oxidation of natural graphite flake with strong oxidants.[34] In a typical procedure, 1 g of natural graphite flake (Sigma-Aldrich) was ground with 5 g of NaCl (Alfa Aesar, 99+%) until the mixture becomes homogeneous by visual inspection. NaCl from the mixture was then washed away using deionized water with vacuum filtration. The ground graphite on the filter paper was dried at 110 °C in a lab oven for 2 h to remove all physisorbed water in the ground graphite. 0.765 g of $NaNO_3$ (Sigma-Aldrich, ≥ 99.0%) was first dissolved in 40 mL of concentrated H_2SO_4 (Sigma-Aldrich, ACS reagent, 95 ~ 98%) in a 400 mL of beaker with stirring for 20 minutes. About 1 g of the dried ground graphite was then added to the beaker with keep stirring. Subsequently, the beaker was placed in an ice bath and then 5 g of $KMnO_4$ (Sigma-Aldrich, ≥ 99.0%) was slowly added to the beaker while the temperature was kept below 10 °C. Afterward, the beaker was removed from the ice bath. The mixture in the beaker was then heated around 40 °C with vigorously stirring until it became pink thick paste. 100 mL of deionized water was added to the beaker and then 20 mL of H_2O_2 (Alfa Aesar, ACS reagent, 29 ~ 32%) was slow added to the suspension subsequently to finish the reaction. After the reaction, the color of the suspension became bright yellow. The suspension was then repeatedly centrifuged and the precipitate was washed with diluted HCl until $BaCl_2$ (Anhydrous purified, J.T. Baker chemical Co.) test shows a negative result.

6.2.2 Synthesis of Mercapto Reduced Graphene Oxides (m-RGOs)

The purified GOs in water (pH ~ 4) were mixed with 1 *M* NaOH aqueous solution to obtain agglomerated GOs. The agglomerated GOs in water was

centrifuged at 4000 rpm for 3 minutes and then decanted to remove clear supernatant solution. This was repeated until the pH of the supernatant solution reached around 9. The pH adjusted GOs sludge was rinsed with around 100 mL of pyridine with vacuum filtration to wash away physisorbed water in GOs sludge. The pyridine rinsed GOs sludge was transferred to a fresh pyridine and sonicated for 20 minutes to obtain exfoliated GOs in the pyridine for the sulfidation reaction. For the synthesis of m-RGOs *via* solvothermal reaction route, phosphorus decasulfide (P_4S_{10}, Sigma-Aldrich, 99%) has been used as a thionating reagent. To get control over the amount of sulfur incorporation in graphitic network, the amount of the phosphorus decasulfide (P_4S_{10}, sulfur precursor) as well as the reaction temperature were varied. Hereafter, all m-RGOs samples, unless otherwise stated, were synthesized by using 10% excess with respect to stoichiometric amount of P_4S_{10}. In a typical solvothermal reaction, 220 mg of P_4S_{10} (10% excess with respect to stoichiometric amount of P_4S_{10}) was added to 200 mg of GOs in 13 mL of pyridine in a Teflon-lined autoclave of capacity of 23 mL. It was then placed in an oven pre-heated at 120, 150 and 180 °C for 15 hours. After the reaction, the solid product was collected *via* vacuum filtration and it was washed several times with deionized water and ethanol to remove all the unreacted P_4S_{10} and by products. The mercapto reduced graphene oxides (m-RGOs) in water were freeze-dried for further characterization. This final product could be easily dispersed in various solvents such as H_2O, DMF, DMSO, and NMP etc. by sonication for 30 minutes to achieve the stable dispersion of mostly single or bi-layer m-RGO in wide range of solvent media.

6.2.3 Depositions of m-RGOs on Au Substrate

The as-synthesized m-RGOs was dispersed in absolute ethanol by sonication for about 30 minutes and then the m-RGOs dispersion was centrifuged at 6000 rpm

for 10 minutes to remove unexfoliated m-RGOs. After the centrifugation, the only supernatant solution was carefully transferred to eppendorf tube for further experiment. The purchased Au film (Agilent Technology) that forms with (111) orientation on the (001) cleavage planes of mica was used for all experiments. The Au substrate was annealed using H_2 flame for about 30 seconds to remove organic residue adsorbed on the surface of the Au and increase (111) domain size of the Au right before the uses. The annealed Au substrate was immersed in the eppendorf tube that is filled with m-RGOs dispersion 50% full. Subsequently, the eppendorf tube was placed in a pre-heated dry oven at 60 °C and incubated for 10 hours. After the incubation, the Au substrate was taken out and rinsed with absolute ethanol thoroughly to remove m-RGOs unbound to Au substrate and dried at ambient condition for further characterization.

6.2.4 Materials Characterization

X-ray photoelectron spectroscopic (XPS) measurements were carried out using a VG-220IXL spectrometer with a monochromated Al Kα radiation (1486.6 eV, line width 0.8 eV). The pressure in the analysis chamber was about 10^{-9} torr while recording the spectra. The spectrometer has an energy resolution of 0.4 eV. All the binding energies were corrected with reference to C1s at 284.6 eV. Deconvolution of the spectrum was done using the CASA software with the accuracy of 0.2 eV. Shirley background was used for the deconvolution. For the high-resolution C1s XPS spectrum was deconvoluted into the following three components: C–C (sp^2- and sp^3-hybridized peaks at 284.7 and 285.4 eV, respectively),[37] C=O (carbonyl peak at 287.6 eV),[173] and C–O (hydroxyl peak at 286.5 eV).[104] Carbon atoms with the C–S bond were not separately treated because the C1s binding energy of C–S (285.3 eV)[105] is too close to that of C–C (sp^3-hybridization) and thus could not be resolved,

given the resolution of the XPS instrument (0.4 eV). The high-resolution O1s XPS spectrum was presented with the following oxygen functional groups: C=O (531.7 eV)[106, 149] and C–OH (533 eV).[60a] The high-resolution S2p XPS spectrum was deconvoluted with thiol ($S2p_{3/2}$ at 164.0 eV with FWHM of 1.2 eV; $S2p_{1/2}$ at 165.2 eV with FWHM of 1.2 eV).[108] The area ratio and splitting energy difference between $S2p_{3/2}$ and $S2p_{1/2}$ spin-orbit doublet peaks were 2:1 and 1.2 eV, respectively.

Surface topography images were obtained using atomic force microscope (AFM) (Pico-Plus AFM, Molecular imaging, Agilent technologies). All AFM studies were performed in air using a tapping mode with SCANASYST-AIR tips (Bruker). Electrochemical measurements were implemented with a CHI760C electrochemical analyzer in 1 M KCl in a three-electrode cell. Platinum wire was used as a counter electrode and saturated calomel electrode (SCE) was used for the reference electrode. The scan rate was 100 mV/s.

The Nano-Secondary Ion Mass Spectrometry (NanoSIMS) measurements were done using a Cs^+ primary ion beam with the Cameca Ametek NanoSIMS50L at Arizona State University. The beam current at the sample was lowered to ~0.48 pA by choosing a small diaphragm to get much desired fine beam and high enough count rates for imaging of the sample. Negative secondary ions of ^{12}C, ^{16}O,and ^{32}S were measured simultaneously using electron multipliers in the multicollection mode. Sufficient mass resolving power (MRP) to separate out mass interferences, e.g., ^{32}S from $^{31}P^1H$ (MRP > 4000), was maintained by choosing an appropriate entrance slit. Typical measurement condition varied from 10×10 μm^2 to 25×25 μm^2 analysis areas. Each area was divided into 256^2 pixels with dwell times of 40 msec/pixel. The ion images from multiple layers were corrected for beam drifts using the WinImage software and the last 8-12 layers were added to form summed ion images.

6.3 Results and Discussions

General schematic illustration of deposition of m-RGOs on Au substrate is shown in **Figure 48**. The annealed with H_2-flame gold substrate was immersed in an eppendorf tube that is filled with m-RGOs dispersion in absolute ethanol 50% full. Subsequently, the eppendorf tube was placed in a pre-heated dry oven at 60 °C and incubated for 10 hours. During incubation, m-RGOs will spontaneously bind to the surface of the gold substrate by a strong gold-sulfur interaction. Elevated temperature could facilitate the formation of Au–S bond.[180a] After the incubation, the Au substrate was taken out from the eppendorf tube and rinsed it with absolute ethanol thoroughly and dried at ambient condition to obtain m-RGO sheets deposited on the surface of Au substrate.

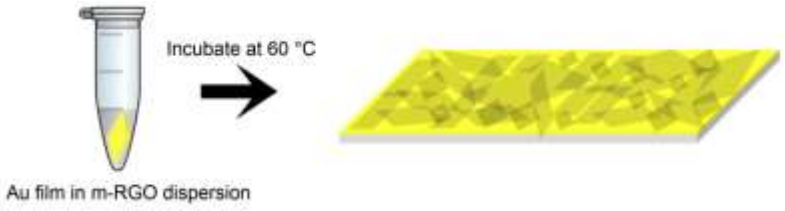

Figure 48. Schematic illustration of deposition of m-RGOs on gold substrate.

The elemental analysis of the as-synthesized m-RGOs was carried out with X-ray photoelectron spectroscopy (XPS) and the XPS spectra of m-RGOs were represented in **Figure 49**. According to the XPS wide scan of m-RGOs depicted in **Figure 49(a)**, the XPS spectrum of m-RGOs only shows carbon, oxygen, and sulfur elements, which indicates all unreacted P_4S_{10} and by-products were completely removed and the C:O:S atomic ratio is around 13:1:0.9. The high-resolution XPS C1s spectrum shown in **Figure 49(b)** indicates that m-RGOs were reduced during the synthesis and sp^2-hybridized carbon species were significantly restored. Many oxygen functional groups are also removed during the reaction in comparison with the high-resolution XPS C1s spectrum of GOs although not shown here. The high-

resolution XPS O1s spectrum of the m-RGOs represented in **Figure 49(c)** indicates that hydroxyl and carbonyl functional groups are only left on the m-RGOs, which is consistent with the high-resolution XPS C1s spectrum shown in **Figure 49(b)**. **Figure 49(d)** shows the high-resolution XPS S2p spectrum of m-RGOs and the spectrum reveals that all sulfur functional groups are thiol in m-RGOs. In the **Figure 49(d)**, the large FWHM XPS S2p spectrum is deconvoluted into two peaks, $S2p_{2/3}$ and $S2p_{1/2}$, due to the spin-orbit coupling. The splitting energy between deconvoluted $S2p_{2/3}$ peak and $S2p_{1/2}$ peak is 1.2 eV and the area ratio is 2:1.

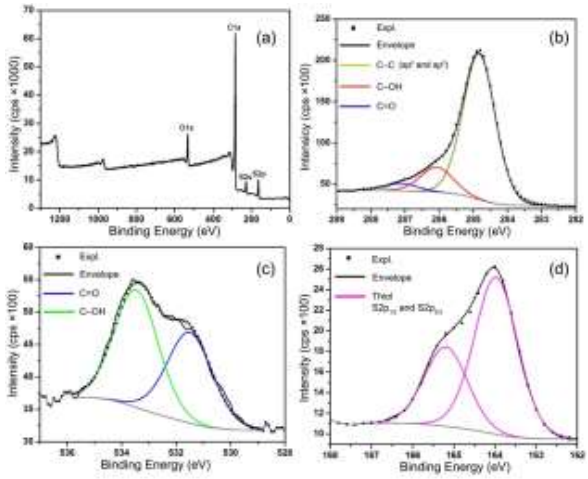

Figure 49. XPS spectra of m-RGO: (a) wide scan, (b) high-resolution C1s, (c) high-resolution O1s, and (d) high-resolution S2p.

Atomic force microscope (AFM) images of (111) fresh gold surface and m-RGOs deposited on the gold surface are shown in **Figure 50** and **Figure 51**, respectively. The entire surface of the Au substrate is not atomically flat but the surface of each (111) Au island is flat. After the deposition of m-RGOs on the Au substrate, the whole surface of the Au is covered by m-RGO sheets and the average size of each sheet is around 60 nm. The m-RGO sheets deposited on the surface of Au are well distributed. According to the previous report, thermal desorption of n-

alkanethiol bound to the surface of gold occurs around 70 °C[182] but thermal desorption of m-RGOs during incubation process could not happen on the gold substrate. This result may imply that each m-RGO sheet comprises multiple thiol functional groups, which provides stronger binding between m-RGO sheets and the surface of the gold. This result is consistent with a recent work.[192] Interestingly, although the m-RGOs dispersion in ethanol contains a lot of large sheets (~ 1 μm) only small sized m-RGO sheets (~ 60 nm) are deposited on the surface of the gold and there are no larger sized m-RGO sheets (larger than 100 nm) observed on the surface of Au. This result may imply that larger sized m-RGO sheets may have higher kinetic momentum than that of small sized m-RGO sheets. Thus, larger sized m-RGO sheets could rebind from the surface of the gold. The small sized m-RGOs sheets, however, may have lower kinetic momentum and those may well bind to the surface of the Au.

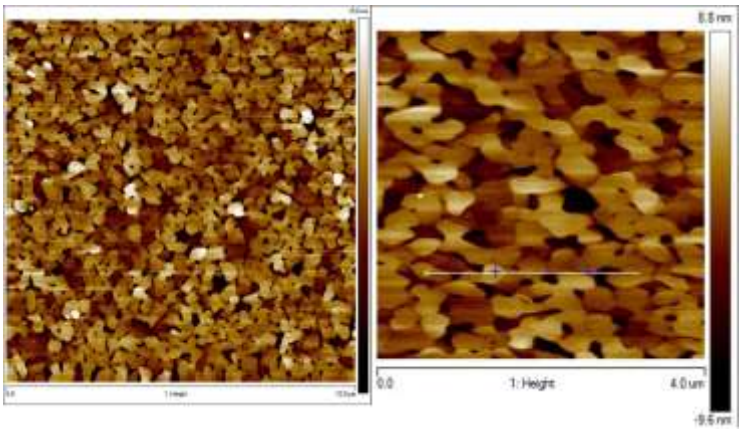

Figure 50. AFM images of bare gold: 10×10 μm^2 scanned area (top left) and 4×4 μm^2 scanned area (top right).

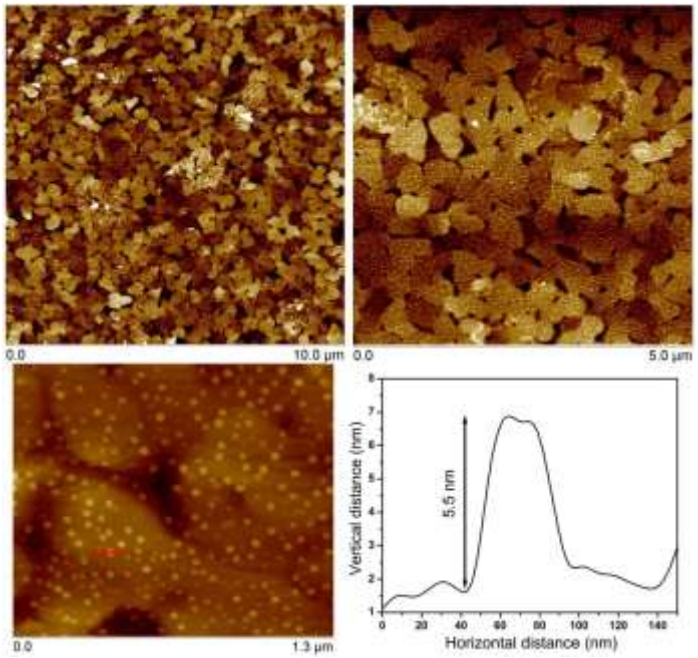

Figure 51. AFM images of m-RGO deposited on gold: 10×10 μm^2 scanned area (top left), 5×5 μm^2 scanned area (top right), 1.3×1.1 μm^2 scanned area (bottom left) and corresponding height profile of the 1.3×1.1 μm^2 scanned area (bottom right).

The NanoSIMS was carried out to investigate the distribution of carbon, oxygen, and sulfur on the m-RGO sheets deposited on Au substrate and compare with bare Au substrate. NanoSIMS is a new generation double-focusing mass spectrometer,[178] which is characterized by high spatial resolution (up to 50 nm using the Cs^+ primary beam and ~200 nm with the O^- beam) necessary to study the m-RGO sheets deposited on the Au substrate in this study. The carbon, oxygen, and sulfur ion images as well as secondary electron images of bare Au are shown in **Figure 52**. Although carbon and oxygen ions were detected from bare gold substrate, sulfur ion was not detected at all. Carbon and oxygen ions may come from hydrocarbons or organic molecules adsorbed on the surface of Au substrate. A couple of big islands from the secondary electron image shown in **Figure 52** may be aggregated gold clusters generated during H_2-flame annealing process. In order to

obtain carbon, oxygen, and sulfur ions images of m-RGOs deposited on the Au substrate, the sputtered 5 nm thick carbon film was coated on top of the m-RGO sheets deposited on the Au substrate to protect very thin m-RGO sheets during pre-sputtering process. The last 5-8 layers were added to form summed ion images shown in **Figure 53**. The summed up images depicted in **Figure 53** clearly shows the distribution of oxygen and sulfur functional groups on the surface of the m-RGOs sheets deposited on the Au substrate, which is consistent with the AFM results. The size of m-RGO sheets deposited on the Au substrate is very similar to the spatial resolution limit of NaonoSIMS thus the NanoSIMS may not resolve the m-RGO sheets. The relatively big islands on the Au substrate shown in **Figure 53** may be gold cluster produced during H_2-flame annealing process. The edge of oxygen ion image is brighter than center area, which may be due to the beam damage.

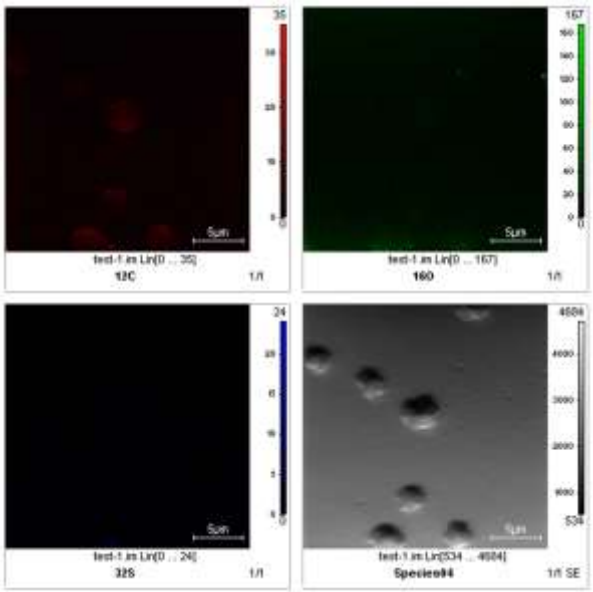

Figure 52. Ion images of $^{12}C^-$, $^{16}O^-$, and $^{32}S^-$ as well as secondary electron image of a 25x25 um^2 area on bare Au substrate using Nano-Secondary Ion Mass Spectrometry (NanoSIMS).

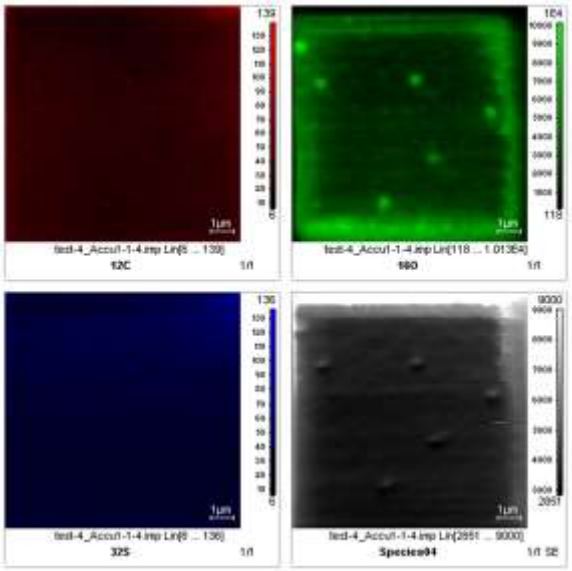

Figure 53. Ion images of $^{12}C^-$, $^{16}O^-$, and $^{32}S^-$ as well as secondary electron image of a 10x10 um^2 area on m-RGOs deposited on Au substrate using Nano-Secondary Ion Mass Spectrometry (NanoSIMS).

6.4 Concluding Remarks

It has been well demonstrated that as-synthesized m-RGOs were successfully deposited on the gold electrode in the same manner of self-assembled monolayers (SAMs) of n-alkanethiol on Au electrode after incubation at 60 °C. During the incubation, small sized m-RGO sheets were bound to the surface of Au electrode without thermal desorption of m-RGO sheets from the surface of Au electrode. This result may imply that thermal stability of m-RGOs deposited on gold could be better than SAMs of n-alkanethiol on gold due to the presence of multiple thiol functional groups on m-RGO sheet. The atomic force microscope (AFM) images show that the nano-sized mercapto reduced graphene oxide sheets are well distributed on the surface of the gold electrode and the entire surface of the gold is covered by m-RGO sheets. Additionally, oxygen and sulfur functional groups are homogeneously

distributed on the surface of the Au electrode. This result may expand the field in SAMs on gold with organosulfur molecules.

CHAPTER 7

CONCLUSIONS

It has been successfully demonstrated that the synthesis and characterization of thionated reduced graphene oxides (mercapto reduced graphene oxides (m-RGOs)) and their thin films. The two methods for the synthesis of m-RGOs and characterizations are presented in **Chapter 3** and **Chapter 4**. In **Chapter 3**, the synthesis of m-RGOs through solid-gas metathetical sulfidation reaction as well as characterization of m-RGOs were shown. In **Chapter 4**, the synthesis of m-RGOs through solvothermal reaction route using a Berzelius reagent and characterization of m-RGOs were described. Additionally, the fabrication and characterizations of m-RGOs Langmuir Blodgett (LB) film and the deposition and characterizations of m-RGOs sheets on Au electrode were elaborated in **Chapter 5** and **Chapter 6**, respectively.

The C:O:S atomic ratios of m-RGOs synthesized *via* solid-gas metathetical sulfidation reaction route are around 20:1:2.2 and the atomic ratios could be controlled by changing the reaction temperature. As-synthesized m-RGOs show a good dispersibility in both water and various polar organic solvents such as ethanol, dimethylformamide (DMF), acetone, and propylene carbonate (PC). The mercapto reduced graphene oxides contain thiol functional group as a dominant sulfur functional group and most of the thiol functional groups are chemically reactive to form disulfides. Additionally, Tauc energy gap, which is also referred to optical band gap, of m-RGO is 0.03 eV. Much lower Tauc energy gap of m-RGOs could be ascribed to the restoration of sp^2-hybridized carbon species as well as overlapping sulfur 3p and 3s orbitals with π-orbitals in graphene sheets.

The mercapto reduced graphene oxides (m-RGOs) synthesized *via* solvothermal reaction route utilizing a Berzelius reagent (P_4S_{10}) show that thiol

functional group is a majority among various sulfur functional groups in m-RGOs and the C:O:S atomic ratios are about 13:1:1. As-synthesized m-RGOs are highly reduced and the m-RGOs are not re-stacked together during the synthesis. The atomic ratios of m-RGOs could be also controlled by the reaction temperature. The attenuated total reflectance-Fourier transform infrared (ATR-FTIR) spectrum shows that sulfur functional groups directly attach to the carbon on graphene sheets. According to scanned transmission electron microscope (STEM) elemental mapping image, the oxygen and sulfur functional groups are homogeneously distributed on the graphene matrix.

The mercapto reduced graphene oxides (m-RGOs) Langmuir-Blodgett (LB) film and deposition of m-RGOs on Au electrode were successfully fabricated using m-RGOs dispersed in absolute ethanol. The mercapto reduced graphene oxides Langmuir film on top of the water surface in a container could be easily transferred to various substrates such as glass, mica, or gold. The optical transparency at 550 nm of the m-RGOs LB film is about 92%, which indicates 4 layers of m-RGO sheets deposited on the substrate and the sheet resistance of the m-RGOs LB film is approximately 500 kΩ/sq. With similar optical transparency of m-RGOs LB films, more sulfur functional groups could significantly reduce the sheet resistance of the m-RGOs LB film. The thickness of m-RGOs LB film could be controlled with different concentration of m-RGOs dispersion. The mercapto reduced graphene oxides (m-RGOs) LB film is macroscopically homogeneous on substrates.

The deposition of m-RGOs on Au electrode was performed in the same fashion of self-assembled monolayers (SAMs) of organosulfur molecules. The deposited m-RGO sheets on Au electrode are well distributed and the size of m-RGO sheets is around 60 nm. During the incubation process at 60 °C, thermal desorption of m-RGO sheets from the surface of Au electrode was not observed. The result may

indicate that larger sheets have higher kinetic momentum thus all larger sheets (> 100 nm) are rebound from the surface of Au electrode. Therefore, only small sized m-RGO sheets that have lower kinetic momentum well bind to the surface of Au electrode. The thermal stability of m-RGOs on Au electrode could be better than that of SAMs of n-alkanethiols on Au electrode because each m-RGO sheet may contain multiple thiol functional groups. The homogeneous distribution of oxygen and sulfur functional groups on the surface of Au electrode was shown from NanoSIMS $^{16}O^-$ and $^{32}S^-$ ion images.

The two developed methods to produce m-RGOs may apply to any kind of carbonaceous materials or polymers those contain oxygen functional groups to generate thiol-functionalized carbonaceous materials or thiol-functionalized polymers. The new derivative graphene, mercapto reduced graphene oxides (m-RGOs), may expand the graphene chemistry. The as-synthesized m-RGOs may be applied to bio-chemistry or polymer chemistry to conjugate between m-RGOs and biomolecules or polymers by using thiol functional group as a cross-linker as well as the m-RGOs could make new graphene-metal composites based on thiol-metal bond. Moreover, the m-RGOs may be applied to water purification application because thiol functional groups show a good affinity with heavy metals. The new facile fabrication method developed may facilitate utilizing graphene film for various applications.

REFERENCES

1. Geim, A. K.; Novoselov, K. S., *Nat. Mater.* **2007**, *6,* 183.

2. (a) Slonczewski, J.; Weiss, P., *Phys. Rev.* **1958**, *109,* 272. (b) Wallace, P., *Phys. Rev.* **1947**, *71,* 622. (c) McClure, J., *Phys. Rev.* **1956**, *104,* 666.

3. Fradkin, E., *Phys. Rev. B* **1986**, *33,* 3263.

4. Mermin, N. D., *Phys. Rev.* **1968**, *176,* 250.

5. Novoselov, K.; Geim, A.; Morozov, S.; Jiang, D.; Zhang, Y.; Dubonos, S.; Grigorieva, I.; Firsov, A., *Science* **2004**, *306,* 666.

6. (a) Berger, C.; Song, Z.; Li, T.; Li, X.; Ogbazghi, A. Y.; Feng, R.; Dai, Z.; Marchenkov, A. N.; Conrad, E. H.; First, P. N., *J. Phys. Chem. B* **2004**, *108,* 19912. (b) Berger, C.; Song, Z.; Li, X.; Wu, X.; Brown, N.; Naud, C.; Mayou, D.; Li, T.; Hass, J.; Marchenkov, A. N., *Science* **2006**, *312,* 1191.

7. (a) Bunch, J. S.; Van der Zande, A. M.; Verbridge, S. S.; Frank, I. W.; Tanenbaum, D. M.; Parpia, J. M.; Craighead, H. G.; McEuen, P. L., *Science* **2007**, *315,* 490. (b) Bunch, J. S.; Verbridge, S. S.; Alden, J. S.; van der Zande, A. M.; Parpia, J. M.; Craighead, H. G.; McEuen, P. L., *Nano Lett.* **2008**, *8,* 2458. (c) Meyer, J. C.; Geim, A.; Katsnelson, M.; Novoselov, K.; Booth, T.; Roth, S., *Nature* **2007**, *446,* 60.

8. (a) Ghosh, S.; Calizo, I.; Teweldebrhan, D.; Pokatilov, E.; Nika, D.; Balandin, A.; Bao, W.; Miao, F.; Lau, C. N., *Appl. Phys. Lett.* **2008**, *92,* 151911. (b) Balandin, A. A.; Ghosh, S.; Bao, W.; Calizo, I.; Teweldebrhan, D.; Miao, F.; Lau, C. N., *Nano Lett.* **2008**, *8,* 902.

9. (a) Novoselov, K.; McCann, E.; Morozov, S.; Fal'ko, V. I.; Katsnelson, M.; Zeitler, U.; Jiang, D.; Schedin, F.; Geim, A., *Nat. Phys.* **2006**, *2,* 177. (b) Novoselov, K. S.; Jiang, Z.; Zhang, Y.; Morozov, S.; Stormer, H.; Zeitler, U.; Maan, J.; Boebinger, G.; Kim, P.; Geim, A., *Science* **2007**, *315,* 1379.

10. Zhang, Y.; Tan, Y.-W.; Stormer, H. L.; Kim, P., *Nature* **2005**, *438,* 201.

11. Huang, M.; Pascal, T. A.; Kim, H.; Goddard III, W. A.; Greer, J. R., *Nano Lett.* **2011**, *11,* 1241.

12. Rao, C. e. N. e. R.; Sood, A. e. K.; Subrahmanyam, K. e. S.; Govindaraj, A., *Angew. Chem. Int. Ed.* **2009**, *48,* 7752.

13. Nair, R.; Blake, P.; Grigorenko, A.; Novoselov, K.; Booth, T.; Stauber, T.; Peres, N.; Geim, A., *Science* **2008**, *320,* 1308.

14. Bai, J.; Cheng, R.; Xiu, F.; Liao, L.; Wang, M.; Shailos, A.; Wang, K. L.; Huang, Y.; Duan, X., *Nat. Nanotehnol.* **2010**, *5,* 655.

15. Miller, J. R.; Outlaw, R.; Holloway, B., *Science* **2010**, *329,* 1637.

16. (a) Brownson, D. A.; Kampouris, D. K.; Banks, C. E., *J. Power Sources* **2011**, *196,* 4873. (b) Pumera, M., *Energy Environ. Sci.* **2011**, *4,* 668.

17. (a) Yoon, H. J.; Jun, D. H.; Yang, J. H.; Zhou, Z.; Yang, S. S.; Cheng, M. M.-C., *Sensors and Actuators B: Chemical* **2011**, *157,* 310. (b) Ang, P. K.; Chen, W.; Wee, A. T. S.; Loh, K. P., *J. Am. Chem. Soc.* **2008**, *130,* 14392. (c) Fowler, J. D.; Allen, M. J.; Tung, V. C.; Yang, Y.; Kaner, R. B.; Weiller, B. H., *ACS nano* **2009**, *3,* 301.

18. (a) Li, X.; Zhu, Y.; Cai, W.; Borysiak, M.; Han, B.; Chen, D.; Piner, R. D.; Colombo, L.; Ruoff, R. S., *Nano Lett.* **2009**, *9,* 4359. (b) Wang, X.; Zhi, L.; Müllen, K., *Nano Lett.* **2008**, *8,* 323.

19. (a) Zhao, G.; Li, J.; Ren, X.; Chen, C.; Wang, X., *Envion. Sci. Technol.* **2011**, *45,* 10454. (b) Chandra, V.; Park, J.; Chun, Y.; Lee, J. W.; Hwang, I.-C.; Kim, K. S., *ACS nano* **2010**, *4,* 3979.

20. (a) Mao, Y.; Bao, Y.; Gan, S.; Li, F.; Niu, L., *Biosensors and Bioelectronics* **2011**, *28,* 291. (b) Li, J.; Guo, S.; Zhai, Y.; Wang, E., *Analytica Chimica Acta* **2009**, *649,* 196.

21. (a) Wu, Z.-S.; Ren, W.; Wen, L.; Gao, L.; Zhao, J.; Chen, Z.; Zhou, G.; Li, F.; Cheng, H.-M., *ACS nano* **2010**, *4,* 3187. (b) Zhou, G.; Wang, D.-W.; Li, F.;

Zhang, L.; Li, N.; Wu, Z.-S.; Wen, L.; Lu, G. Q.; Cheng, H.-M., *Chem. Mater.* **2010**, *22,* 5306.

22. (a) Wang, Y.; Li, Z.; Wang, J.; Li, J.; Lin, Y., *Trends in Biotechnology* **2011**, *29,* 205. (b) Tang, Z.; Wu, H.; Cort, J. R.; Buchko, G. W.; Zhang, Y.; Shao, Y.; Aksay, I. A.; Liu, J.; Lin, Y., *Small* **2010**, *6,* 1205.

23. (a) Liu, F.; Choi, J. Y.; Seo, T. S., *Biosensors and Bioelectronics* **2010**, *25,* 2361. (b) Li, F.; Huang, Y.; Yang, Q.; Zhong, Z.; Li, D.; Wang, L.; Song, S.; Fan, C., *Nanoscale* **2010**, *2,* 1021.

24. Liu, Q.; Liu, Z.; Zhang, X.; Zhang, N.; Yang, L.; Yin, S.; Chen, Y., *Appl. Phys. Lett.* **2008**, *92,* 223303.

25. Bae, S.; Kim, H.; Lee, Y.; Xu, X.; Park, J.-S.; Zheng, Y.; Balakrishnan, J.; Lei, T.; Kim, H. R.; Song, Y. I., *Nat. Nanotehnol.* **2010**, *5,* 574.

26. (a) Wassei, J. K.; Kaner, R. B., *Materials Today* **2010**, *13,* 52. (b) Jo, G.; Choe, M.; Lee, S.; Park, W.; Kahng, Y. H.; Lee, T., *Nanotechnology* **2012**, *23,* 112001.

27. Hass, J.; De Heer, W.; Conrad, E., *Journal of Physics: Condensed Matter* **2008**, *20,* 323202.

28. (a) Stankovich, S.; Dikin, D. A.; Dommett, G. H. B.; Kohlhaas, K. M.; Zimney, E. J.; Stach, E. A.; Piner, R. D.; Nguyen, S. B. T.; Ruoff, R. S., *Nature* **2006**, *442,* 282. (b) Stankovich, S.; Piner, R. D.; Chen, X.; Wu, N.; Nguyen, S. B. T.; Ruoff, R. S., *J. Mater. Chem.* **2006**, *16,* 155. (c) Stankovich, S.; Dikin, D. A.; Piner, R. D.; Kohlhaas, K. A.; Kleinhammes, A.; Jia, Y.; Wu, Y.; Nguyen, S. B. T.; Ruoff, R. S., *Carbon* **2007**, *45,* 1558. (d) Li, D.; Muller, M. B.; Gilje, S.; Kaner, R. B.; Wallace, G. G., *Nat. Nanotehnol.* **2008**, *3,* 101. (e) Hernandez, Y.; Nicolosi, V.; Lotya, M.; Blighe, F. M.; Sun, Z.; De, S.; McGovern, I.; Holland, B.; Byrne, M.; Gun'Ko, Y. K., *Nat. Nanotechnol.* **2008**, *3,* 563.

29. Gilje, S.; Han, S.; Wang, M.; Wang, K. L.; Kaner, R. B., *Nano Lett.* **2007**, *7,* 3394.

30. (a) Lu, X.; Yu, M.; Huang, H.; Ruoff, R. S., *Nanotechnology* **1999**, *10,* 269. (b) Zhang, Y.; Small, J. P.; Pontius, W. V.; Kim, P., *Appl. Phys. Lett.* **2005**, *86,* 073104.

31. (a) Paredes, J.; Villar-Rodil, S.; Martinez-Alonso, A.; Tascon, J., *Langmuir* **2008**, *24,* 10560. (b) Zhu, Y.; Murali, S.; Cai, W.; Li, X.; Suk, J. W.; Potts, J. R.; Ruoff, R. S., *Adv. Mater.* **2010**, *22,* 3906.

32. Brodie, B., *Ann. Chim. Phys* **1860**, *59,* 466.

33. Staudenmaier, L., *Berichte der deutschen chemischen Gesellschaft* **1898**, *31,* 1481.

34. Hummers, W. S., Jr.; Offeman, R. E., *J. Am. Chem. Soc.* **1958**, *80,* 1339.

35. Lerf, A.; He, H.; Riedl, T.; Forster, M.; Klinowski, J., *Solid State Ionics* **1997**, *101,* 857.

36. Wang, G.; Yang, J.; Park, J.; Gou, X.; Wang, B.; Liu, H.; Yao, J., *J. Phys. Chem. C* **2008**, *112,* 8192.

37. Shin, H.-J.; Kim, K. K.; Benayad, A.; Yoon, S.-M.; Park, H. K.; Jung, I.-S.; Jin, M. H.; Jeong, H.-K.; Kim, J. M.; Choi, J.-Y.; Lee, Y. H., *Adv. Funct. Mater.* **2009**, *19,* 1987.

38. Zhang, J.; Yang, H.; Shen, G.; Cheng, P.; Zhang, J.; Guo, S., *Chemical Communications* **2010**, *46,* 1112.

39. (a) McAllister, M. J.; Li, J. L.; Adamson, D. H.; Schniepp, H. C.; Abdala, A. A.; Liu, J.; Herrera-Alonso, M.; Milius, D. L.; Car, R.; Prud'homme, R. K., *Chem. Mater.* **2007**, *19,* 4396. (b) Schniepp, H. C.; Li, J. L.; McAllister, M. J.; Sai, H.; Herrera-Alonso, M.; Adamson, D. H.; Prud'homme, R. K.; Car, R.; Saville, D. A.; Aksay, I. A., *J. Phys. Chem. B* **2006**, *110,* 8535.

40. Kudin, K. N.; Ozbas, B.; Schniepp, H. C.; Prud'Homme, R. K.; Aksay, I. A.; Car, R., *Nano Lett.* **2008**, *8,* 36.

41. Potts, J. R.; Dreyer, D. R.; Bielawski, C. W.; Ruoff, R. S., *Polymer* **2011**, *52,* 5.

42. Arsat, R.; Breedon, M.; Shafiei, M.; Spizziri, P.; Gilje, S.; Kaner, R.; Kalantar-zadeh, K.; Wlodarski, W., *Chem. Phys. Lett.* **2009**, *467,* 344.

43. Miller, J. R.; Outlaw, R.; Holloway, B., *Electrochimica Acta* **2011**, *56,* 10443.

44. (a) Eizenberg, M.; Blakely, J., *Surface Science* **1979**, *82,* 228. (b) Shelton, J.; Patil, H.; Blakely, J., *Surface Science* **1974**, *43,* 493. (c) Eizenberg, M.; Blakely, J., *J. Chem. Phys.* **1979**, *71,* 3467.

45. Bauer, A.; Kräußlich, J.; Dressler, L.; Kuschnerus, P.; Wolf, J.; Goetz, K.; Käckell, P.; Furthmüller, J.; Bechstedt, F., *Phys. Rev. B* **1998**, *57,* 2647.

46. De Heer, W. A.; Berger, C.; Wu, X.; First, P. N.; Conrad, E. H.; Li, X.; Li, T.; Sprinkle, M.; Hass, J.; Sadowski, M. L., *Solid State Communications* **2007**, *143,* 92.

47. Emtsev, K. V.; Bostwick, A.; Horn, K.; Jobst, J.; Kellogg, G. L.; Ley, L.; McChesney, J. L.; Ohta, T.; Reshanov, S. A.; Röhrl, J., *Nat. Mater.* **2009**, *8,* 203.

48. (a) Forbeaux, I.; Themlin, J.-M.; Debever, J.-M., *Phys. Rev. B* **1998**, *58,* 16396. (b) Van Bommel, A.; Crombeen, J.; Van Tooren, A., *Surface Science* **1975**, *48,* 463.

49. (a) Tsukamoto, T.; Hirai, M.; Kusaka, M.; Iwami, M.; Ozawa, T.; Nagamura, T.; Nakata, T., *Applied Surface Science* **1997**, *113,* 467. (b) Tsukamoto, T.; Hirai, M.; Kusaka, M.; Iwami, M.; Ozawa, T.; Nagamura, T.; Nakata, T., *Surface Science* **1997**, *371,* 316. (c) Muehlhoff, L.; Choyke, W.; Bozack, M.; Yates, J. T., *Journal of Applied Physics* **1986**, *60,* 2842. (d) Forbeaux, I.; Themlin, J.-M.; Debever, J.-M., *Surface Science* **1999**, *442,* 9.

50. Forbeaux, I.; Themlin, J.-M.; Charrier, A.; Thibaudau, F.; Debever, J.-M., *Applied Surface Science* **2000**, *162,* 406.

51. (a) Reina, A.; Jia, X.; Ho, J.; Nezich, D.; Son, H.; Bulovic, V.; Dresselhaus, M. S.; Kong, J., *Nano Lett.* **2008**, *9,* 30. (b) Kim, K. S.; Zhao, Y.; Jang, H.; Lee, S. Y.; Kim, J. M.; Kim, K. S.; Ahn, J.-H.; Kim, P.; Choi, J.-Y.; Hong, B. H., *Nature* **2009**, *457,* 706.

52. Yu, V.; Whiteway, E.; Maassen, J.; Hilke, M., *Phys. Rev. B* **2011**, *84,* 205407.

53. (a) Lee, S.; Lee, K.; Zhong, Z., *Nano Lett.* **2010**, *10,* 4702. (b) Li, X.; Magnuson, C. W.; Venugopal, A.; An, J.; Suk, J. W.; Han, B.; Borysiak, M.; Cai, W.; Velamakanni, A.; Zhu, Y., *Nano Lett.* **2010**, *10,* 4328. (c) Li, X.; Cai, W.; An, J.; Kim, S.; Nah, J.; Yang, D.; Piner, R.; Velamakanni, A.; Jung, I.; Tutuc, E., *Science* **2009**, *324,* 1312.

54. Yu, Q.; Lian, J.; Siriponglert, S.; Li, H.; Chen, Y. P.; Pei, S.-S., *Appl. Phys. Lett.* **2008**, *93,* 113103.

55. Van der Heide, P. *X-ray Photoelectron Spectroscopy: An Introduction to Principles and Practices;* John Wiley & Sons: 2011.

56. Einstein, A., *Ann. Physic.* **1905**, *322,* 132.

57. Sokolowski, E.; Nordling, C.; Siegbahn, K., *Arkiv Fysik* **1957**, *12*.

58. Siegbahn, K.; Nordling, C.; Fahlman, A., *Nov. Act. Uppsaliensis* **1967**.

59. Drummond, I.; Bryson, R., *Phil. Trans. R. Soc. Lond. A* **1996**, *354,* 2667.

60. (a) Yang, D.; Velamakanni, A.; Bozoklu, G.; Park, S.; Stoller, M.; Piner, R. D.; Stankovich, S.; Jung, I.; Field, D. A.; Ventrice Jr, C. A., *Carbon* **2009**, *47,* 145. (b) Xu, Y. J.; Weinberg, G.; Liu, X.; Timpe, O.; Schlögl, R.; Su, D. S., *Advanced Functional Materials* **2008**, *18,* 3613.

61. (a) Polovina, M.; Babić, B.; Kaluderović, B.; Dekanski, A., *Carbon* **1997**, *35,* 1047. (b) Bai, H.; Li, C.; Shi, G., *Adv. Mater.* **2011**, *23,* 1089.

62. Li, X.; Wang, H.; Robinson, J. T.; Sanchez, H.; Diankov, G.; Dai, H., *J. Am. Chem. Soc.* **2009**, *131,* 15939.

63. Raman, C.; Krishnan, K., *Nature* **1928**, *121,* 501.

64. Ferrari, A. C.; Robertson, J., *Phil. Trans. R. Soc. Lond. A* **2004**, *362,* 2477.

65. Ferrari, A.; Robertson, J., *Phys. Rev. B* **2000**, *61,* 14095.

66. Tuinstra, F.; Koenig, J. L., *J. Chem. Phys.* **1970**, *53,* 1126.

67. Ferrari, A.; Meyer, J.; Scardaci, V.; Casiraghi, C.; Lazzeri, M.; Mauri, F.; Piscanec, S.; Jiang, D.; Novoselov, K.; Roth, S., *Phys. Rev. Lett.* **2006**, *97,* 187401.

68. Guinebretière, R. *X-ray diffraction by polycrystalline materials;* John Wiley & Sons: 2010.

69. Röntgen, W. C., *Ann. Physic.* **1898**, *300,* 1.

70. (a) Schubert, H., *The Monist* **1896**, *6,* 324. (b) Barkla, C. G.; Sadler, C. A., *The London, Edinburgh, and Dublin Philosophical Magazine and Journal of Science* **1908**, *16,* 550.

71. Friedrich, W.; Knipping, P.; Laue, M., *Ann. Physic.* **1913**, *346,* 971.

72. Jenkins, R.; Snyder, R. *Introduction to X-ray powder diffractometry;* John Wiley & Sons: 2012.

73. Azaroff, L. V.; Buerger, M. J., *The powder method in X-ray crystallography*. McGraw-Hill Book Co.: New York, 1953.

74. Manoj, B.; Kunjomana, A., *Int. J. Electrochem. Sci* **2012**, *7,* 3127.

75. Takagi, H.; Maruyama, K.; Yoshizawa, N.; Yamada, Y.; Sato, Y., *Fuel* **2004**, *83,* 2427.

76. Carter, C. B. *Transmission Electron Microscopy: A Textbook for Materials Science. Diffraction. II;* Springer: 1996.

77. Williams, D. B.; Carter, C. B. *The Transmission Electron Microscope;* Springer: 1996.

78. Utsunomiya, S.; Ewing, R. C., *Envion. Sci. Technol.* **2003**, *37,* 786.

79. Block, E. *Reactions of organosulfur compounds;* Academic press New York: 1978.

80. Ozturk, T.; Ertas, E.; Mert, O., *Chem. Rev.* **2010**, *110,* 3419.

81. Kekulé, A., *Justus Liebigs Ann. Chem.* **1854**, *90,* 309.

82. (a) Brinker, C. J.; Scherer, G. W. *Sol-gel science: the physics and chemistry of sol-gel processing;* San Diego: Elsevier Science, 1990. (b) Jones, R. W., *Fundamental Principles of Sol--Gel Technology*. The Institute of Metals: Brookfield, 1990.

83. Inoue, M.; Kondo, Y.; Inui, T., *Chem. Lett.* **1986**, 1421.

84. Demazeau, G., *High Press. Res.* **2000**, *18,* 203.

85. Silvert, P.-Y.; Herrera-Urbina, R.; Tekaia-Elhsissen, K., *J. Mater. Chem.* **1997**, *7,* 293.

86. Inoue, M.; Otsu, H.; Kominami, H.; Inui, T., *J. Am. Ceram. Soc.* **1991**, *74,* 1452.

87. Rajamathi, M.; Seshadri, R., *Curr. Opin. Solid State Mater. Sci.* **2002**, *6,* 337.

88. Demazeau, G., *J. Mater. Chem.* **1999**, *9,* 15.

89. Qian, Y., *Adv. Mater.* **1999**, *11,* 1101.

90. Bowes, C. L.; Ozin, G. A., *Adv. Mater.* **1996**, *8,* 13.

91. Spandl, J.; Brüdgam, I.; Hartl, H., *Angew. Chem. Int. Ed.* **2001**, *40,* 4018.

92. Yu, S. H.; Yoshimura, M., *Adv. Mater.* **2002**, *14,* 296.

93. Hu, G.; Cheng, M.; Ma, D.; Bao, X., *Chem. Mater.* **2003**, *15,* 1470.

94. Patzke, G. R.; Krumeich, F.; Nesper, R., *Angew. Chem. Int. Ed.* **2002**, *41,* 2446.

95. Yu, S.-H.; Yang, J.; Qian, Y.-T.; Yoshimura, M., *Chem. Phys. Lett.* **2002**, *361,* 362.

96. Lou, Z.; Deng, J.; Wang, L.; Wang, L.; Zhang, T., *Sens. Actuators B* **2013**, *182,* 217.

97. (a) Stankovich, S.; Piner, R. D.; Nguyen, S. B. T.; Ruoff, R. S., *Carbon* **2006**, *44,* 3342. (b) Niyogi, S.; Bekyarova, E.; Itkis, M. E.; McWilliams, J. L.; Hamon, M. A.; Haddon, R. C., *J. Am. Chem. Soc.* **2006**, *128,* 7720. (c) Xu, Y.; Bai, H.; Lu, G.; Li, C.; Shi, G., *J. Am. Chem. Soc.* **2008**, *130,* 5856. (d) Si, Y.; Samulski, E. T., *Nano Lett.* **2008**, *8,* 1679. (e) Xu, Y.; Liu, Z.; Zhang, X.; Wang, Y.; Tian, J.; Huang, Y.; Ma, Y.; Chen, Y., *Adv. Mater.* **2009**, *21,* 1275. (f) Shan, C.; Yang, H.; Han, D.; Zhang, Q.; Ivaska, A.; Niu, L., *Langmuir* **2009**, *25,* 12030. (g) Quintana, M.; Vazquez, E.; Prato, M., *Acc. Chem. Res.* **2012**, *46,* 138.

98. Cao, H.; Wu, X.; Yin, G.; Warner, J. H., *Inorg. Chem.* **2012**, *51,* 2954.

99. (a) Moon In, K.; Lee, J.; Ruoff Rodney, S.; Lee, H., *Nat. Commun.* **2010**, *1,* 73. (b) Zhu, C.; Guo, S.; Fang, Y.; Dong, S., *ACS nano* **2010**, *4,* 2429.

100. Yang, D.; Velamakanni, A.; Bozoklu, G.; Park, S.; Stoller, M.; Piner, R. D.; Stankovich, S.; Jung, I.; Field, D. A.; Ventrice, C. A., Jr.; Ruoff, R. S., *Carbon* **2009**, *47,* 145.

101. (a) Wu, L.-M.; Sharma, R.; Seo, D.-K., *Inorg. Chem.* **2003**, *42,* 5798. (b) Wu, L.-M.; Seo, D.-K., *J. Am. Chem. Soc.* **2004**, *126,* 4676.

102. Barin, I. *Thermochemical Data of Pure Substances,* 3rd ed.; Wiley-VCH Verlag GmbH: Weinheim, 1995.

103. Mills, K. C. *Thermodynamic Data for Inorganic Sulfides, Selenides, and Tellurides;* Butterworth Co.: London, England: 1974.

104. (a) Szabó, T.; Berkesi, O.; Forgó, P.; Josepovits, K.; Sanakis, Y.; Petridis, D.; Dékány, I., *Chem. Mater.* **2006**, *18,* 2740. (b) Jeong, H. K.; Lee, Y. P.; Lahaye, R. J. W. E.; Park, M. H.; An, K. H.; Kim, I. J.; Yang, C. W.; Park, C. Y.; Ruoff, R. S.; Lee, Y. H., *J. Am. Chem. Soc.* **2008**, *130,* 1362.

105. Compton, O. C.; Jain, B.; Dikin, D. A.; Abouimrane, A.; Amine, K.; Nguyen, S. B. T., *ACS Nano* **2011**, *5,* 4380.

106. Beamson, G.; Briggs, D. *High Resolution XPS of Organic Polymers: The Scienta ESCA300 Database;* John Wiley & Sons Ltd: Chichester, 1992.

107. (a) Crispin, X.; Marciniak, S.; Osikowicz, W.; Zotti, G.; van der Gon, A.; Louwet, F.; Fahlman, M.; Groenendaal, L.; De Schryver, F.; Salaneck, W. R., *J. Polym. Sci., Part B: Polym. Phys.* **2003**, *41,* 2561. (b) Gao, W.; Alemany, L. B.; Ci, L.; Ajayan, P. M., *Nat. Chem.* **2009**, *1,* 403.

108. Hutchison, J. E.; Postlethwaite, T. A.; Murray, R. W., *Langmuir* **1993**, *9,* 3277.

109. Whelan, C. M.; Smyth, M. R.; Barnes, C. J.; Brown, N.; Anderson, C. A., *Appl. Surf. Sci.* **1998**, *134,* 144.

110. Nambu, A.; Kondoh, H.; Nakai, I.; Amemiya, K.; Ohta, T., *Surf. Sci.* **2003**, *530,* 101.

111. Skulason, H.; Frisbie, C. D., *J. Am. Chem. Soc.* **2000**, *122,* 9750.

112. (a) Park, S.; An, J.; Piner, R. D.; Jung, I.; Yang, D.; Velamakanni, A.; Nguyen, S. B. T.; Ruoff, R. S., *Chem. Mater.* **2008**, *20,* 6592. (b) Park, S.; An, J.; Jung, I.; Piner Richard, D.; An Sung, J.; Li, X.; Velamakanni, A.; Ruoff Rodney, S., *Nano Lett.* **2009**, *9,* 1593.

113. Greene, F. T.; Gilles, P. W., *J. Am. Chem. Soc.* **1964**, *86,* 3964.

114. Li, D.; Müller, M. B.; Gilje, S.; Kaner, R. B.; Wallace, G. G., *Nat. Nanotechnol.* **2008**, *3,* 101.

115. Marcano, D. C.; Kosynkin, D. V.; Berlin, J. M.; Sinitskii, A.; Sun, Z.; Slesarev, A.; Alemany, L. B.; Lu, W.; Tour, J. M., *ACS nano* **2010**, *4,* 4806.

116. (a) Nemanich, R. J.; Solin, S. A., *Phys. Rev. B* **1979**, *20,* 392. (b) Knight, D. S.; White, W. B., *J. Mater. Res.* **1989**, *4,* 385. (c) Yan, J.-A.; Ruan, W. Y.; Chou, M. Y., *Phys. Rev. B* **2008**, *77,* 125401.

117. (a) Livneh, T.; Haslett, T. L.; Moskovits, M., *Phys. Rev. B* **2002**, *66,* 195110. (b) Cançado, L. G.; Pimenta, M. A.; Neves, B. R. A.; Dantas, M. S. S.; Jorio, A., *Phys. Rev. Lett.* **2004**, *93,* 247401.

118. Kudin, K. N.; Ozbas, B.; Schniepp, H. C.; Prud'Homme, R. K.; Aksay, I. A.; Car, R., *Nano Lett.* **2008**, *8,* 36.

119. (a) Nelson, D.; Peliti, L., *J. Phys.* **1987**, *48,* 1085. (b) Le Doussal, P.; Radzihovsky, L., *Phys. Rev. Lett.* **1992**, *69,* 1209. (c) Janowska, I.; Chizari, K.; Ersen, O.; Zafeiratos, S.; Soubane, D.; Costa, V. D.; Speisser, V.; Boeglin, C.; Houllé, M.; Bégin, D., *Nano Res.* **2010**, *3,* 126.

120. Bae, S.; Kim, H.; Lee, Y.; Xu, X.; Park, J. S.; Zheng, Y.; Balakrishnan, J.; Lei, T.; Kim, H. R.; Song, Y. I., *Nat. Nanotechnol.* **2010**, *5,* 574.

121. Chen, W. F.; Yan, L. F.; Bangal, P. R., *J. Phys. Chem. C* **2010**, *114,* 19885.

122. (a) Silverstein, R.; Morril, T. *Spectrophotometric Identification of Organic Compounds,* 3rd ed.; John Wiley & Sons, Inc.: Hoboken, 1974. (b) Bellamy, L. J. *The Infra-red Spectra of Complex Molecules,* 3rd ed.; Chapman & Hall: London, 1975.

123. Chin, H. C., *Carbon* **1981**, *19,* 175.

124. Ellman, G. L., *Arch. Physiol. Biochem.* **1959**, *82,* 70.

125. (a) Dubin, S.; Gilje, S.; Wang, K.; Tung, V. C.; Cha, K.; Hall, A. S.; Farrar, J.; Varshneya, R.; Yang, Y.; Kaner, R. B., *ACS nano* **2010**, *4,* 3845. (b) Park, S.; An, J.; Potts, J. R.; Velamakanni, A.; Murali, S.; Ruoff, R. S., *Carbon* **2011**, *49,* 3019. (c) Pham, V. H.; Pham, H. D.; Dang, T. T.; Hur, S. H.; Kim, E. J.; Kong, B. S.; Kim, S.; Chung, J. S., *J. Mater. Chem.* **2012**, *22,* 10530.

126. (a) Tauc, J.; Grigorovici, R.; Vancu, A., *Phys. Status Solidi B* **1966**, *15,* 627. (b) Tauc, J., *Mater. Res. Bull.* **1968**, *3,* 37. (c) Fanchini, G.; Ray, S.;

Tagliaferro, A., *Diamond Relat. Mater.* **2003**, *12,* 891. (d) Silva, S. R. P. *Properties of amorphous carbon;* INSPEC, The Institution of Electrical Engineers, London: 2003. (e) Robertson, J.; Leatherhead, S. K. T., *Adv. Phys.* **2011**, *60,* 87.

127. Mathkar, A.; Tozier, D.; Cox, P.; Ong, P.; Galande, C.; Balakrishnan, K.; Leela Mohana Reddy, A.; Ajayan, P. M., *J. Phys. Chem. Lett.* **2012**, *3,* 986.

128. Lowe, A. B., *Polym. Chem.* **2010**, *1,* 17.

129. Ito, E.; Ito, H.; Kang, H.; Hayashi, T.; Hara, M.; Noh, J., *J. Phys. Chem. C* **2012**, *116,* 17586.

130. Zhang, S.; Leem, G.; Srisombat, L.; Lee, T. R., *J. Am. Chem. Soc.* **2008**, *130,* 113.

131. Eda, G.; Fanchini, G.; Chhowalla, M., *Nat. Nanotechnol.* **2008**, *3,* 270.

132. Neto, A. C.; Guinea, F.; Peres, N.; Novoselov, K.; Geim, A., *Reviews of modern physics* **2009**, *81,* 109.

133. (a) Banerjee, S.; Hemraj - Benny, T.; Wong, S. S., *Adv. Mater.* **2005**, *17,* 17. (b) Quintana, M.; Vazquez, E.; Prato, M., *Acc. Chem. Res.* **2012**, DOI: 10.102/ar300138e.

134. (a) Si, Y.; Samulski, E. T., *Nano Lett.* **2008**, *8,* 1679. (b) Moon In, K.; Lee, J.; Ruoff Rodney, S.; Lee, H., *Nat Commun* **2010**, *1,* 73.

135. Chen, C.; Wang, L.; Liu, Y.; Chen, Z.; Pan, D.; Li, Z.; Jiao, Z.; Hu, P.; Shek, C.-H.; Wu, C.-M. L., *Langmuir* **2013**, *29,* 4111.

136. (a) Miyata, K.; Kakizawa, Y.; Nishiyama, N.; Harada, A.; Yamasaki, Y.; Koyama, H.; Kataoka, K., *J. Am. Chem. Soc.* **2004**, *126,* 2355. (b) Choh, S.-Y.; Cross, D.; Wang, C., *Biomacromolecules* **2011**, *12,* 1126.

137. Vericat, C.; Vela, M.; Benitez, G.; Carro, P.; Salvarezza, R., *Chem. Soc. Rev.* **2010**, *39,* 1805.

138. (a) Yantasee, W.; Warner, C. L.; Sangvanich, T.; Addleman, R. S.; Carter, T. G.; Wiacek, R. J.; Fryxell, G. E.; Timchalk, C.; Warner, M. G., *Environ. Sci. Technol.* **2007**, *41,* 5114. (b) Li, G.; Zhao, Z.; Liu, J.; Jiang, G., *J. Hazard. Mater.* **2011**, *192,* 277.

139. (a) Dong, S.; Li, J., *Bioelectrochem. Bioenerg.* **1997**, *42,* 7. (b) Xu, S.; Han, X., *Biosens. Bioelectron.* **2004**, *19,* 1117.

140. Potta, T.; Chun, C.; Song, S.-C., *Biomaterials* **2009**, *30,* 6178.

141. Chapman, J.; Owen, L., *J. Chem. Soc.* **1950**, 579.

142. Djerassi, C.; Gorman, M.; Markley, F.; Oldenburg, E., *J. Am. Chem. Soc.* **1955**, *77,* 568.

143. Kulka, M., *Can. J. Chem.* **1956**, *34,* 1093.

144. Ellis Jr, L.; Reid, E. E., *J. Am. Chem. Soc.* **1932**, *54,* 1674.

145. Tkachenko, B. A.; Fokina, N. A.; Chernish, L. V.; Dahl, J. E.; Liu, S.; Carlson, R. M.; Fokin, A. A.; Schreiner, P. R., *Org. Lett.* **2006**, *8,* 1767.

146. Hofmann, A. W.; Gabriel, S., *Chem. Ber.* **1892**, *25,* 1578.

147. Curran, S. A.; Cech, J.; Zhang, D.; Dewald, J. L.; Avadhanula, A.; Kandadai, M.; Roth, S., *J. Mater. Res.* **2006**, *21,* 1012.

148. Bergman, J.; Pettersson, B.; Hasimbegovic, V.; Svensson, P. H., *J. Org. Chem.* **2011**, *76,* 1546.

149. Khattak, G.; Salim, M.; Wenger, L.; Gilani, A., *J. Non-Cryst. Solids* **2000**, *262,* 66.

150. (a) Moulder, J. F.; Chastain, J.; King, R. C. *Handbook of X-ray photoelectron spectroscopy: a reference book of standard spectra for identification and interpretation of XPS data;* Physical Electronics Eden Prairie, MN: 1995. (b) Fang, J.; Shi, F.; Bu, J.; Ding, J.; Xu, S.; Bao, J.; Ma, Y.; Jiang, Z.; Zhang, W.;

Gao, C., *J. Phys. Chem. C* **2010**, *114,* 7940. (c) Shi, F.; Wang, W.; Huang, W., *Chinese Journal of Chemical Physics* **2012**, *25,* 214.

151. (a) Ohno, T.; Akiyoshi, M.; Umebayashi, T.; Asai, K.; Mitsui, T.; Matsumura, M., *Applied Catalysis A: General* **2004**, *265,* 115. (b) Rengifo-Herrera, J.; Mielczarski, E.; Mielczarski, J.; Castillo, N.; Kiwi, J.; Pulgarin, C., *Applied Catalysis B: Environmental* **2008**, *84,* 448.

152. Lotya, M.; Hernandez, Y.; King, P. J.; Smith, R. J.; Nicolosi, V.; Karlsson, L. S.; Blighe, F. M.; De, S.; ZHIMING, W.; McGovern, I., *J. Am. Chem. Soc.* **2009**, *131,* 3611.

153. Hamilton, C. E.; Lomeda, J. R.; Sun, Z.; Tour, J. M.; Barron, A. R., *Nano letters* **2009**, *9,* 3460.

154. Ferrari, A. C.; Robertson, J., *Phys. Rev. B* **2000**, *61,* 14095.

155. Compton, O. C.; Jain, B.; Dikin, D. A.; Abouimrane, A.; Amine, K.; Nguyen, S. T., *ACS nano* **2011**, *5,* 4380.

156. Pham, V. H.; Cuong, T. V.; Hur, S. H.; Oh, E.; Kim, E. J.; Shin, E. W.; Chung, J. S., *J. Mater. Chem.* **2011**, *21,* 3371.

157. Socrates, G. *Infrared and Raman characteristic group frequencies: tables and charts,* 3rd ed.; John Wiley & Sons Ltd.: Chichester, 2001.

158. (a) Andersson, A.; Johansson, N.; Bröms, P.; Yu, N.; Lupo, D.; Salaneck, W. R., *Adv. Mater.* **1998**, *10,* 859. (b) Gan, Y.; Liu, J.; Zeng, S., *Surf. Coat. Technol.* **2006**, *201,* 25. (c) Rowell, M. W.; Topinka, M. A.; McGehee, M. D.; Prall, H.-J.; Dennler, G.; Sariciftci, N. S.; Hu, L.; Gruner, G., *Appl. Phys. Lett.* **2006**, *88,* 233506. (d) Schmidt-Mende, L.; Fechtenkötter, A.; Müllen, K.; Moons, E.; Friend, R.; MacKenzie, J., *Science* **2001**, *293,* 1119.

159. (a) Wang, L.; Yang, Y.; Marks, T. J.; Liu, Z.; Ho, S.-T., *Appl. Phys. Lett.* **2005**, *87,* 161107. (b) Schlatmann, A.; Floet, D. W.; Hilberer, A.; Garten, F.; Smulders, P.; Klapwijk, T.; Hadziioannou, G., *Appl. Phys. Lett.* **1996**, *69,* 1764.

160. Becerril, H. A.; Mao, J.; Liu, Z.; Stoltenberg, R. M.; Bao, Z.; Chen, Y., *ACS nano* **2008**, *2,* 463.

161. Hernandez, Y.; Nicolosi, V.; Lotya, M.; Blighe, F. M.; Sun, Z.; De, S.; McGovern, I.; Holland, B.; Byrne, M.; Gun'Ko, Y. K., *Nature Nanotechnology* **2008**, *3,* 563.

162. Li, D.; Mueller, M. B.; Gilje, S.; Kaner, R. B.; Wallace, G. G., *Nature nanotechnology* **2008**, *3,* 101.

163. Ghosh, S.; Sarker, B. K.; Chunder, A.; Zhai, L.; Khondaker, S. I., *Appl. Phys. Lett.* **2010**, *96,* 163109.

164. Pham, V. H.; Cuong, T. V.; Hur, S. H.; Shin, E. W.; Kim, J. S.; Chung, J. S.; Kim, E. J., *Carbon* **2010**, *48,* 1945.

165. Cote, L. J.; Kim, F.; Huang, J., *J. Am. Chem. Soc.* **2008**, *131,* 1043.

166. Chen, F.; Liu, S.; Shen, J.; Wei, L.; Liu, A.; Chan-Park, M. B.; Chen, Y., *Langmuir* **2011**, *27,* 9174.

167. Chen, C.; Yang, Q. H.; Yang, Y.; Lv, W.; Wen, Y.; Hou, P. X.; Wang, M.; Cheng, H. M., *Adv. Mater.* **2009**, *21,* 3007.

168. Biswas, S.; Drzal, L. T., *Nano Lett.* **2008**, *9,* 167.

169. (a) Zhu, Y.; Cai, W.; Piner, R. D.; Velamakanni, A.; Ruoff, R. S., *Appl. Phys. Lett.* **2009**, *95,* 103104. (b) Bramhaiah, K.; John, N. S., *Adv. Nat. Sci.: Nanosci. Nanotechnol.* **2012**, *3,* 045002.

170. Verma, V. P.; Das, S.; Lahiri, I.; Choi, W., *Appl. Phys. Lett.* **2010**, *96,* 203108.

171. Wu, J.; Becerril, H. A.; Bao, Z.; Liu, Z.; Chen, Y.; Peumans, P., *Appl. Phys. Lett.* **2008**, *92,* 263302.

172. Wu, J.; Agrawal, M.; Becerril, H. A.; Bao, Z.; Liu, Z.; Chen, Y.; Peumans, P., *ACS nano* **2009**, *4,* 43.

173. Chen, Y.; Zhang, X.; Zhang, D.; Yu, P.; Ma, Y., *Carbon* **2011**, *49,* 573.

174. Schroder, D. K. *Semiconductor material and device characterization;* John Wiley & Sons: Hoboken, New Jersey, 2006.

175. Li, X.; Zhang, G.; Bai, X.; Sun, X.; Wang, X.; Wang, E.; Dai, H., *Nat. Nanotehnol.* **2008**, *3,* 538.

176. Zheng, Q.; Ip, W. H.; Lin, X.; Yousefi, N.; Yeung, K. K.; Li, Z.; Kim, J.-K., *ACS nano* **2011**, *5,* 6039.

177. Cheng, M.; Yang, R.; Zhang, L.; Shi, Z.; Yang, W.; Wang, D.; Xie, G.; Shi, D.; Zhang, G., *Carbon* **2012**, *50,* 2581.

178. (a) Hillion, F.; Daigne, B.; Girard, F.; Slodzian, G.; Schuhmacher, M. In *A new high performance instrument: the CAMECA NanoSIMS 50*, Proceedings of the 9th SIMS Conference, John Wiley and Sons, New York, 1993; pp 254. (b) Slodzian, G.; Daigne, B.; Girard, F.; Hillion, F., *Secondary Ion Mass Spectrometry: SIMS IX* **1993**, 294.

179. Ulman, A. *An Introduction to Ultrathin Organic Films* Academic Press: New York, 1991.

180. (a) Love, J. C.; Estroff, L. A.; Kriebel, J. K.; Nuzzo, R. G.; Whitesides, G. M., *Chem. Rev.* **2005**, *105,* 1103. (b) Dubois, L. H.; Nuzzo, R. G., *Annu. Rev. Phys. Chem* **1992**, *43,* 437.

181. Nuzzo, R. G.; Allara, D. L., *J. Am. Chem. Soc.* **1983**, *105,* 4481.

182. Bain, C. D.; Troughton, E. B.; Tao, Y. T.; Evall, J.; Whitesides, G. M.; Nuzzo, R. G., *J. Am. Chem. Soc.* **1989**, *111,* 321.

183. De Long, H. C.; Buttry, D. A., *Langmuir* **1990**, *6,* 1319.

184. (a) Wilbur, J. L.; Whitesides, G. M., Self-assembly and self-assembled monolayers in micro-and nanofabrication. In *Nanotechnology*; Springer, New York, 1999; pp 331. (b) Schreiber, F., *Prog. Surf. Sci.* **2000**, *65,* 151.

185. (a) Amro, N. A.; Xu, S.; Liu, G.-y., *Langmuir* **2000**, *16,* 3006. (b) Hong, S.; Mirkin, C. A., *Science* **2000**, *288,* 1808.

186. Joachim, C.; Gimzewski, J.; Aviram, A., *Nature* **2000**, *408,* 541.

187. Kane, R. S.; Takayama, S.; Ostuni, E.; Ingber, D. E.; Whitesides, G. M., *Biomaterials* **1999**, *20,* 2363.

188. Grzybowski, B.; Haag, R.; Bowden, N.; Whitesides, G., *Anal. Chem.* **1998**, *70,* 4645.

189. Azzaroni, O.; Cipollone, M.; Vela, M.; Salvarezza, R., *Langmuir* **2001**, *17,* 1483.

190. Brust, M.; Walker, M.; Bethell, D.; Schiffrin, D. J.; Whyman, R., *J. Chem. Soc., Chem. Commun.* **1994**, 801.

191. Shimizu, T.; Teranishi, T.; Hasegawa, S.; Miyake, M., *J. Phys. Chem. B* **2003**, *107,* 2719.

192. Angelova, P.; Solel, E.; Parvari, G.; Turchanin, A.; Botoshansky, M.; Gölzhäuser, A.; Keinan, E., *Langmuir* **2013**, *29,* 2217.

193. (a) Qi, X.; Pu, K. Y.; Zhou, X.; Li, H.; Liu, B.; Boey, F.; Huang, W.; Zhang, H., *Small* **2010**, *6,* 663. (b) Xu, Y.; Bai, H.; Lu, G.; Li, C.; Shi, G., *J. Am. Chem. Soc.* **2008**, *130,* 5856.

194. (a) Wei, D.; Liu, Y.; Wang, Y.; Zhang, H.; Huang, L.; Yu, G., *Nano Lett.* **2009**, *9,* 1752. (b) Deng, D.; Pan, X.; Yu, L.; Cui, Y.; Jiang, Y.; Qi, J.; Li, W.-X.; Fu, Q.; Ma, X.; Xue, Q., *Chem. Mater.* **2011**, *23,* 1188. (c) Sheng, Z.-H.; Shao, L.; Chen, J.-J.; Bao, W.-J.; Wang, F.-B.; Xia, X.-H., *ACS nano* **2011**, *5,* 4350.